Doctoral Dissertation

Studies on EMI noise generation mechanism for switching converter based on time and frequency mixed domain analysis

スイッチングコンバータにおける EMI ノイズ発生メカニズムの 時間-周波数領域解析に関する研究

Takaaki Ibuchi

January 2015

Division of Electrical, Electronic and Information Engineering

Graduate School of Engineering

Osaka University

Abstract

The significant advances in power electronics have led to improvement of energy conversion efficiency and have enlarged their application area. The next generation power electronics circuits require fast switching transitions and high switching frequencies using wide-bandgap power semiconductor devices to achieve high efficiency and miniaturization of circuit. However, the fast switching of power devices with high voltage and large current lead to cause high frequency electromagnetic interference (EMI) noise problem. EMI noise source characterization for clarifying noise generation mechanisms is required to develop a general theory of electromagnetic compatible power converter design that uses wide-bandgap power semiconductor devices.

This thesis characterizes and analyzes EMI noise generation mechanism for switching converter based on time and frequency mixed domain analysis. This research focuses on the switching characteristics of power semiconductor devices, and the dynamic characteristics is evaluated for EMI noise source modeling by extracting damping factor and oscillation frequency from the measured time domain data based on the Prony's method. This research also examines the application of real-time spectrum analysis for EMI noise characterization.

This thesis consists of the following five chapters. Chapter 1 is the introduction. The background and objectives of this research are introduced. The definition of electromagnetic compatibility (EMC) and the importance of EMC design for switching converter are also explained in this chapter.

Chapter 2 treats fundamentals and standards of EMI noise measurements. The conventional EMI noise measurement method with super-heterodyne spectrum

analyzer in frequency domain is addressed. However, the time evolution analysis is useful to evaluate the EMI noise generation mechanism, because EMI noise in switching power converters is transient voltage and current caused by the switching operations of power semiconductor devices. This chapter shows the basic theory of Prony's method to model dynamic characteristics and real-time spectrum analysis.

Chapter 3 studies the influence of the dynamic characteristics of the diode on the conducted noise frequency spectrum in the continuous-current-mode (CCM) DC–DC boost converter, which are experimentally investigated and compared for the Si PiN diode (PiND) and SiC Schottky barrier diode (SBD). In CCM boost converters, the reverse recovery current of a PN diode is induced during its turn-off stemming from turn-on operation of a transistor, which causes not only a switching loss but also a switching noise. The SiC-SBDs have much lower reverse recovery current and recovery time as compared to Si-PiND; hence it is expected that replacing Si-PiND with SiC-SBD will result in dramatically lower recovery losses and EMI noise emission. The dynamic characteristics of diode current in turn-off operation are evaluated by Prony's method. The spectrogram is measured by using real-time spectrum analyzer to understand how the noise source could affect the conducted noise emission.

Chapter 4 focuses on the noise in active power-factor correction (PFC) circuits which are commonly used in the input stage of single-phase AC/DC power converters to improve the power factor and low-order harmonic distortion. It is difficult to evaluate the noise source in PFC converter over time in conventional frequency-domain analysis, whose noise spectrum depends on the operating point. This chapter investigates the losses and conducted noise characteristics of a PFC circuit by comparing the measured noise for Si-PiN diodes, Si-SBD, and SiC-SBD. This chapter also studies the MOSFET's operating condition dependency, which could affect the conducted emission, using real-time spectrum analyzer aimed at modeling EMI noise source of a converter.

Chapter 5 summarizes this thesis and suggests topics for future research work.

Acknowledgments

I would like to express my most sincere gratitude to Professor Tsuyoshi Funaki at Division of Electrical, Electronic and Information Engineering, Graduate School of Engineering, Osaka University. He has provided me the opportunity to accomplish this work, insightful suggestions, and ceaseless encouragement through fruitful discussions.

I would like to thank Professor Toshifumi Ise and Professor Shigemasa Takai at Division of Electrical, Electronic and Information Engineering, Graduate School of Engineering, Osaka University for their careful review on my thesis and valuable suggestions. I would also like to thank Professor Tetsuzo Tanino and Professor Hiroyuki Shiraga at Division of Electrical, Electronic and Information Engineering, Graduate School of Engineering, Osaka University for their useful comments.

I sincerely thank Associate Professor Hideharu Sugihara at Division of Electrical, Electronic and Information Engineering, Graduate School of Engineering, Osaka University for useful suggestions. I am thankful for kind advices of Dr. Hidenori Sekiguchi in National Maritime Research Institute.

I wish to thank all members of Funaki Laboratory for kindness and support. Special thanks to Ms. Fumie Imura, secretary in Funaki laboratory, for kindly supporting my daily work.

This work was partially supported by a Grant-in-Aid for Japan Society for the Promotion of Science (JSPS) Fellows (DC2).

Finally, I deeply thank my parents, sister, and all of my friends for their understanding, continuous support, and encouragement heartfelt.

Contents

Chapter 1

Introduction

1.1 Background

Power electronics realizes the efficient processing of electric power by changing voltage and current magnitude and/or frequency based on fast switching of power semiconductor devices such as metal oxide semiconductor field-effect transistor (MOSFET), insulated gate bipolar transistor (IGBT), and diode [1]–[4]. Their applications include transportation system (locomotives, electric/hybrid electric vehicles, aerospace), industrial applications (variable speed motor drive, factory automation), renewable energy conversion (photovoltaic system, wind generation system), consumer products (lighting, air conditioner), etc. Power electronics is playing an important role in energy conversion and solving the global warming problem [1]–[9].

Modern power electronic systems are required to be high efficiency and reduced size, weight, and cost by fast switching of high voltage and large current in power converters. Fast switching operation is also required for high frequency switching. Passive components (inductors and capacitors) typically dominate the size and weight of a switching converter. Higher frequency switching can substantially improve functionality and miniaturize passive components. The performance of switching converter has been improving due to advances in power semiconductor device. Silicon (Si) has been the basic semiconductor material for power semicon-

ductor devices for a long time. The semiconductor materials such as silicon carbide (SiC) and gallium nitride (GaN) have shown superior electrical and thermal performance over conventional Si semiconductor. These materials have large band gap energy, high carrier mobility, high breakdown electrical field intensity, and high thermal conductivity [10]–[16]. Therefore, these wide-bandgap semiconductor devices can be used in high voltage, large current, fast switching, high frequency, and high temperature applications, which are especially suitable for automobiles and aircraft [4], [12]–[19].

However, fast switching of power devices with high voltage and large current results in high dv/dt and di/dt, and lead to high frequency electromagnetic interference (EMI) noise problem, which stems from the circuit parasitic component [20], [21]. EMI noise can lead to performance degradation of other electrical/electronic equipment. The undesirable EMI effects are interference with wireless systems (e.g., radio, TV, mobile, data transmission), malfunction of biomedical equipment (e.g., cardiac pace maker), false operation of security doors of banks, ABS brake systems of cars, and electronic control systems in airplanes and the increase in power system losses associated with improper performance [4]. The meaning and significance of electromagnetic compatibility (EMC) is discussed briefly in section 1.2.

1.2 Electromagnetic compatibility: definition and importance

This section summarizes some important terms and definitions. Electromagnetic Compatibility (EMC) is "*The capability of electrical and electronic systems, equipment, and devices to operate in their intended electromagnetic environment within a defend margin of safety and at design levels or performance without suffering or causing unacceptable degradation as a result of electromagnetic interference.*" [American National Standards Institute (ANSI) C64.14-1992]

Electromagnetic Interference (EMI) is the process by which disruptive electro-

magnetic energy is transmitted from one electric device to another via radiated or conducted paths (or both). Electromagnetic Susceptibility (Immunity, EMS) is tolerance in the presence of electromagnetic energy (Performance degradation due to electromagnetic energy)[22].

A frequency range containing coherent EM radiation of energy useful for communication purposes is called radio frequency (RF) roughly the range from 9 kHz to 300 GHz. This energy may be emitted as a by-product of an electronic device's operation. There are two categories of EMI noise depending on noise transmission: conducted emission (150 kHz to 30 MHz) and radiated emission (30 MHz to 1 GHz). Conducted emission is the component of RF energy that is emitted through a medium as a propagating wave generally through a wire or interconnect cables. Line-conducted interference refers to RF energy in a power code or alternating-current (AC) mains input cable. Radiated emission is the component of RF energy that is emitted through a medium as an EM field. Although RF energy is usually emitted through free space, other modes of field transmission may be present [23].

The relationship among these terms are summarized in Fig.1.1.

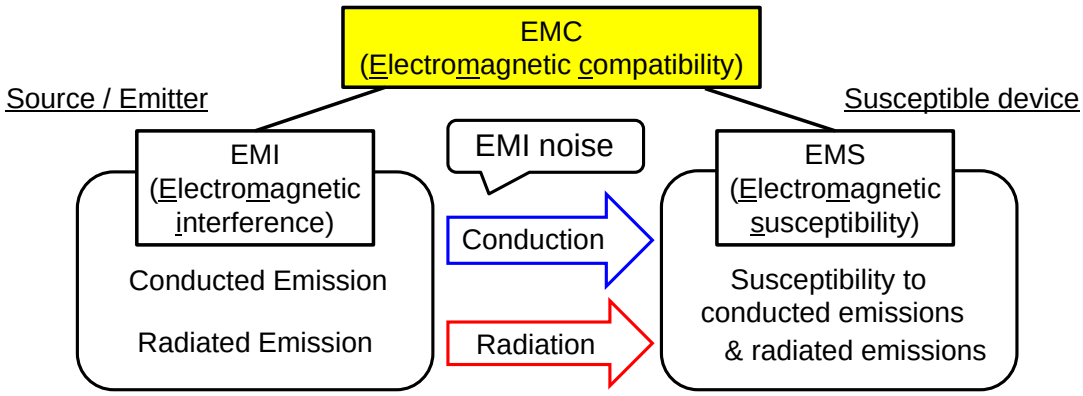

Figure 1.1: EMC definition

Various government agencies and regulatory bodies have imposed EMC regulations that a product must meet before it can be marketed in order to produce an electromagnetically compatible environment. Minimizing EMI noise emission to meet the standards often involves trial and error [23]–[25]. The designer who proceeds with a complete disregard for EMC will almost always have problems

when testing begins. If EMC and noise suppression are considered from design to testing for production, the variety of EMI noise mitigation techniques available to the designer decreases steadily. Early solutions to interference problems are usually the most desirable and cost effective. These trends are shown in Fig.1.2 [24].

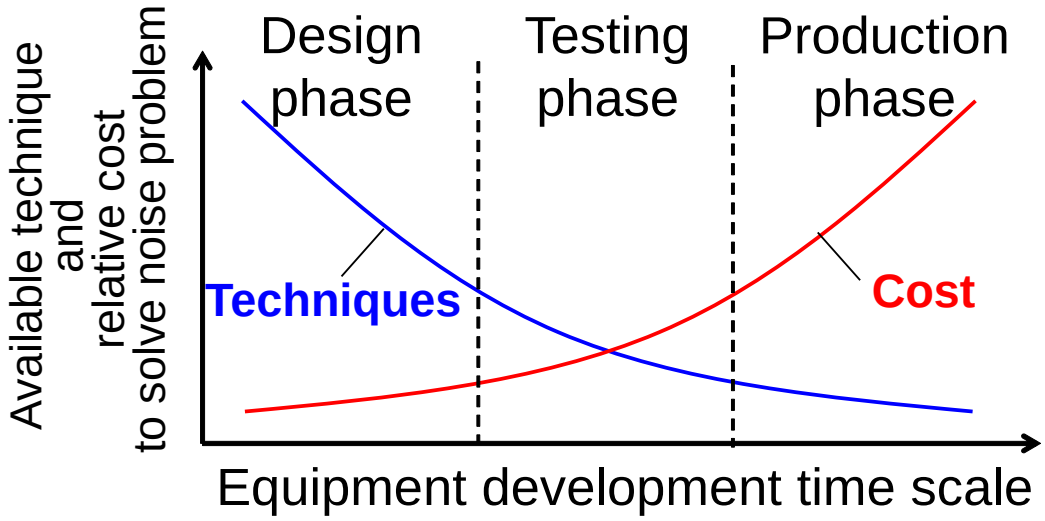

Figure 1.2: Equipment development proceeds

Several methods to minimize conducted EMI noise from the switching converter have been reported. The mitigation approaches are mainly classified into two groups [26]. One way is reducing the EMI noise after its generation by filtering [24], [27]–[29]. However, a post-installed noise filter leads to the increase in size, weight, and its costs. The other approach is reducing the EMI noise at the noise source. The switching devices are the main cause of conducted noise in the case of power electronics circuits. The EMI noise generation can be reduced by proper selection and layout of circuit components [30]–[32], better switch-control scheme [33]–[35], and soft-switching techniques [3], [36], [37]. However, these studies are directed towards circuit level and countermeasure techniques. Therefore, it is necessary for understanding how the voltage and current of the switching device affect the EMI noise in order to clarify EMI noise generation mechanisms and to design the circuit with maximizing switching speed/frequency capability of the wide-bandgap power devices such as SiC and GaN.

1.3 Purpose and outline of this thesis

This thesis is concerned with EMI noise generation mechanism for switching converter based on time and frequency mixed domain analysis. This research focuses on the switching characteristics of power semiconductor devices, and its dynamic characteristic is evaluated for EMI noise source modeling by extracting damping factor and oscillation frequency from the measured time domain data based on the Prony's method. This research also examines the application of real-time spectrum analysis for EMI noise characterization. Fig.1.3 shows the structure of this thesis.

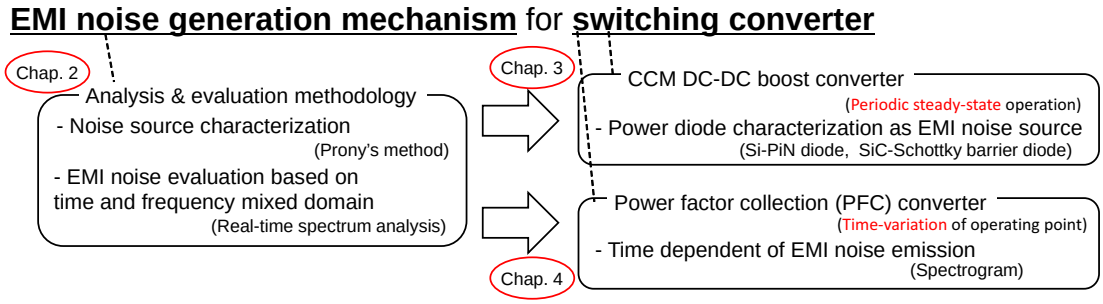

Figure 1.3: The structure of this thesis

Chapter 2 treats fundamentals and standards of EMI noise measurements. The conventional EMI noise measurement method with super-heterodyne spectrum analyzer in frequency domain is addressed. However, the time evolution analysis is useful to consider the EMI noise generation mechanism, because EMI noise in switching power converters is transient voltage and current caused by the switching operations of power semiconductor devices. This chapter shows the basic theory of Prony's method to model dynamic characteristics and real-time spectrum analysis.

Chapter 3 studies the influence of the dynamic characteristics of the diode on the conducted noise frequency spectrum in the continuous-current-mode (CCM) DC–DC boost converter shown in Fig.1.4, which are experimentally investigated and compared for the Si PiN diode (PiND) and SiC Schottky barrier diode (SBD). In CCM boost converters, the reverse recovery current of a PN diode is induced during its turn-off stemming from turn-on operation of a transistor, which causes

not only a switching loss but also a switching noise. The SiC-SBDs have much lower reverse recovery current and recovery time as compared to Si-PiND; hence it is expected that replacing Si-PiND with SiC-SBD will result in dramatically lower recovery losses and EMI noise emission. The dynamic characteristics of diode current in turn-off operation are evaluated by Prony's method. The spectrogram is measured by using real-time spectrum analyzer to understand how the noise source could affect the conducted noise emission.

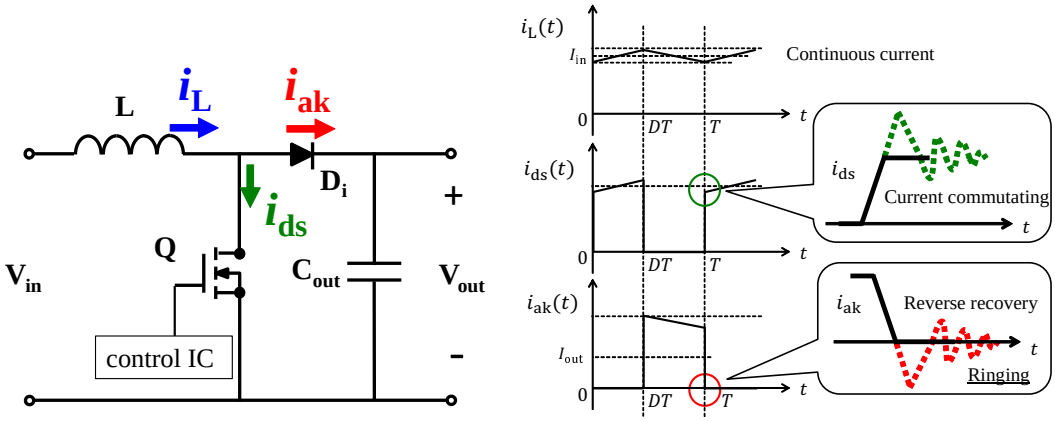

Figure 1.4: CCM boost converter topology and current waveform

Chapter 4 focuses on the noise in active power-factor correction (PFC) circuits which are commonly used in the input stage of single-phase AC/DC power converters to improve the power factor and low-order harmonic distortion. It is difficult to evaluate the noise source in PFC converter over time in conventional frequency-domain analysis, whose noise spectrum depends on the operating point. This chapter investigates the losses and conducted noise characteristics of a PFC circuit by comparing the measured noise for Si-PiN diodes, Si-SBD, and SiC-SBD. This chapter also studies the MOSFET's operating condition dependency, which could affect the conducted emission, using real-time spectrum analyzer aimed at modeling EMI noise source of a converter.

Chapter 5 summarizes this thesis and suggests topics for future research work.

Chapter 2

EMI noise analysis and evaluation methodology based on time and frequency mixed domain

2.1 Introduction

The study of EMI issues is very important in power electronics converters to meet the standard requirements. Section 2.2 covers the EMI noise measurement methods that are laid down in the standards. The standard approach for evaluating conducted and radiated emissions is to analyze noise spectrum amplitude in the frequency domain. However, EMI noise in switching power converters is transient voltage and current caused by the switching of the power semiconductor devices. Therefore, the time evolution analysis is more useful than the spectral amplitude study in the frequency domain to analyze the EMI noise generation mechanism. Section 2.3 shows EMI noise measurement and characterization based on time and frequency mixed domain.

2.2 EMI noise emission standards and conventional EMI noise evaluation method

2.2.1 The international electrotechnical commission

Several international organizations work on the harmonization of standards and regulations. The structure of the bodies which are responsible for defining EMC standards for the purpose of the EMC Directive is shown in Fig.2.1 [38].

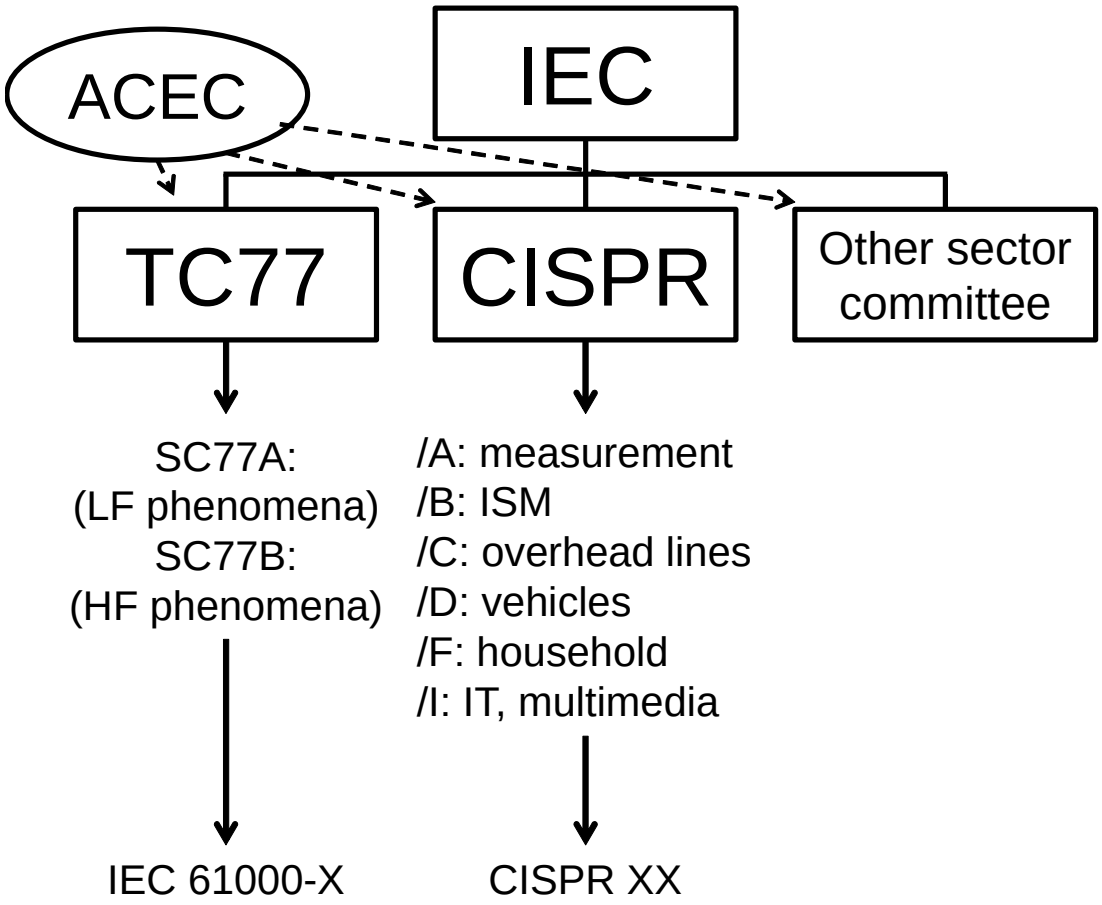

Figure 2.1: International EMC standards structure

The International Electrotechnical Commission (IEC) is the world's leading organization preparing and publishing standards for electrical and electronic technologies. Within the IEC the following committees are interested in the reduction of electromagnetic interference and concerned with EMC issues. The IEC Technical Committee 77 (TC77) prepares standards and technical reports on EMC,

considering general applications and use by product committees [38]. CISPR (International Special Committee on Radio Interference) develops standards concerning EMI and immunity with respect to EMI and and EMC measurement [38]. More than thirty CISPR standards have been published so far. The IEC Advisory Committee on Electromagnetic Compatibility (ACEC) advises the IEC Standards Management Board and prevents the development of conflicting standards [38].

2.2.2 EMI noise emission limits and measurement setup

EMI noise emission limits

EMI noise has to be specified in some detail to generate a standard result, because the measurement results are so dependent on layout and method [22]. Every standard that sets out limits on conducted and radiated emissions (CISPR 22) clearly defines how the data are to be measured . The limits on the conducted and the radiated emissions are plotted in Fig.2.2. The limits are divided into Class A and Class B equipment. Class A devices are those that are marketed for use in a commercial, industrial, or business environment. Class B devices are those that are marketed for use in a residential environment. The Class B limits are more stringent than Class A limits under the reasonable assumption that interference from the device in an industrial environment can be more readily corrected than in a residential environment, where the interference source and the susceptible device are likely to be in closer proximity[23]. There are two levels to be satisfied: QP refers to a quasi-peak detector , whereas Ave refers to an average detector in the measurement spectrum analyzer. These detectors are discussed in more detail in section 2.2.4.

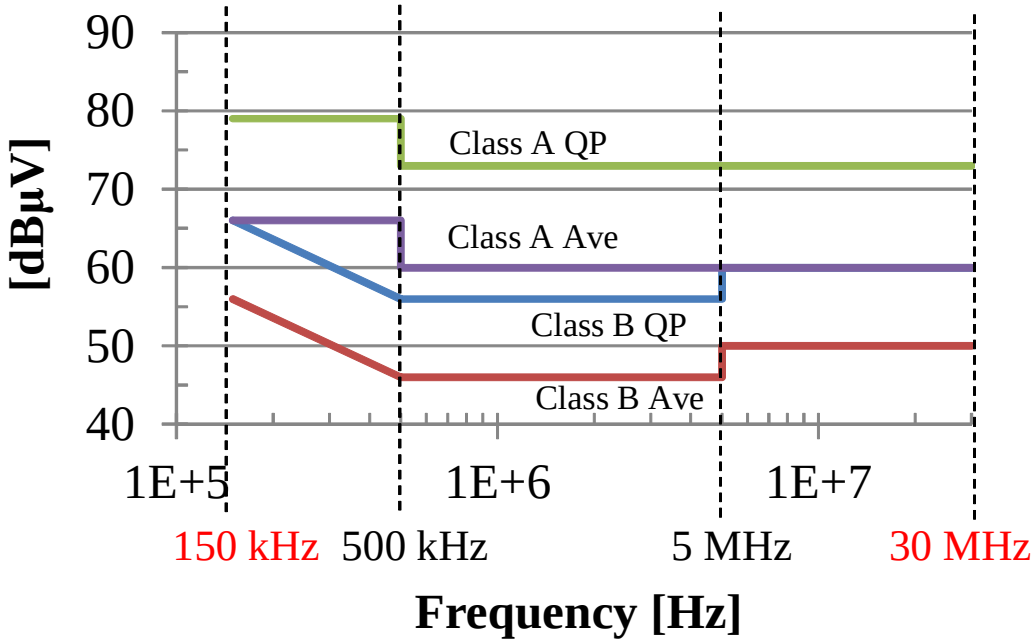

(a) Conducted emission limits

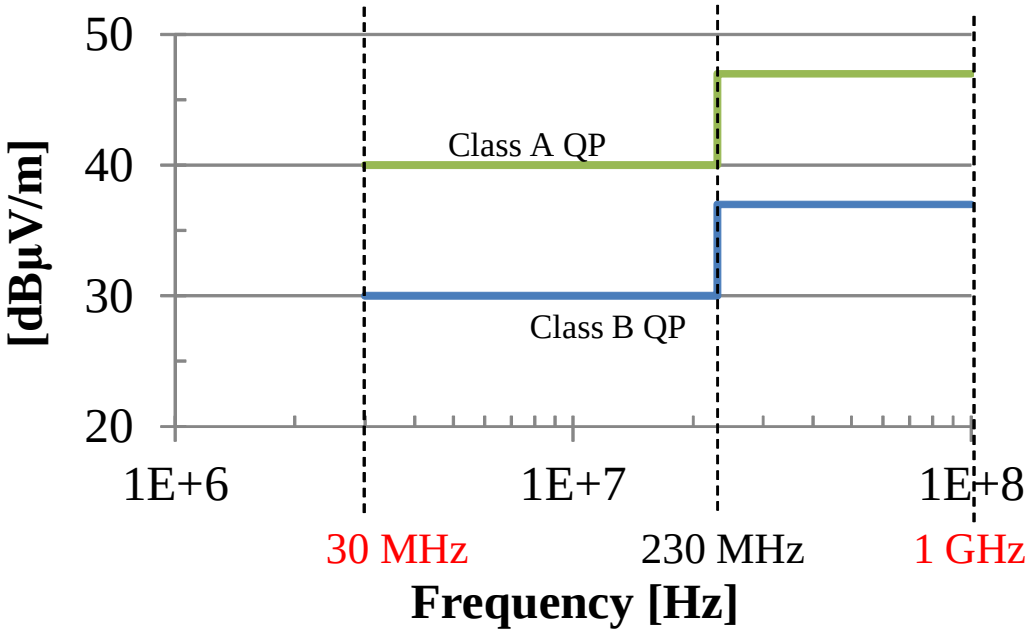

(b) Radiated emission limits

Figure 2.2: EMI noise emission limits (CISPR 22)

2.2.3 EMI noise measurement setup

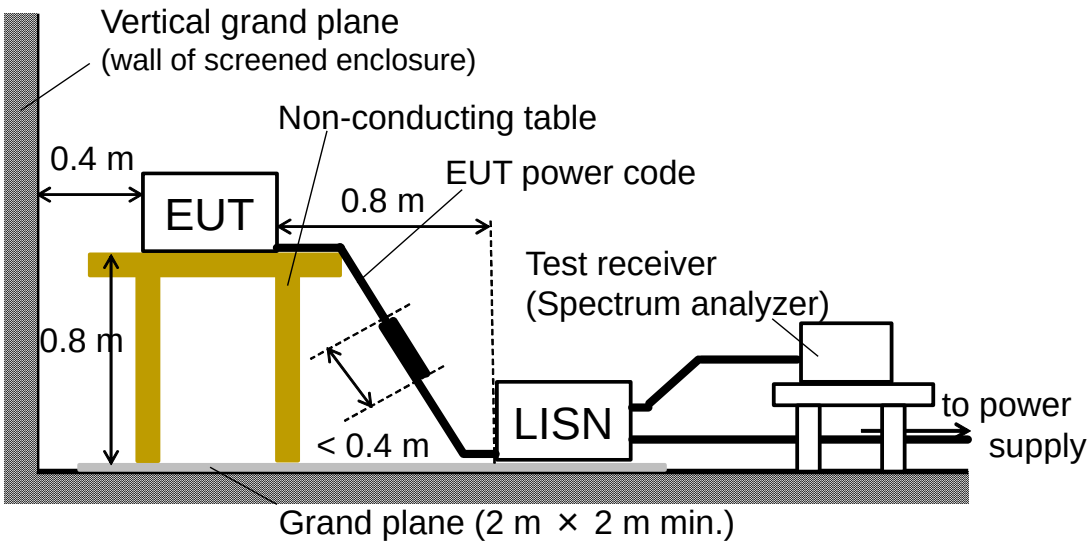

(a) Conducted emission measurement site

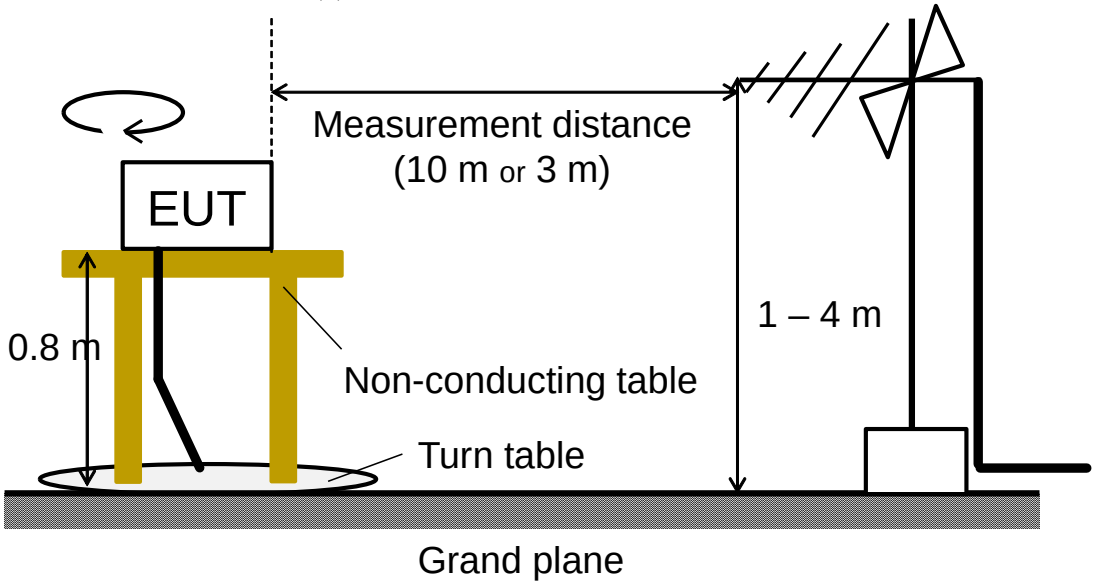

(b) Radiated emission measurement site

Figure 2.3: Layout of EMI noise emission tests (CISPR 16-2-1)

Conducted emissions

Fig.2.3(a) shows the standard layout for conducted emission testing. The principle requirement is to place the equipment under test (EUT) relative to the ground

plane and the line impedance stabilization network (LISN). Placement affects the stray coupling capacitance between EUT and the ground reference, and it must be strictly controlled. The LISN is a low-pass filter network that provides an impedance equivalent to 50 Ω of the power line for the connected EUT, blocks electromagnetic interference coming from the power line, and transfers the electromagnetic interference from the EUT to the spectrum analyzer [23]. The conducted noise disturbance voltage at LISN is usually measured in the frequency range from 150 kHz to 30 MHz. The configuration of LISN is defined in CISPR 16-1-2 and is illustrated in Fig.2.4. This is termed a "V-network" since the impedance appears across each arm of the V for a single-phase supply, where the base of the V is the reference ground.

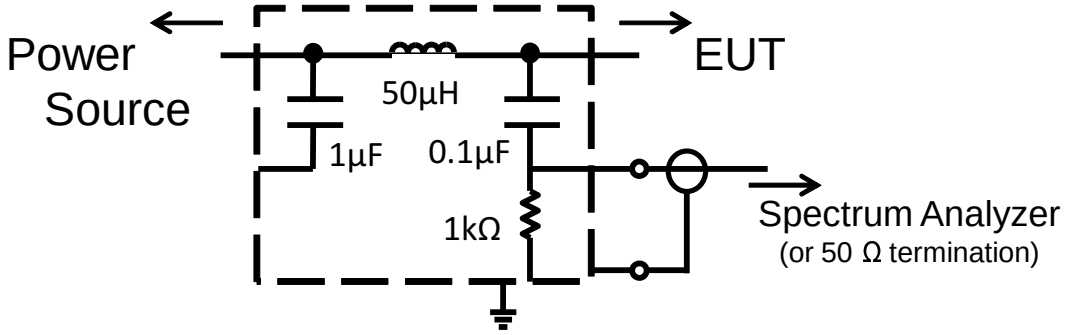

Figure 2.4: The line impedance stabilization network (LISN) for the measurement of conducted emission

LISN's impedance is not defined above 30 MHz, partly because commercial mains conducted emissions are not regulated above 30 MHz, but also because component parasitic reactance makes difficult to achieve 50 Ω impedance above 30 MHz [22]. A similar configuration of LISN is widely used in military tests according to MIL-STD-461E. It can carry higher currents and its impedance can be controlled up to 100 MHz and beyond, since it uses a smaller inductor. The MIL-STD-461E LISN's impedance is specified down to 1 kHz and up to 400 MHz [38].

Radiated emissions

Fig.2.3(b) shows the standard layout for radiated emission testing. The inner side of the metallic wall usually is first covered with ferrite plates and upon these with high-frequency absorbing material. The EUT is placed on a turn table, so that its angular position can be controlled. The CISPR measurement distance is 10 m for both Class A and Class B. The Federal Communications Commission (FCC) in the United States defines the Class B distance with 3 m and the Class A distance with 10 m [23]. The measurement antennas scan from a height of 1 m above the floor to 4 m and record the maximum level. The measurement antennas are also to be directed in horizontal polarization (parallel to the floor) and in vertical polarization (perpendicular to the floor) and the maximum recorded emissions in both polarizations must not exceed the standard. The biconical antenna may be used from 30 to 200 MHz, and the log-periodic antenna is used from 200 MHz to 1 GHz [23].

2.2.4 Conventional EMI noise evaluation method

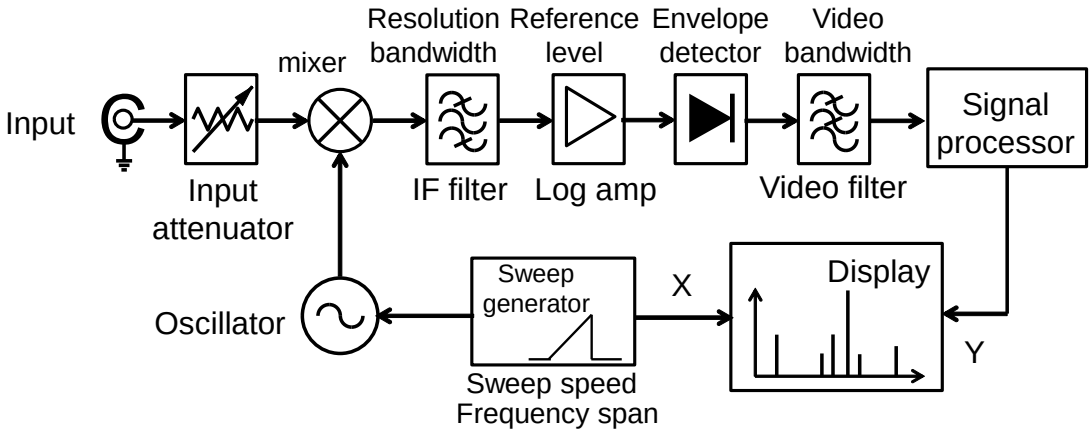

Figure 2.5: Block diagram of spectrum analyzer

The conventional method to evaluate EMI noise is based on the measurement of spectrum analyzers operating in the frequency domain since the mid of 1930's. Fig.2.5 shows the block diagram of a conventional super-heterodyne spectrum analyzers [38]. Compliance measurements require a spectrum analyzer that meets the

requirements of CISPR 16. The input attenuator suppresses the level of the input signal and the mixer does not overload by a controllable attenuator. A mixer and a local oscillator down-convert the signal to an intermediate frequency (IF). The IF filter determines the analyzer's frequency resolution and resolution bandwidth (RBW). Frequency resolution is the ability to distinguish between two signals of similar frequency. CISPR 16-1-1 splits the measurement range of 9 kHz to 1 GHz into four bands, and defines a required measurement RBW as shown in Table 2.1. The filter's resolution bandwidth refers to frequency, which gives -6dB with respect to the peak response. The bandwidth selectivity (ratio of the 60dB bandwidth to the 3dB bandwidth) shapes the IF filter frequency response [38].

Table 2.1: Resolution bandwidth requirements (CISPR 16-1-1)

Band	Frequency range	RBW
A	9 kHz–150 kHz	200 Hz
B	150 kHz–30 MHz	9 kHz
C and D	30 MHz–1 GHz	120 kHz

The measurement signal is evaluated by the three modes of detector for EMI noise emissions: peak, quasi-peak, and average detector mode. The characteristics are defined in CISPR 16-1-1. EMI noise emissions may be amplitude modulated or pulsed. The measured level which is indicated for different type of modulation will depend on the type of detector in use. Fig.2.6 shows the indicated levels for the three detectors with various signal [38].

A peak detector displays the highest level that the signal reaches within the specified time. CISPR standards do not require the peak detector for frequencies below 1 GHz, as shown in Fig.2.2. However, its fast measuring of peak detector makes it very suitable for quick diagnostic, and it can be used to speed up a proper compliance measurement. Average detection takes the average level of the signal. This mode will be the same as its peak value for a continuous signal, but a pulsed or modulated signal will have an average level lower than the peak. The CISPR

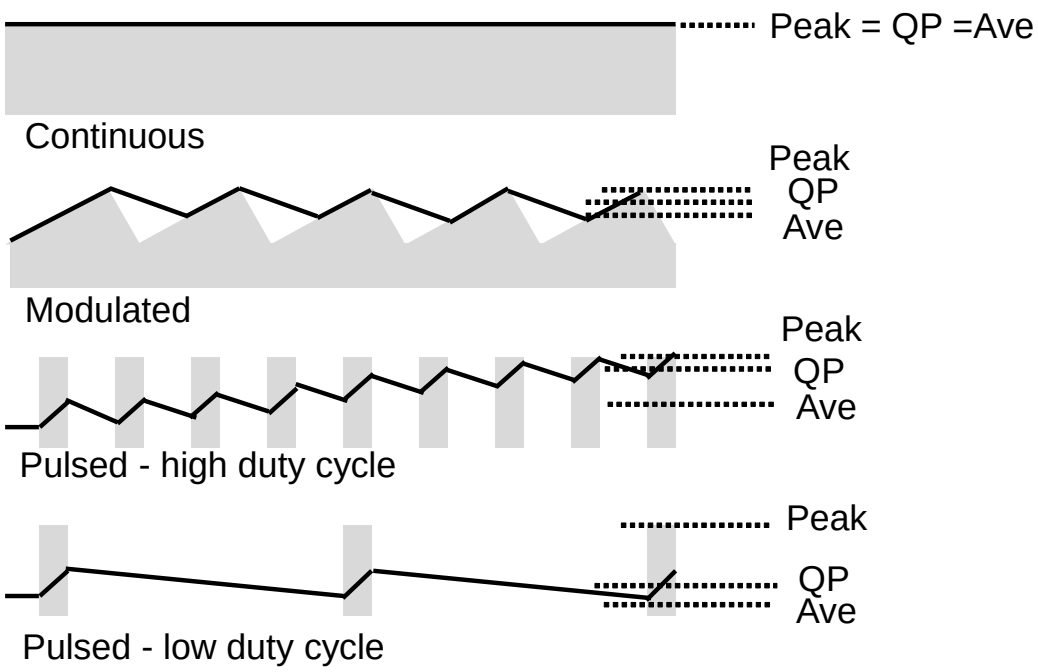

Figure 2.6: Indicated spectral level versus input signals for different detectors

standards call for an average detector measurement on conducted emissions, with limits which are 10–13 dB lower than the quasi-peak limits [38]. Quasi-peak (QP) detection is peak detection with a weighted charge and discharge constant, which corrects for the subjective human response to pulse type interference. A pulsed or modulated signal gives substantially smaller in QP levels than a peak detection give. CISPR lay considerable emphasis on the use of the QP detector since CISPR-based test has historically been intended to protect the communication and broadcast users of the radio spectrum [38]. However, the measurement must dwell on each frequency for substantially longer to get an accurate result. Therefore, the EMI noise measurement using a super-heterodyne spectrum analyzer has to be done with a measuring period long enough.

2.2.5 The Fourier series expansion of periodic signals

The spectrum of the signals is the most important aspect of the ability of the system to satisfy respective regulatory limits as mentioned above. This section discusses the spectrum distribution of periodic switching waveform based on the

Fourier series expansion. The characteristics of their spectra are widely used to understand the underlying relationships between for time-domain phenomenon and spectral content [23], [39], [40].

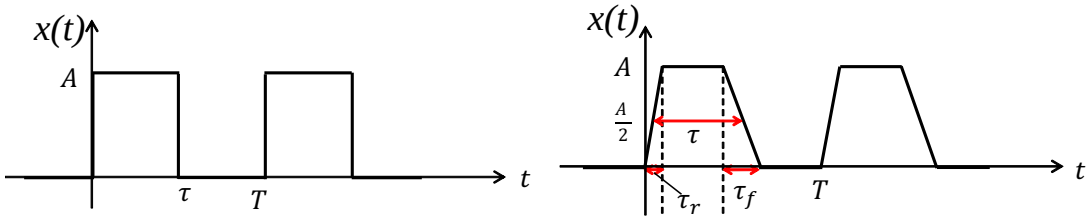

(a) Square wave (b) Trapezoidal wave

Figure 2.7: Periodic pulse trains

The periodic function $x(t)$ with period T is represented as the sum of sinusoidal components that has the integral multiples of the fundamental frequency $k\omega_0$ $\left(\omega_0 = \frac{2\pi}{T} = 2\pi f_0\right)$ [6].

$$x(t) = \sum_{k=-\infty}^{\infty} C_k e^{-jk\omega_0 t} + \sum_{k=1}^{\infty} 2|C_k| \cos(k\omega_0 t + \angle C_k) \tag{2.1}$$

The Fourier coefficient C_k for $x(t)$ is expressed as

$$C_k = \frac{1}{T}\int_0^T x(t) e^{-jk\omega_0 t} dt \tag{2.2}$$

The Fourier coefficient for the periodic square wave with amplitude A and a pulsewidth τ shown in Fig.2.7(a) is obtained as (2.3).

$$\begin{aligned} C_k &= \frac{1}{T}\int_0^T A e^{-jk\omega_0 t} dt = \frac{A}{jk\omega_0 T}(1 - e^{-jk\omega_0 t}) \\ &= \frac{A\tau}{T} e^{-jk\omega_0 \frac{\tau}{2}} \frac{\sin\left(\frac{1}{2}k\omega_0\tau\right)}{\frac{1}{2}k\omega_0\tau} \end{aligned} \tag{2.3}$$

Actual voltage and current do not change abruptly in switching operation, then they are represented as periodic trapezoid as shown in Fig.2.7(b). The Fourier coefficient for the periodic trapezoidal wave is obtained as (2.4).

$$C_k = j\frac{A}{2\pi k} e^{-jk\omega_0 \frac{(\tau+\tau_r)}{2}} \left[\frac{\sin\left(\frac{1}{2}k\omega_0\tau_r\right)}{\frac{1}{2}k\omega_0\tau_r} e^{jk\omega_0 \frac{\tau}{2}} - \frac{\sin\left(\frac{1}{2}k\omega_0\tau_f\right)}{\frac{1}{2}k\omega_0\tau_f} e^{jk\omega_0 \frac{\tau}{2}} \right], \tag{2.4}$$

where τ_r is a pulse risetime, τ_f is a pulse falltime, and τ is a pulse width between 50 % points of the amplitude. If the pulse risetime equals the falltime $\tau_r = \tau_f$, the Fourier coefficient is obtained as follows.

$$C_k = A\frac{\tau}{T}e^{-jk\omega_0\frac{(\tau+\tau_r)}{2}}\frac{\sin\left(\frac{1}{2}k\omega_0\tau\right)}{\frac{1}{2}k\omega_0\tau}\cdot\frac{\sin\left(\frac{1}{2}k\omega_0\tau_r\right)}{\frac{1}{2}k\omega_0\tau_r} \tag{2.5}$$

The magnitudes of Fourier coefficient for one-sided spectrum can be obtained as (2.6) by using (2.5) and $\omega_0 = 2\pi T$.

$$2|C_k| = 2A\frac{\tau}{T}\left|\frac{\sin\left(\frac{k\pi\tau}{T}\right)}{\frac{k\pi\tau}{T}}\right|\left|\frac{\sin\left(\frac{k\pi\tau_r}{T}\right)}{\frac{k\pi\tau_r}{T}}\right| \tag{2.6}$$

The pulse risetime (falltime) τ and the duty ratio D affect the amplitude of spectrum as (2.6). The duty ratio of MOSFET in a boost PFC converter, for example, changes with input voltage level. It leads to the time-varying frequency spectrum distributions.

2.3 EMI noise measurement and characterization in time and frequency mixed domain

Conventional super-heterodyne spectrum analyzer measures EMI noise in the frequency domain. However, this measurements assume that the signal frequency content is time invariant. Spectrum analyzer can only measure within the measurement bandwidth. Signals containing both narrow-band and broad-band spectrum or pulsed transient signal are especially hard to measure reliably. Therefore, time and frequency mixed domain analysis is needed to EMI noise characterization and measurement. This research studies the dynamic characterization of noise based on the Prony's method [41]–[46]. This research also examines the application of real-time spectrum analysis for EMI noise measurement. This section shows basic theory of Prony's method to model dynamic characteristics and real-time spectrum analysis [47]–[54].

2.3.1 Prony's method

Prony's method identifies the mathematical model of a dynamical system with the sampled time domain data as a linear combination of multiple oscillation modes. The damping, frequency, magnitude, and initial phase information of the respective modes are estimated directly. This method is commonly used to analyze physical phenomenon, which can be represented with a combination of damped sine waves, such as sound signals and power system oscillations [41]–[43]. This research applies Prony analysis to model dynamic characteristics. A brief mathematical summary of this method is given as follows.

Assuming the N data samples $y_{(k)}(k = 0, 1, 2, \cdots, N-1)$ (sampling period Δt), the investigated signal can be approximated by n exponential functions which are expressed by the $n$initial values B_i and distinct eigenvalues λ_i as (2.7).

$$y_{(k)} \approx \sum_{i=1}^{n} B_i Z_i^k \qquad (Z_i = \exp(\lambda_i \Delta t), \quad i = 1, 2, \cdots, n) \tag{2.7}$$

The distinct eigenvalue λ_i and the initial value B_i can be expressed as following.

$$\begin{cases} \lambda_i = \alpha_i + j2\pi f_i & (2.8) \\ B_i = A_i e^{j\theta_i}, & (2.9) \end{cases}$$

where α_i is damping factor, f_i is frequency, A_i is amplitude, and θ_i denotes initial phase.

Z_i^n is represented as the roots of the nth order polynomial (characteristic equation).

$$Z_i^n - (a_1 Z_i^{n-1} + a_2 Z_i^{n-2} + \cdots + a_n Z_i^0) = 0 \tag{2.10}$$

If the polynomial coefficients $a_1 \sim a_n$ are identified, the eigenvalue λ_i can be determined from the roots Z_i which satisfy (2.10).

$$\lambda_i = \frac{1}{\Delta t} \log Z_i \tag{2.11}$$

The polynomial may be represented as the sum as (2.12) to define the polynomial coefficient,

$$a_n y_{(0)} + a_{n-1} y_{(1)} + \cdots + a_1 y_{(n-1)} \approx \sum_{i=1}^{n} B_i (a_n Z_i^0 + a_{n-1} Z_i^1 + \cdots + a_1 Z_i^{n-1}) = \sum_{i=1}^{n} B_i Z_i^n = y_{(n)} \tag{2.12}$$

(2.12) denotes that the measured data $y_{(n)}$ can be approximated by the linear combination of the past n data $y_{(0)}$〜$y_{(n-1)}$ and predictive coefficients a_1〜a_n.

Thus, $\hat{y}_{(n)}$ is defined as the predictive data as shown in (2.13).

$$\hat{y}_{(n)} = a_1 y_{(n-1)} + a_2 y_{(n-2)} + \cdots + a_n y_{(0)} \tag{2.13}$$

The N equations of (2.13) may be expressed in matrix form as (2.14).

$$\begin{bmatrix} y_{(n-1)} & y_{(n-2)} & \cdots & y_{(0)} \\ y_{(n)} & y_{(n-1)} & \cdots & y_{(1)} \\ \vdots & \vdots & & \vdots \\ y_{(N-2)} & y_{(N-3)} & \cdots & y_{(N-n-1)} \end{bmatrix} \begin{bmatrix} a_1 \\ a_2 \\ \vdots \\ a_n \end{bmatrix} = \begin{bmatrix} \hat{y}_{(n)} \\ \hat{y}_{(n+1)} \\ \vdots \\ \hat{y}_{(N-1)} \end{bmatrix} \tag{2.14}$$

We may therefore first solve the linear equations (2.14) of a_1〜a_n for measured data $y_{(k)}$, then find the roots Z_i of (2.10). However, these identified coefficients a_1 〜a_n are affected by measured (noisy) data.

The prediction error $e_1(i)$ is expressed as (2.15).

$$e_1(i) = y_{(n+i)} - a_1 y_{(n-1+i)} - a_2 y_{(n-2+i)} + \cdots + a_n y_{(i)} \tag{2.15}$$

The prediction coefficients a_i are determined by the least-square method. The second order evaluation function J_1 is given by (2.16).

$$J_1 = \sum_{i=0}^{N-n-1} e_1(i)^2 = \sum_{i=0}^{N-n-1} \{y_{(n+i)} - a_1 y_{(n-1+i)} - a_2 y_{(n-2+i)} + \cdots + a_n y_{(i)}\}^2 \tag{2.16}$$

The least-square condition for minimizing evaluation function J_1 is expressed as following.

$$\min J_1 = \begin{cases} \frac{\partial J_1}{\partial a_1} = 0 \Leftrightarrow 2 \sum_{i=0}^{N-n-1} [-y_{(n-1+i)}\{y_{(n+i)} - a_1 y_{(n-1+i)} - a_2 y_{(n-2+i)} + \cdots + a_n y_{(i)}\}] = 0 \\ \frac{\partial J_1}{\partial a_2} = 0 \Leftrightarrow 2 \sum_{i=0}^{N-n-1} [-y_{(n-2+i)}\{(y_{(n+i)} - a_1 y_{(n-1+i)} - a_2 y_{(n-2+i)} + \cdots + a_n y_{(i)}\}] = 0 \\ \vdots \\ \frac{\partial J_1}{\partial a_n} = 0 \Leftrightarrow 2 \sum_{i=0}^{N-n-1} [-y_{(i)}\{y_{(n+i)} - a_1 y_{(n-1+i)} - a_2 y_{(n-2+i)} + \cdots + a_n y_{(i)}\}] = 0 \end{cases} \tag{2.17}$$

$$\therefore \begin{cases} \sum_{i=0}^{N-n-1} y_{(n-1+i)}y_{(n+i)} = a_1 \sum_{i=0}^{N-n-1} y_{(n-1+i)}y_{(n-1+i)} + \cdots + a_n \sum_{i=0}^{N-n-1} y_{(n-1+i)}y_{(i)} \\ \sum_{i=0}^{N-n-1} y_{(n-2+i)}y_{(n+i)} = a_1 \sum_{i=0}^{N-n-1} y_{(n-2+i)}y_{(n-1+i)} + \cdots + a_n \sum_{i=0}^{N-n-1} y_{(n-2+i)}y_{(i)} \\ \vdots \\ \sum_{i=0}^{N-n-1} y_{(i)}y_{(n+i)} = a_1 \sum_{i=0}^{N-n-1} y_{(i)}y_{(n-1+i)} + \cdots + a_n \sum_{i=0}^{N-n-1} y_{(i)}y_{(i)} \end{cases} \tag{2.18}$$

(2.14) is presented in the matrix form $\mathbf{Y}=\mathbf{A}\mathbf{X}$, where

$$\mathbf{Y} = \begin{bmatrix} \sum_{i=0}^{N-n-1} y_{(n-1+i)}y_{(n+i)} \\ \sum_{i=0}^{N-n-1} y_{(n-2+i)}y_{(n+i)} \\ \vdots \\ \sum_{i=0}^{N-n-1} y_{(i)}y_{(n+i)} \end{bmatrix}$$

$$, \mathbf{A} = \begin{bmatrix} \sum_{i=0}^{N-n-1} y_{(n-1+i)}y_{(n-1+i)} & \sum_{i=0}^{N-n-1} y_{(n-1+i)}y_{(n-2+i)} & \cdots & \sum_{i=0}^{N-n-1} y_{(n-1+i)}y_{(i)} \\ \sum_{i=0}^{N-n-1} y_{(n-2+i)}y_{(n-1+i)} & \sum_{i=0}^{N-n-1} y_{(n-2+i)}y_{(n-2+i)} & \cdots & \sum_{i=0}^{N-n-1} y_{(n-2+i)}y_{(i)} \\ \vdots & \vdots & & \vdots \\ \sum_{i=0}^{N-n-1} y(i)y(n-1+i) & \sum_{i=0}^{N-n-1} y_{(i)}y_{(n-2+i)} & \cdots & \sum_{i=0}^{N-n-1} y(i)y(i) \end{bmatrix}$$

$$, \mathbf{X} = \begin{bmatrix} a_1 \\ a_2 \\ \vdots \\ a_n \end{bmatrix}. \text{ Therefore, } a_1 \sim a_n \text{ can be identified by } \mathbf{X} = \mathbf{A}^{-1}\mathbf{Y}.$$

In the second step, the roots of the polynomial Z_i, which is defined by (2.10), is calculated with the relationship $z = e^{-sT}$ (T : sampling period).

$$z^n Z_j = a_1 z^{n-1} Z_j + a_2 z^{n-2} Z_j + \cdots + a_{n-1} z^1 Z_j + a_n Z_j \tag{2.19}$$

Where $Z_1, Z_2, Z_3, \cdots, Z_n$ are expressed with Z_j as following.

$$\begin{aligned} Z_1 &= Z_j \\ Z_2 &= zZ_j \\ Z_3 &= z^2 Z_j \\ &\vdots \\ Z_n &= z^{n-1} Z_j \end{aligned} \tag{2.20}$$

Multiply both sides of (2.20) with z.

$$\begin{aligned} zZ_1 &= zZ_j \\ zZ_2 &= z^2 Z_j \\ &\vdots \\ zZ_n &= z^n Z_j \\ &= a_1 z^{n-1} Z_j + a_2 z^{n-2} Z_j + \cdots + a_{n-1} z Z_j + a_n Z_j \qquad (\because (2.19)) \\ &= a_1 Z_n + a_2 Z_{n-1} + \cdots + a_{n-1} Z_2 + a_n Z_1 \qquad (\because (2.20)) \end{aligned} \tag{2.21}$$

$$\therefore \begin{bmatrix} zZ_1 \\ zZ_2 \\ \vdots \\ zZ_n \end{bmatrix} = \begin{bmatrix} 0 & 1 & 0 & 0 & \cdots & 0 & 0 \\ 0 & 0 & 1 & 0 & \cdots & 0 & 0 \\ \vdots & \vdots & \vdots & \vdots & \cdots & \vdots & \vdots \\ 0 & 0 & 0 & 0 & \cdots & 0 & 1 \\ a_n & a_{n-1} & a_{n-2} & a_{n-3} & \cdots & a_2 & a_1 \end{bmatrix} \begin{bmatrix} Z_1 \\ Z_2 \\ \vdots \\ Z_n \end{bmatrix} \tag{2.22}$$

Z_i is expressed by using the eigenvalue of the matrix $\begin{bmatrix} 0 & 1 & 0 & 0 & \cdots & 0 & 0 \\ 0 & 0 & 1 & 0 & \cdots & 0 & 0 \\ \vdots & \vdots & \vdots & \vdots & \cdots & \vdots & \vdots \\ 0 & 0 & 0 & 0 & \cdots & 0 & 1 \\ a_n & a_{n-1} & a_{n-2} & a_{n-3} & \cdots & a_2 & a_1 \end{bmatrix}$.

The eigenvalue λ_i (the damping factor and sinusoidal frequency) may be determined from the roots Z_i.

In the last step, the initial values B_i are determined by using the eigenvalue

λ_i. The successive N data $y_{(i)}$ can be expressed by (2.7) as following equation.

$$\begin{bmatrix} Z_1^0 & Z_2^0 & \cdots & Z_n^0 \\ Z_1^1 & Z_2^1 & \cdots & Z_n^1 \\ \vdots & \vdots & & \vdots \\ Z_1^{N-1} & Z_2^{N-1} & \cdots & Z_n^{N-1} \end{bmatrix} \begin{bmatrix} B_1 \\ B_2 \\ \vdots \\ B_n \end{bmatrix} \approx \begin{bmatrix} y_{(0)} \\ y_{(1)} \\ \vdots \\ y_{(N-1)} \end{bmatrix} \tag{2.23}$$

The initial values B_i are determined by the least-square method using (2.23). The errors $e_2(i)$ between the measured value $y_{(i)}$ and the estimated value $\hat{y}_{(i)}$ are expressed as following.

$$e_2(i) = y_{(i)} - B_1 Z_1^i - B_2 Z_2^i + \cdots + B_n Z_n^i \tag{2.24}$$

Then, the second order evaluation function J_2 is given by (2.25).

$$J_2 = \sum_{i=0}^{N-1} e_2(i)^2 = \sum_{i=0}^{N-1} \{y_{(i)} - B_1 Z_1^i - B_2 Z_2^i + \cdots + B_n Z_n^i\}^2 \tag{2.25}$$

The least-square condition for minimizing evaluation function J_2 is expressed as following.

$$\min J_2 = \begin{cases} \frac{\partial J_2}{\partial B_1} = 0 \Leftrightarrow 2 \sum_{i=0}^{N-1} [-Z_1^i \{y_{(i)} - B_1 Z_1^i - B_2 Z_2^i + \cdots + B_n Z_n^i\}] = 0 \\ \frac{\partial J_2}{\partial B_2} = 0 \Leftrightarrow 2 \sum_{i=0}^{N-1} [-Z_2^i \{y_{(i)} - B_1 Z_1^i - B_2 Z_2^i + \cdots + B_n Z_n^i\}] = 0 \\ \vdots \\ \frac{\partial J_2}{\partial B_n} = 0 \Leftrightarrow 2 \sum_{i=0}^{N-1} [-Z_n^i \{y_{(i)} - B_1 Z_1^i - B_2 Z_2^i + \cdots + B_n Z_n^i\}] = 0 \end{cases} \tag{2.26}$$

$$\therefore \begin{cases} \sum_{i=0}^{N-1} Z_1^i y_{(i)} = B_1 \sum_{i=0}^{N-1} Z_1^i Z_1^i + \cdots + B_n \sum_{i=0}^{N-1} Z_1^i Z_n^i \\ \sum_{i=0}^{N-1} Z_2^i y_{(i)} = B_1 \sum_{i=0}^{N-1} Z_2^i Z_1^i + \cdots + B_n \sum_{i=0}^{N-n-1} Z_2^i Z_n^i \\ \vdots \\ \sum_{i=0}^{N-1} Z_n^i y_{(i)} = B_1 \sum_{i=0}^{N-1} Z_n^i Z_1^i + \cdots + B_n \sum_{i=0}^{N-1} Z_n^i Z_n^i \end{cases} \tag{2.27}$$

(2.23) is presented in the matrix form $\mathbf{Y}$=$\mathbf{CX}$, where

$$\mathbf{Y} = \begin{bmatrix} \sum_{i=0}^{N-1} Z_1^i y(i) \\ \sum_{i=0}^{N-1} Z_2^i y(i) \\ \vdots \\ \sum_{i=0}^{N-1} Z_n^i y(i) \end{bmatrix}, \mathbf{C} = \begin{bmatrix} \sum_{i=0}^{N-1} Z_1^i Z_1^i & \sum_{i=0}^{N-1} Z_1^i Z_2^i & \cdots & \sum_{i=0}^{N-1} Z_1^i Z_n^i \\ \sum_{i=0}^{N-1} Z_2^i Z_1^i & \sum_{i=0}^{N-1} Z_2^i Z_2^i & \cdots & \sum_{i=0}^{N-1} Z_2^i Z_n^i \\ \vdots & \vdots & & \vdots \\ \sum_{i=0}^{N-1} Z_n^i Z_1^i & \sum_{i=0}^{N-1} Z_n^i Z_2^i & \cdots & \sum_{i=0}^{N-1} Z_n^i Z_n^i \end{bmatrix}, \mathbf{X} = \begin{bmatrix} B_1 \\ B_2 \\ \vdots \\ B_n \end{bmatrix}.$$

Therefore, $B_1 \sim B_n$ can be identified by $\mathbf{X} = \mathbf{C}^{-1}\mathbf{Y}$.

The a_i and B_i are respectively calculated with the linear least square method. Thus, model output $\hat{y}(k)$, approximates the measured value $y(k)$ in a least squares sense. The model order n must be smaller than half of the samples $\frac{N}{2}$.

Fig.2.8 shows an example of the dynamic characteristics evaluation based on Prony analysis. The algorithm of Prony analysis is implemented with GNU Octave.

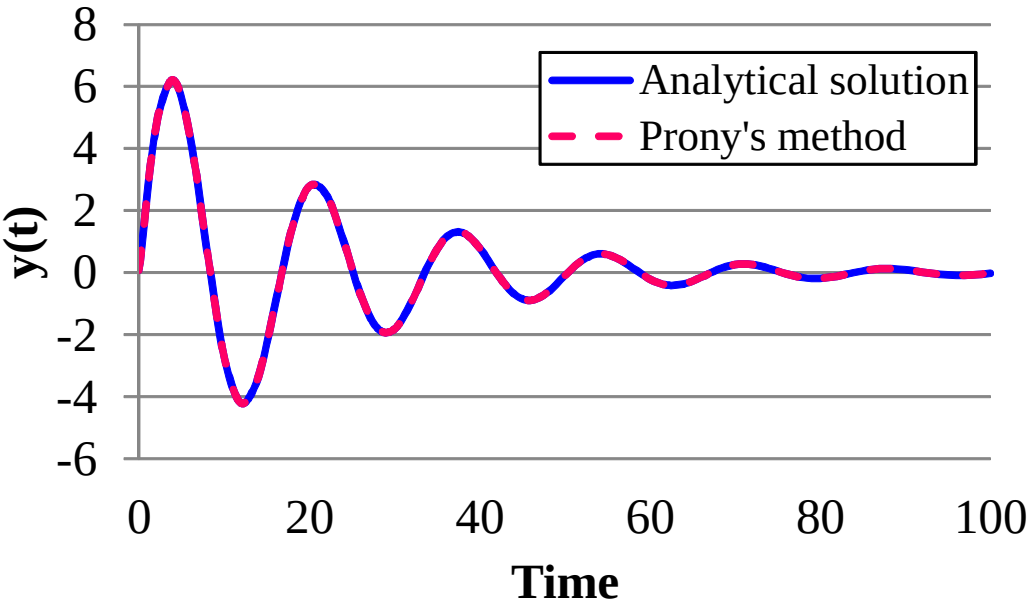

Figure 2.8: Dynamic characteristics evaluation for analytical solution

The dynamic behavior emerges as the dominant mode of the response, which can be extracted as the mode with large signal residue $|B_i|$ [43]. That is, the

reduced order model is obtained as a sum of the dominant modes. Prony analysis results are susceptible to noise in the measured samples. When they have auto correlation, the noise components are also evaluated in an oscillation mode in the Prony's method. This affects the accuracy of the identified λ_i and B_i when the model order n is insufficiently low [44]. Then, a higher-order model is preferable for noisy data.

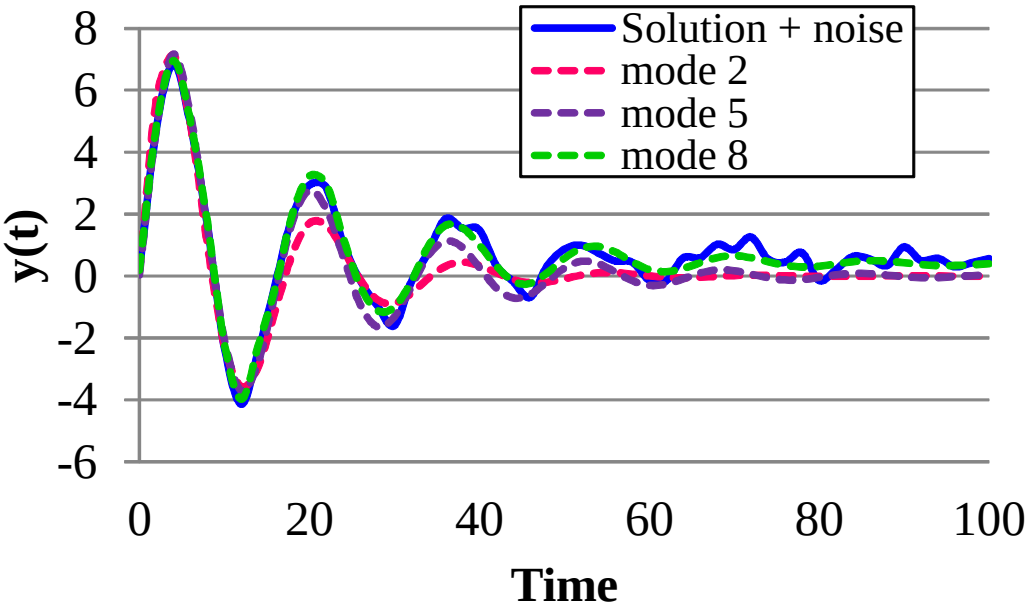

(a) Prony analysis for noisy data

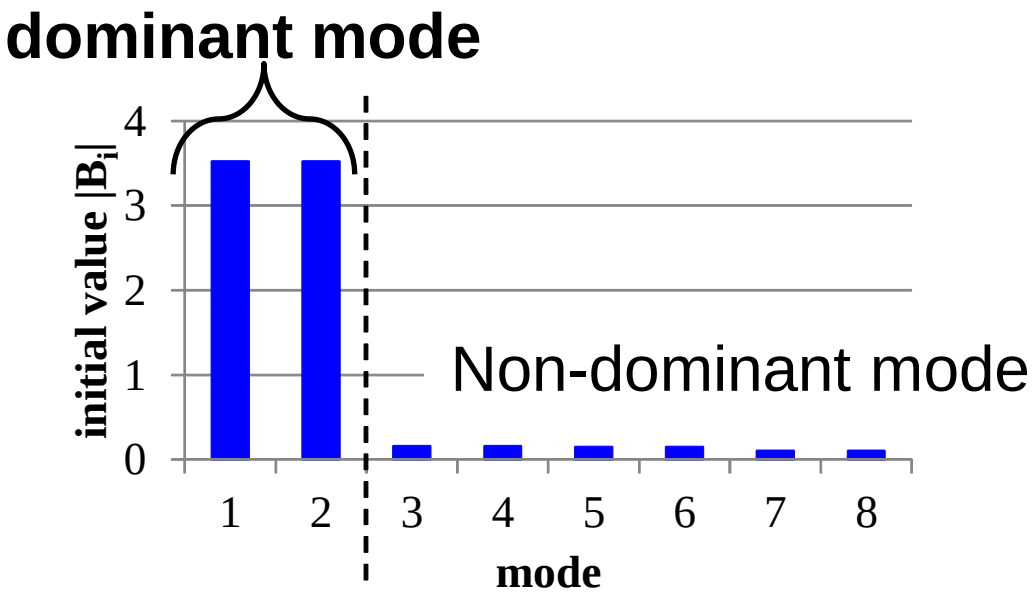

(b) Magnitude of the initial values of the decomposed modes

Figure 2.9: Dynamic characteristics evaluation for noise-included data

2.3.2 Real-time spectrum analysis

Real-time spectrum analysis is based on digital signal processing, which is performed using discrete Fourier transform (DFT). The DFT formulation considers periodic repetition of signal in time-domain and is given as (2.28).

$$X[k] = \sum_{n=0}^{N-1} x[n] e^{\frac{-j2\pi kn}{N}} \tag{2.28}$$

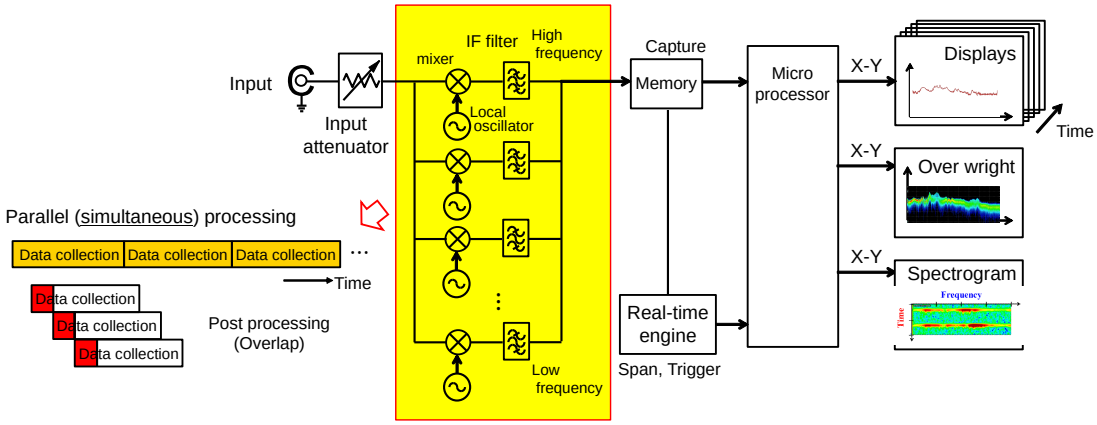

Figure 2.10: Block diagram of real-time spectrum analyzer

Real-time spectrum analyzer reveals how the signal spectrum evolves over time. The block diagram of real-time spectrum analyzer is shown in Fig.2.10 [47], [49]. EMI noise consists of stationary and transient signal. Real-time means that there is no dead time between acquisitions and all sampled data are processed. Real-time calculations demand that DFTs be performed on Field Programmable Gate Arrays (FPGAs). The short-time Fast Fourier Transform (STFT) is used for fast calculation. The mathematical formulation of the STFT of the signal $x(t)$ is given as [52]

$$STFT_h[x](t,\omega) = \int_{-\infty}^{\infty} x(\tau) h^*(t-\tau) e^{-j\omega\tau} d\tau, \tag{2.29}$$

where $h(t)$ a window function for local spectral analysis and $*$ denotes the complex conjugation. Spectrogram is STFT for a sequence computed using a sliding window. The spectrogram is analyzed as output

$$SP_h[x](t,\omega) = |STFT_x(t,\omega)|^2. \tag{2.30}$$

The resulting Fourier transform contains both the frequency and time behavior of the signal. The STFT calculates the Fourier transform on a segment-by-segment basis. Individual segments used in the calculation can overlap and some weighted windowing function can be used.

The window function $h(t)$ balances the time and frequency resolution of the spectrogram. If DFT is used in spectrum estimation, the spectrogram has a spectral resolution Δf_D as (2.31).

$$\Delta f_D = \frac{2\pi}{N} = \frac{f_s}{N}, \tag{2.31}$$

where N is the window length and f_s is the sampling frequency. N also affects the time resolution. The time resolution in a spectrogram is

$$\Delta t = \frac{N}{f_s}. \tag{2.32}$$

Equation (2.31) suggests that a short window leads to a fine time resolution and worse frequency resolution and vice versa [52]. A good compromise can be achieved by tuning time-segment length, overlapping, and selecting proper window function of DFT.

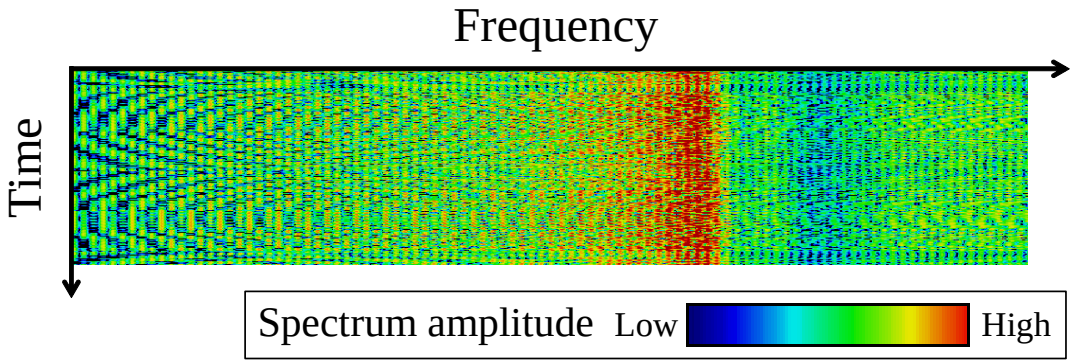

Figure 2.11: An example of spectrogram

Fig.2.11 shows an example of spectrogram. The frequency is plotted along x-axis and time along y-axis. The color scale represents the spectrum amplitude. Spectrograms are used in applications, where the spectral content of the signal changes continuously; e.g. speech recognizing, sonar, radar processing, and biomedical signal analysis [54]. This method can also be used to identify the

source of emissions in complex systems where multiple broadband sources exist, such as switched power supplies with DC-DC converters [52]. However, time and frequency mixed domain analysis has not been commonly used in the field of EMI noise measurements. This research studies how the change of the working point of the circuit could affect the noise spectrum distribution of terminal disturbance voltage using real-time spectrum analyzer for modeling EMI noise source in a switching power converter.

2.4 Summary

This chapter treated fundamentals and standards of EMI noise measurement methods. Section 2.2 described EMC standard structure and conducted / radiated EMI noise regulations that are now in existence. The conventional EMI noise measurement with super-heterodyne spectrum analyzer is also addressed. Section 2.3 presented EMI noise source analysis and evaluation methodology based on time and frequency mixed domain analysis techniques. Section 2.3.1 studies the dynamic characteristics modeling based on the Prony's method. The prony analysis is susceptible to the noise components in the time-domain measured data. It is able to extract the dominant mode with large signal residue $|B_i|$ for high order model. The error of the model can be reduced with higher order decomposition. Though this reduces the numerical error, it disrupts the physical meaning of the dominant mode. Real-time spectrum analysis described in section 2.3.2 is especially useful to identify the sources of emissions and the switching operations to emit EMI noise. It intuitively displays the spectrum levels over time, offering a new perspective that cannot be achieved by specific time and frequency domain analysis.

Chapter 3

EMI noise generation mechanism for switching converter

3.1 Introduction

The continuous current mode (CCM) boost converters are widely used for high-power application circuit. However, the reverse recovery current is induced for a conventional Silicon (Si)-PiN diode (PiND) in turn-off operation, which is initiated by the turn-on operation of transistor, resulting in not only a large switching loss but also a switching noise in the CCM converter [55],[56]. Silicon carbide (SiC) semiconductors have superior electrical and thermal performance compared with conventional Si semiconductors [10]–[16]. SiC-Schottky barrier diode (SBD) exhibits almost no reverse recovery current. The possible advantages in its application have been focused on power conversion circuits, improvement in efficiency, and temperature stability characteristics have been presented [57]–[59]. This chapter focuses on the turn-off operation of Si-PiND and SiC-SBD, and investigates the influence of diode characteristics on conducted emission of CCM boost DC-DC converter in periodic steady-state operation.

3.2 Power diode operating characteristics: PiN diode and Schottky barrier diode

3.2.1 Switching characteristics

A P–N junction diodes suffer from reverse recovery. Fig.3.1 shows the diode current and voltage waveforms of a P–N junction diode in turn-off operation with finite rate of change of the diode current $|\frac{di_F}{dt}|$. The carrier stored in a drift layer of a PN diode causes a transient reverse current to flow during a rapid transition from the conducting state to blocking state. The anode voltage starts to establish when the reverse current reaches the peak $I_{\mathrm{R_p}}$; then, it approaches the supply voltage. The recovery time t_{rr} is defined as the time between the zero-crossing point of the current and the point in time in which the current has decayed down to 10% of $I_{\mathrm{R_p}}$ [10]. Removal of stored excess minority carrier is achieved by the flow of reverse current and by the recombination of minority carriers [11]. Reverse recovery current causes switching losses and the steep current decrement from peak reverse current. This peak induces surge voltage in the circuit, which results in a broad spectrum of EMI noise. High $\frac{di_R}{dt}$ induces a significant voltage and current oscillation, which stems from the resonance between the terminal capacitance of diode and parasitic inductance of circuit wiring [21]. This ringing oscillation also could cause EMI noise.

A cross-section of PiN diode and Schottky barrier diode is depicted in Fig. 3.2. PiN diode is a bipolar device which injects large amounts of hole in the n^- drift region to achieve low on resistance with conductivity modulation. The stored charge has to be removed or recombined to turn off PiN diode. In contrast, Schottky barrier diodes (SBD) operate with majority carrier and do not store minority carrier, therefore it does not have reverse recovery phenomenon. However, small current flows to deplete the drift region which depends on the applied voltage [10]. The peak reverse recovery current $I_{\mathrm{R_p}}$ of Si-PiND is much higher than that of the SiC-SBD. $I_{\mathrm{R_p}}$ increases with increasing temperature for Si-PiND, but it remains nearly constant for SiC-SBD. The rated blocking voltage of Si-SBD is

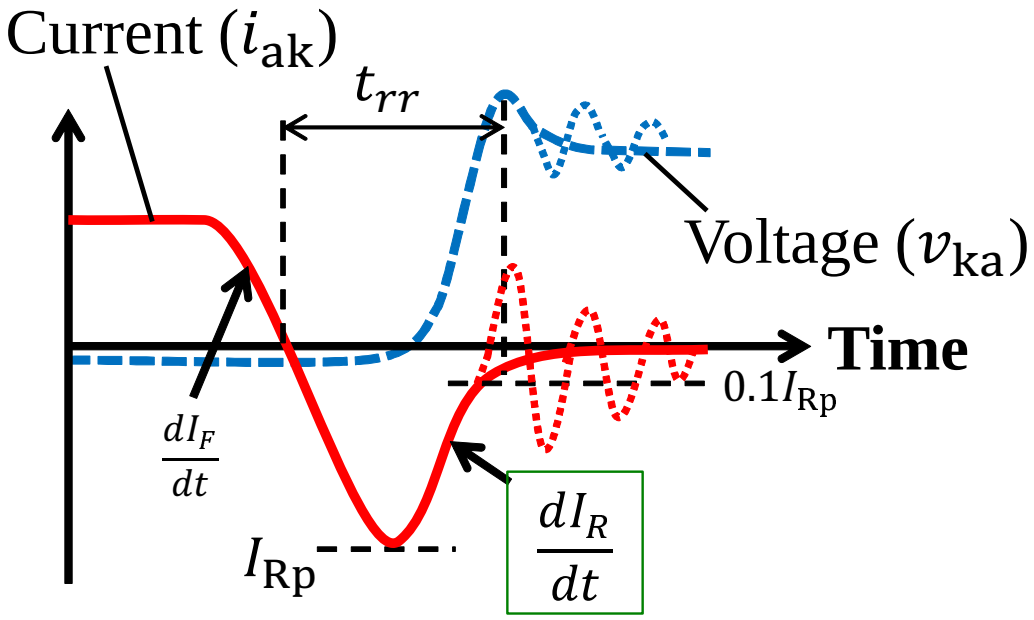

Figure 3.1: The reverse recovery phenomenon of P–N junction diode

low, typically below 200 V. In contrast, the breakdown voltage of SiC-SBD is high, typically in the range of 300–1200 V, which is suitable for high-power, fast-switching power conversion circuits [11].

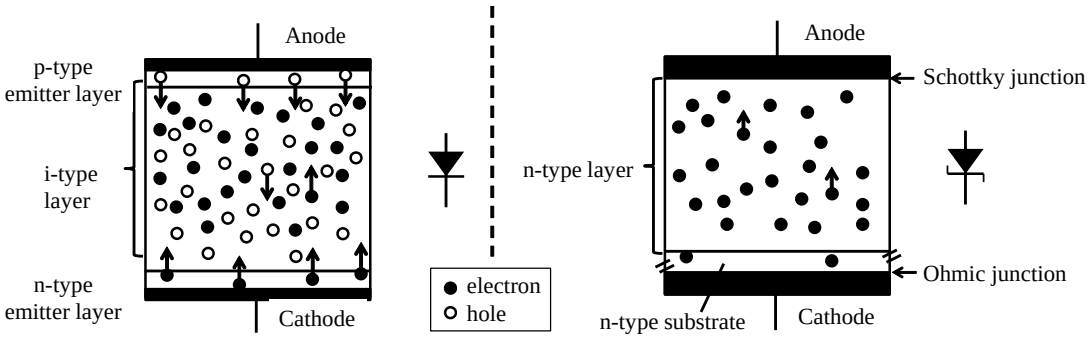

(a) PiN diode (b) Schottky barrier diode

Figure 3.2: The cross-section of PiN diode and Schottky barrier diode

3.2.2 Measured static characteristics

Diode type dependence

This section shows the static characteristics of the studied diodes: they are two Si-PiNDs of STTH8L06 (STMicroelectronics, 600 V, 8 A) and RHRP860 (Fairchild Semiconductor, 600 V, 8 A), and two SiC-SBD of TRS8E65C (Toshiba, 650 V, 8 A) and IDH08SG60C (Infineon, 600 V, 8 A), which have comparable voltage and current ratings.

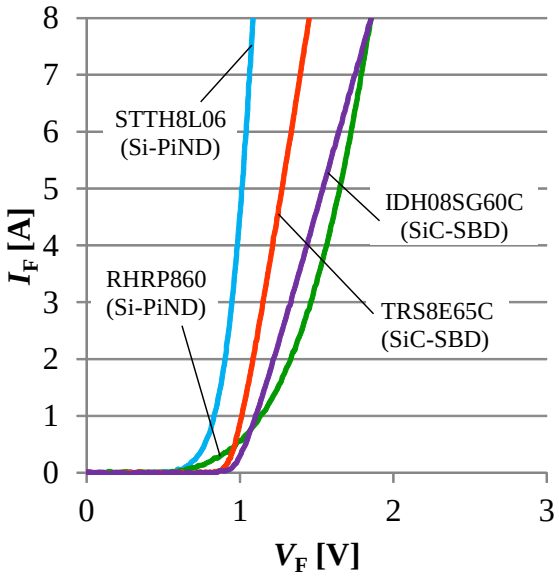

Figure 3.3: Measured $I_F - V_F$ characteristics of diodes (at room temperature)

Fig.3.3 depicts the measured forward current–voltage (I–V) characteristics of the studied diodes at room temperature (25°C) using curve tracer (Agilent B1505). The forward characteristics of both Si-PiND and SiC-SBD show almost the same characteristics except for conductivity modulation, which is the reduction of the resistance resulting from high level of carrier injection for Si-PiND [11].

Fig.3.4 (a) shows the measured capacitance–voltage (C–V) characteristics in the blocking condition using the impedance analyzer (Agilent, 4294A) with a 100 mV, 1 MHz AC measurement signal. The reverse bias voltage dependency of the capacitance is resulted from the depletion of the drift layer in the device. The SiC-SBD has a larger junction capacitance due to a higher impurity concentration

in the drift region [10].

Fig.3.4 (b) shows the measured reverse bias voltage dependency of the equivalent series resistance (ESR) R_S of the diodes in the blocking condition. The ESR of SiC-SBDs are smaller than Si-PiNDs in low reverse bias voltage.

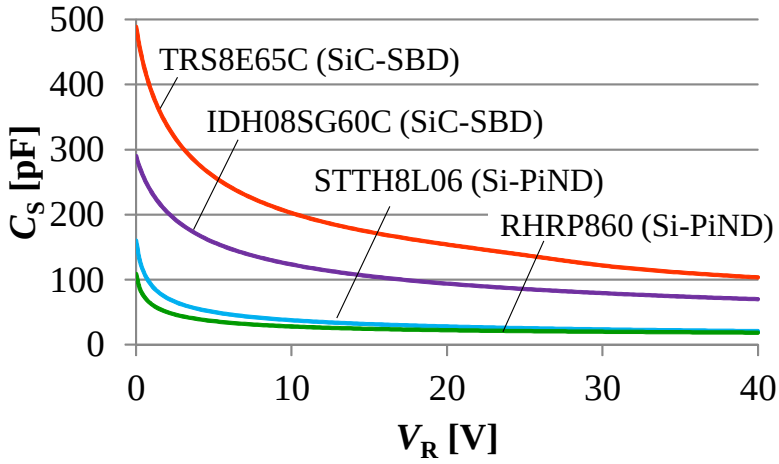

(a) $C_S - V_R$ characteristics

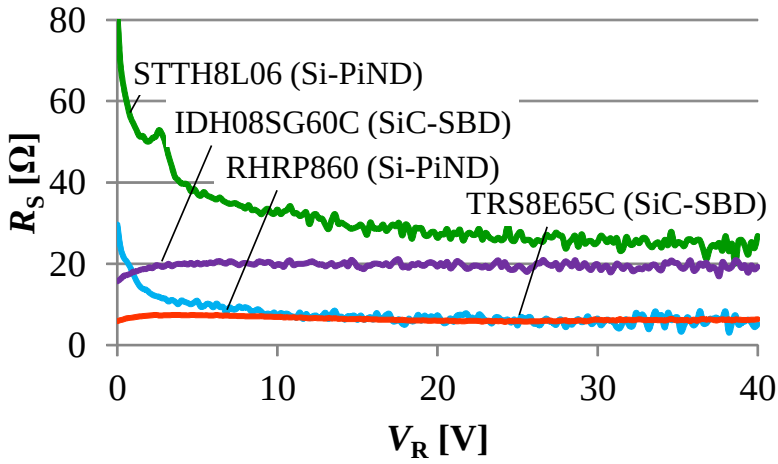

(b) $R_S - V_R$ characteristics

Figure 3.4: Measured $C_S - V_R$ and $R_S - V_R$ characteristics of diodes (at room temperature)

Fig.3.5 shows the die of the studied Si-PiNDs (STTH8L06 and RHRP860) and SiC-SBDs (TRS8E65C and IDH08SG60C). The die size of Si-PiNDs are larger than SiC-SBDs. However, SiC-SBDs have larger junction capacitance than that of Si-PiNDs due to a higher impurity concentration. Fig.3.6 shows the calculated

terminal capacitance per unit area. These results suggest that the terminal capacitance per unit area dependents on the type of diode.

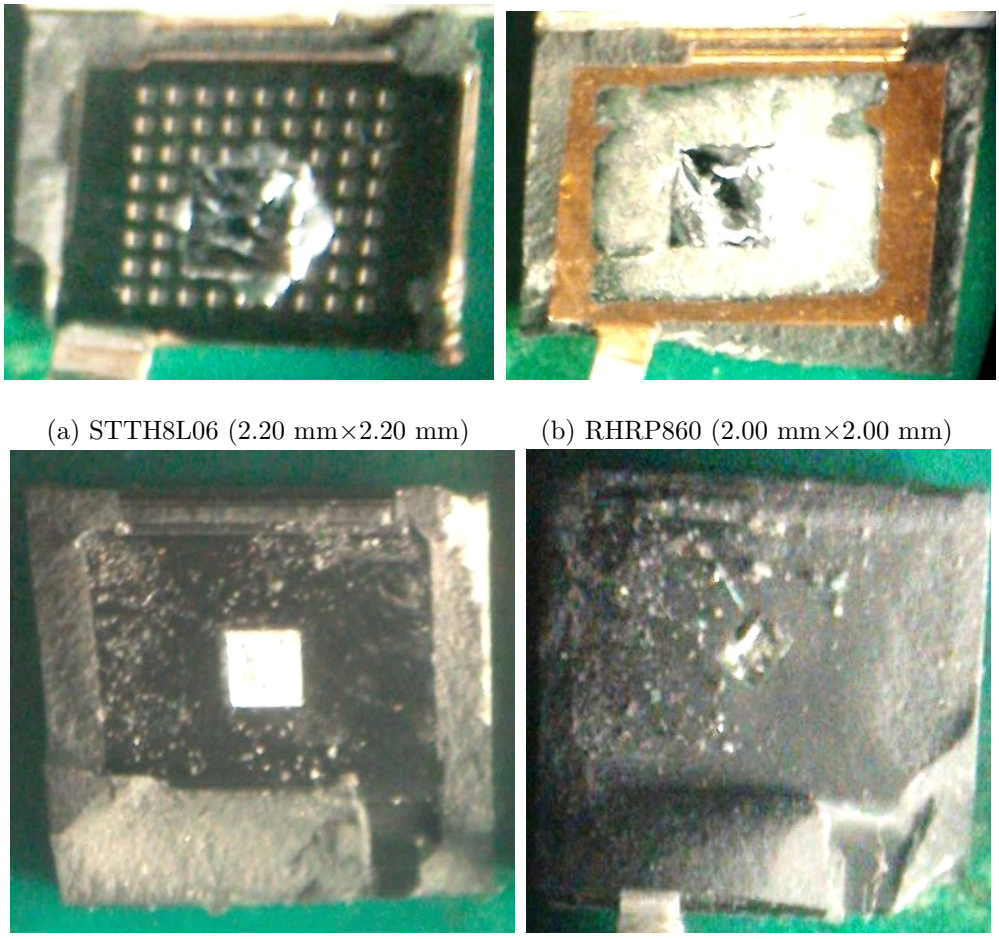

(a) STTH8L06 (2.20 mm×2.20 mm) (b) RHRP860 (2.00 mm×2.00 mm)

(c) TRS8E65C (1.65 mm×1.65 mm) (d) IDH08SG60C (1.15 mm×1.50 mm)

Figure 3.5: Die size of studied Si-PiNDs and SiC-SBDs

Temperature dependence

This section shows the temperature dependence on the static characteristics of the studied Si-PiND (RHRP860) and SiC-SBD (TRS8E65C), which have comparable voltage and current ratings.

Figs.3.7(a) and (b) show the measured temperature dependence in $I_F - V_F$ characteristics of the studied diodes. The knee voltage for both type of diodes decreased with increasing temperature. Moreover, the on-resistance of the SiC-SBD is increased at high temperature, stemming from the carrier mobility reduction

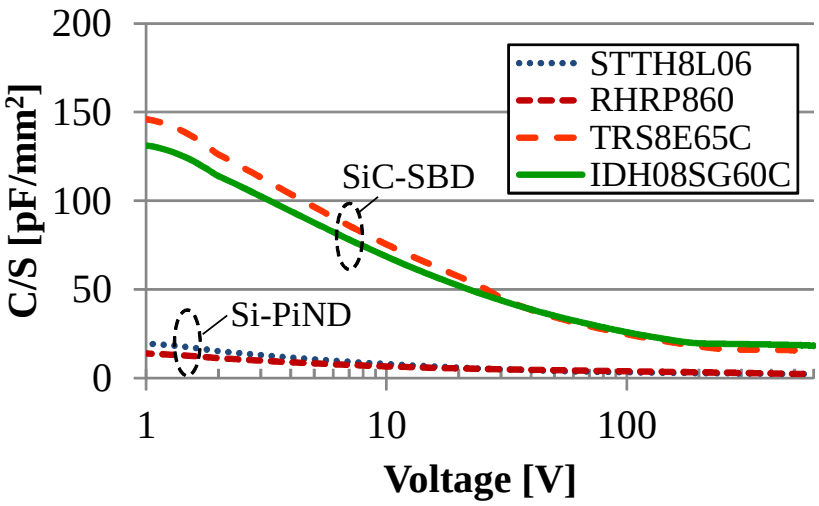

Figure 3.6: Terminal capacitance per unit area

(degradation) [14], whereas life time of minority carrier in Si-PiND counteracts the mobility reduction.

Fig.3.7(c) shows the measured capacitance−voltage (C−V) characteristics in the blocking condition using the semiconductor characterization system (Keithley, 4200-SCS) with a 100 mV, 1 MHz AC measurement signal for different temperatures. The C−V characteristics of the diodes were invariant for the diode temperature.

Fig.3.7(d) shows the measured reverse bias voltage dependency of ESR R_S in the diodes for blocking condition. SiC-SBDs showed lower ESR than Si-PiNDs, which have less voltage dependency and invariance with temperature. ESR of Si-PiNDs increased with temperature, i.e., for the applied 200 V reverse bias voltage, ESR was 57.4 Ω, 99.0 Ω, and 161.9 Ω for 25°C, 100°C, and 175°C, respectively.

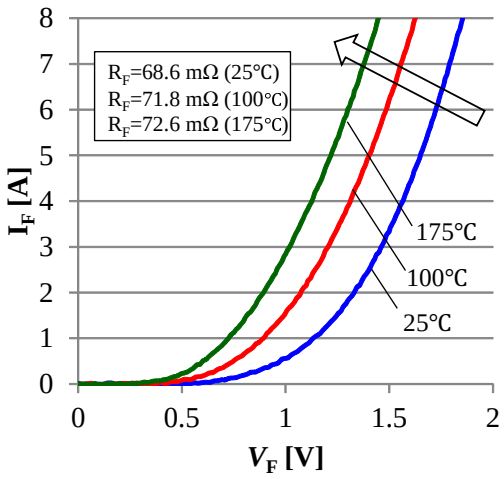

(a) $I_F - V_F$ characteristics (Si-PiND)

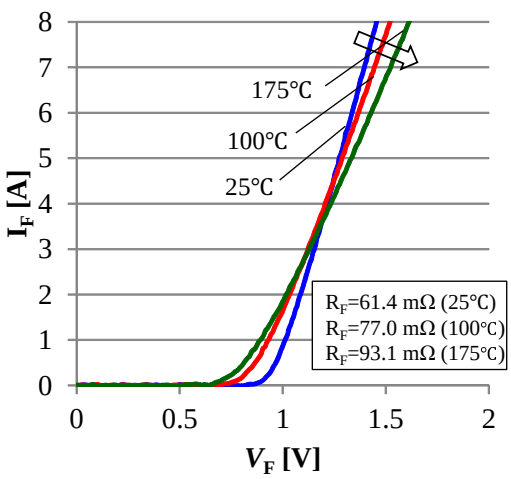

(b) $I_F - V_F$ characteristics (SiC-SBD)

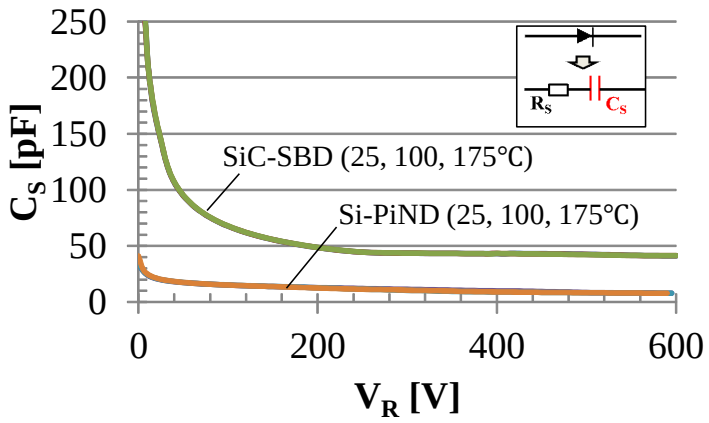

(c) $C_S - V_R$ characteristics

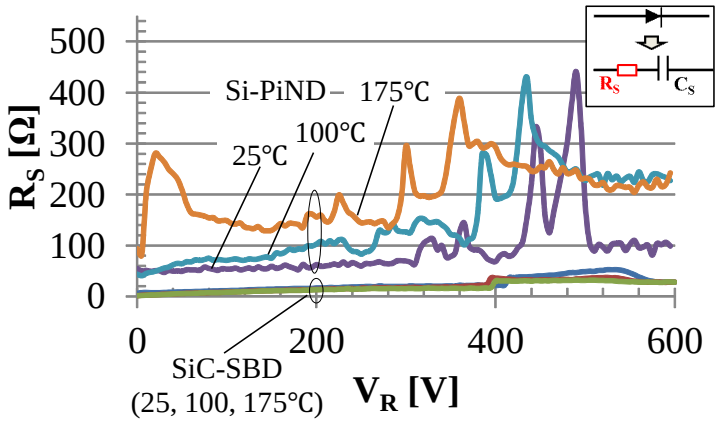

(d) $R_S - V_R$ characteristics

Figure 3.7: Measured static characteristics of diodes (Temperatude dependency)

3.2.3 Turn-off characteristics evaluation

This section experimentally studies the influence of the diode ESR and terminal capacitance on the diode switching characteristics, and compares the difference among diode type.

Fig.3.8 depicts the experimental circuit for double pulse test to evaluate switching characteristics of a diode [10]. The switching operation of metal–oxide–semiconductor field-effect transistor (MOSFET) simultaneously induces the switching operation of the diode. The test sequence is also shown in Fig.3.8.

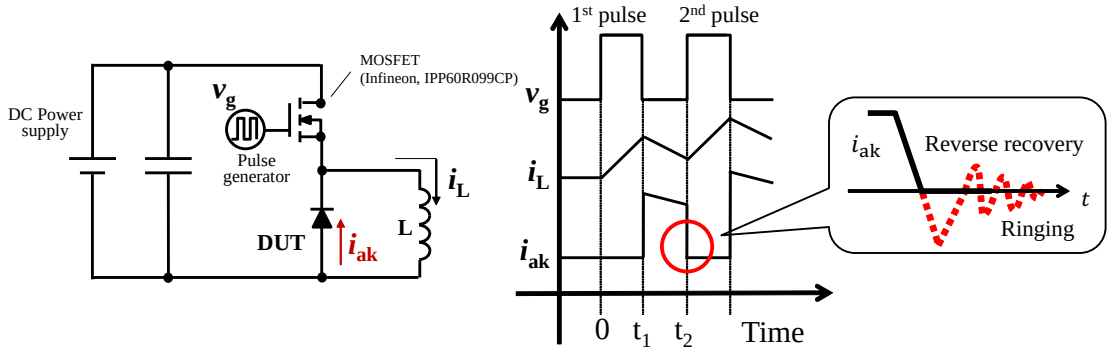

Figure 3.8: Double-pulse test circuit configuration and the test sequence

Fig.3.9 and Fig.3.10 show the measured diode current i_{ak} and reverse voltage v_{ka} of Si-PiND and SiC-SBD for the same turn-off switching operation condition. The diode temperature is given as the parameter 25 °C (room temperature), 100 °C, and 175 °C. The Si-PiND shows reverse recovery phenomena, and the recovery time for STTH8L06 increases from 30 ns to 100 ns with the temperature increases from 25 °C to 175 °C, as shown in Fig.3.9 (a). Sample RHRP860 also shows large reverse current peak, but it has less than half recovery time of STTH8L06. The lower recovery current late ($\frac{di_{ak}}{dt}$) of STTH8L06 than RHRP860 leads to the smaller overshoot voltages.

SiC-SBDs show smaller peak reverse current and shorter recovery time than Si-PiNDs, which do not change with the temperature, as shown in Fig.3.10. Si-PiND RHRP860 shows comparable fast recovery characteristics with SiC SBDs, however the overshoot voltage of SiC-SBDs is smaller than RHRP860 due to smaller reverse current peak. The difference between PiNDs and SBDs is resulting from the

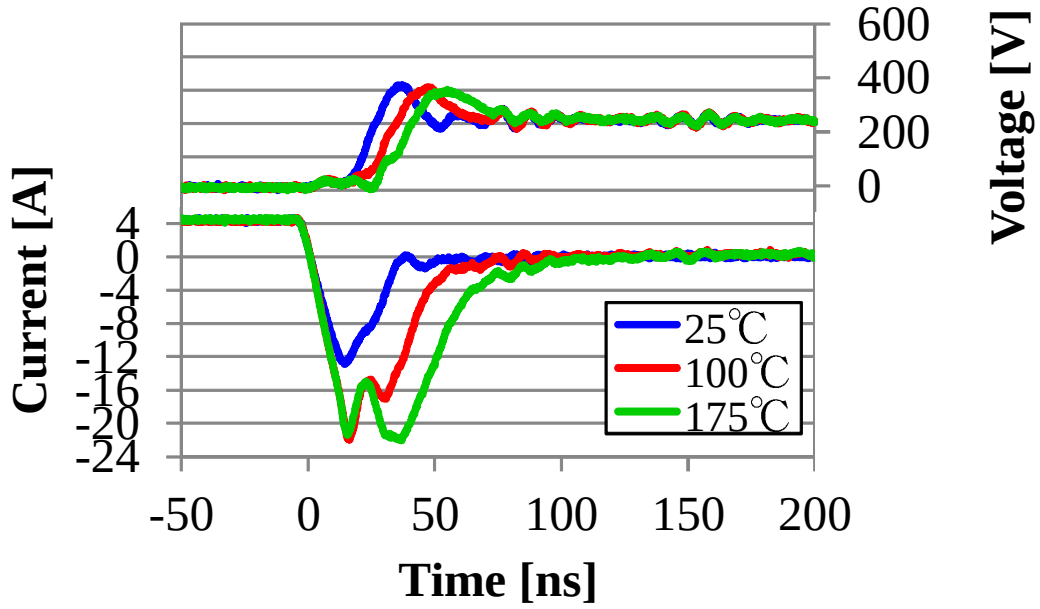

(a) STTH8L06

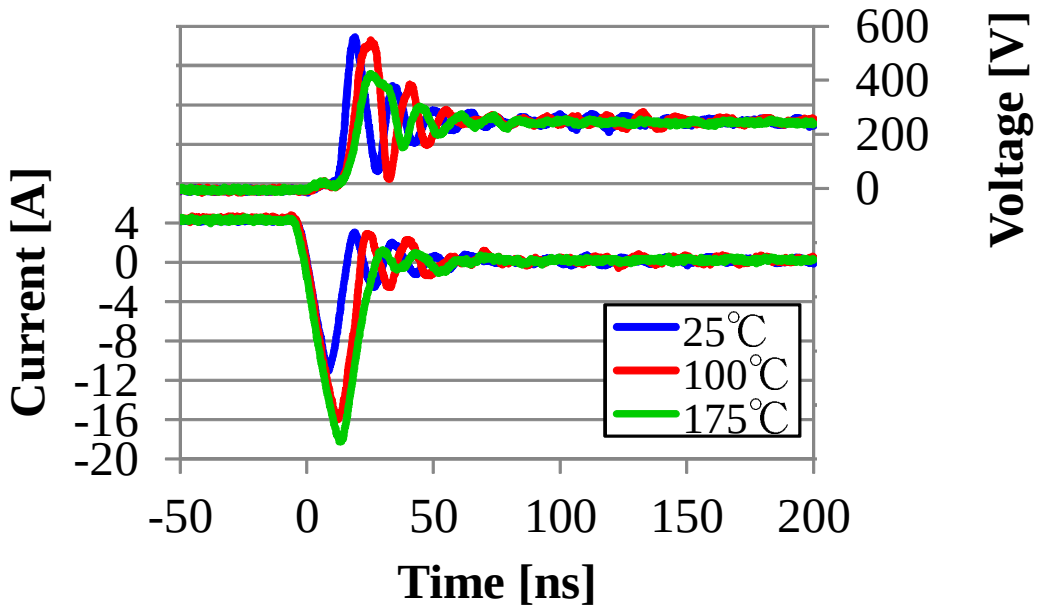

(b) RHRP860

Figure 3.9: Measured diode turn-off characteristics for double-pulse test (Si-PiND)

dominant carrier behavior for conduction. SBDs operate with the majority carrier and do not have stored minority carriers; therefore, it is free from reverse recovery phenomenon and only the depletion charge is observed for turn off operation.

The switching operation of the diode induces ringing oscillation especially in turn-off. The initial amplitude of ringing for SiC-SBDs is relatively small.

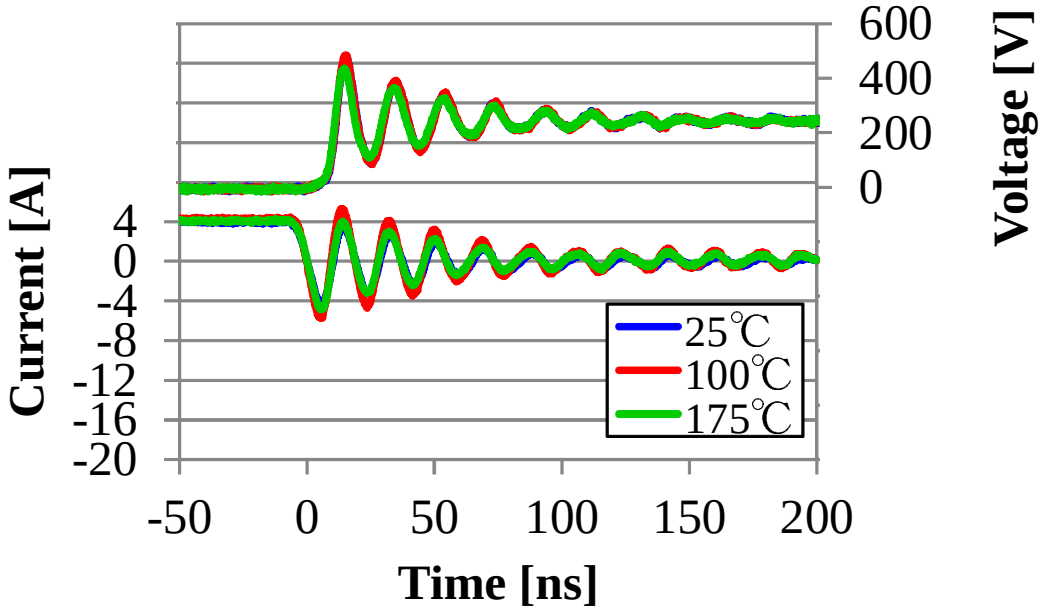

(a) TRS8E65C

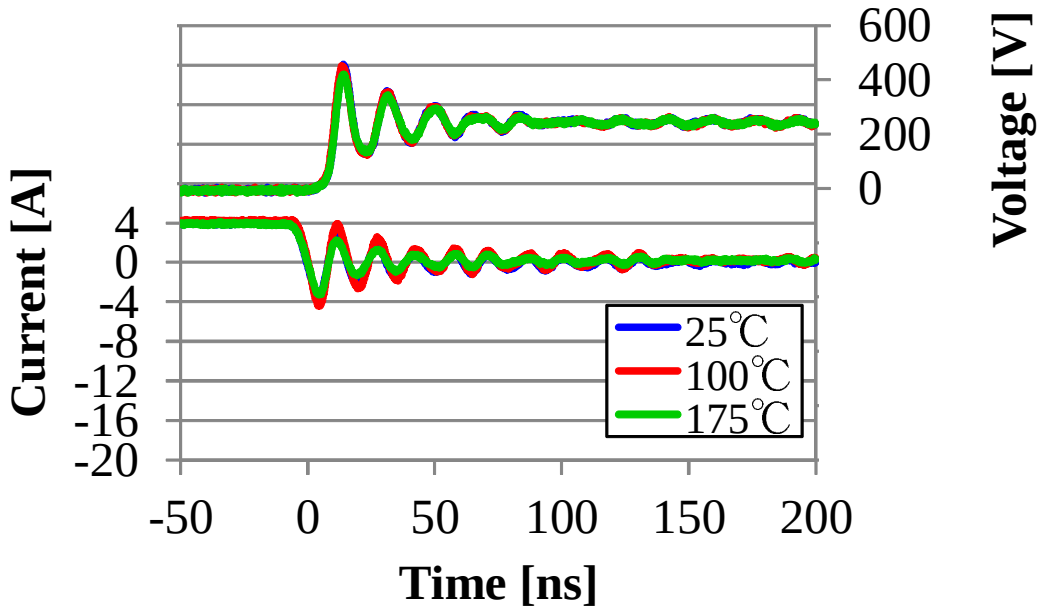

(b) IDH08SG60C

Figure 3.10: Measured diode turn-off characteristics for double-pulse test (SiC-SBD)

However, SiC-SBDs show slower damping in ringing oscillation than Si-PiNDs. TRS8E65C exhibit larger peak current and lower damping than IDH08SG60C. The damping in ringing oscillation of these diodes are determined by the junction capacitance and the ESR in the blocking condition.

3.3 Power diode characterization as EMI noise source

3.3.1 DC-DC boost converter: topology and principle

The equivalent circuit of DC–DC boost converter is shown in Fig.3.11. Its output voltage V_{out} becomes higher than the input voltage V_{in} for steady-state operation. The converter consists of a transistor Q, a diode D_i, a load resistor R_{load}, an inductor L, and a output filter capacitor C. They have parasitic resistance r_L and r_C. Q turns on and off with the switching frequency $f_s = \frac{1}{T}$ for ON duty ratio $D = \frac{t_{on}}{T}$, where t_{on} is the time period to be ON transistor. The output power of a boost converter is usually designed to be between 20 and 400 W [11]. This converter is commonly used as an active power factor corrector (PFC).

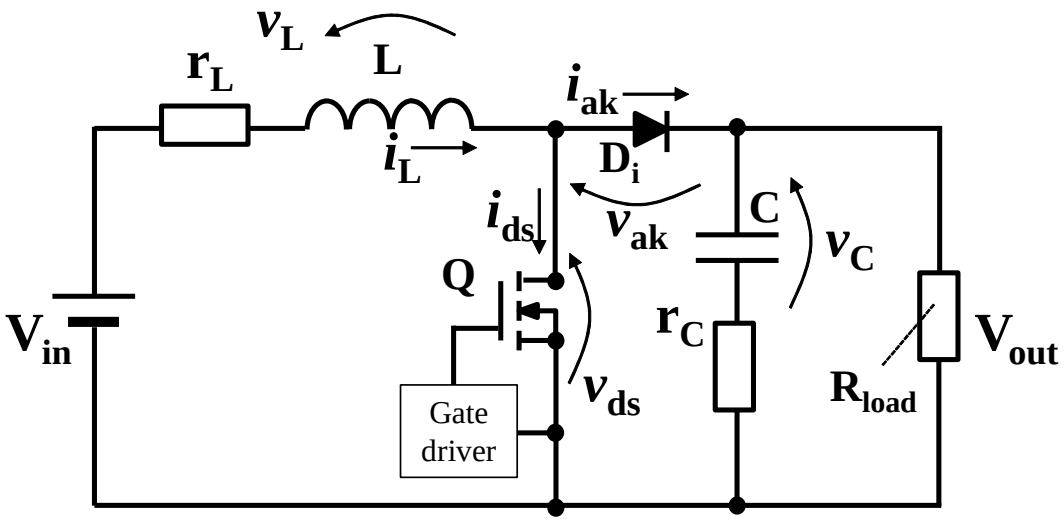

Figure 3.11: Equivalent circuit of DC–DC boost converter

The boost converter can operate in either continuous current mode (CCM) or discontinuous current mode (DCM), whose mode is discriminated with the behavior of the inductor current. Idealized waveforms of the currents and voltages that explain the principle of converter operation are depicted in Fig.3.12 [4]. During the time period $0 < t \leq DT$, the transistor is ON. The voltage across the diode is $v_{ak} = -V_{out}$ during this period. The diode is reverse biased during this period

and the voltage across the inductor is $v_L = V_{in}$. As a result, the inductor current increases linearly with slope $\frac{V_{in}}{L}$. Consequently, the stored magnetic energy in the inductor also increases. The transistor current is equal to the inductor current. At $t = DT$, the transistor turns off with the gate-to-source voltage. The inductor acts as a current source and turns the diode on. The applied voltage across the inductor is $v_L = V_{in} - V_{out} < 0$. Hence, the inductor current decreases with slope $\frac{V_{in}-V_{out}}{L}$. The diode current equals the inductor current. The energy is transferred from the inductor L to the filter capacitor C and the load resistance R_{load} during this period. At time $t = T$, the transistor turns on again, terminating the cycle.

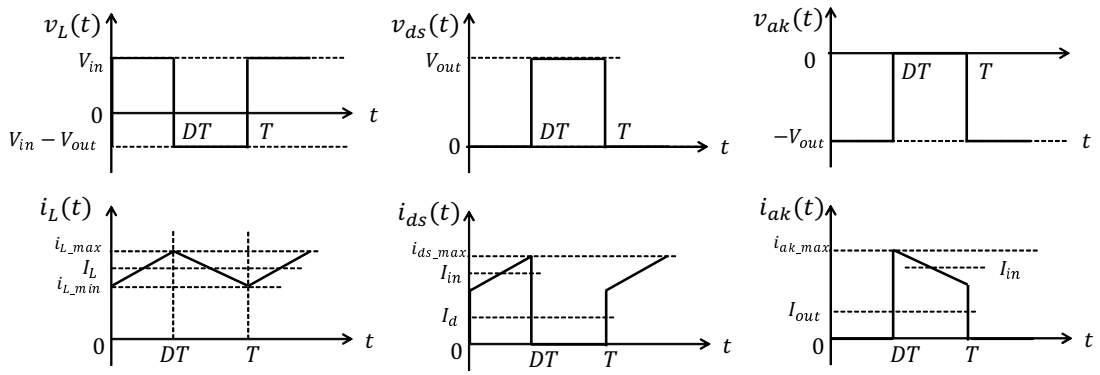

Figure 3.12: Idealized waveforms of the currents and voltages in CCM DC–DC boost converter

The analysis of CCM boost converter uses the following assumptions. The transistor and the diode are ideal switches, that is, the conduction resistance of the transistor and the diode are zero. The terminal capacitance of transistor, the diode capacitance, and lead inductances (and thus switching losses) are zero. Passive components are linear, time-invariant, and frequency-independent. The parasitic resistance of the output capacitor and the inductor are denoted by r_C and r_L, respectively. A state-space representation of a system two vectorial equations:

$$\begin{cases} \dot{\boldsymbol{x}}(t) = \boldsymbol{A}\boldsymbol{x}(t) + \boldsymbol{B}v_{in}(t) \\ v_{out}(t) = \boldsymbol{C}\boldsymbol{x}(t), \end{cases} \tag{3.1}$$

where the coefficients of the matrices $\boldsymbol{A}, \boldsymbol{B}, \boldsymbol{C}$ are functions of the circuit elements. The state variables in the circuit is expressed by state-space vector $\boldsymbol{x}$= $[i_L, v_c]$.

Kirchhoff's voltage law (KVL) is applied to the inductor and capacitor loops in the transistor ON state, which becomes [4]

$$\begin{cases} v_{in} = L\frac{di_L}{dt} + r_L i_L \\ v_C + r_C C\frac{dv_C}{dt} + R_{load} C\frac{dv_C}{dt} = 0 \end{cases} \tag{3.2}$$

with $v_{out} = -R_{load} C\frac{dv_C}{dt}$. It leads to the state-space equations of the transistor ON state circuit:

$$\frac{d}{dt}\begin{bmatrix} i_L \\ v_C \end{bmatrix} = \begin{bmatrix} -\frac{r_L}{L} & 0 \\ 0 & -\frac{1}{C(R_{load}+r_C)} \end{bmatrix}\begin{bmatrix} i_L(t) \\ v_C(t) \end{bmatrix} + \begin{bmatrix} \frac{1}{L} \\ 0 \end{bmatrix} v_{in} \tag{3.3}$$

$$v_{out} = -R_{load}\left(-\frac{v_C}{R_{load}+r_C}\right) = \begin{bmatrix} 0 & \frac{R_{load}}{R_{load}+r_C} \end{bmatrix}\begin{bmatrix} i_L(t) \\ v_C(t) \end{bmatrix}, \tag{3.4}$$

where

$$\boldsymbol{A_1} = \begin{bmatrix} -\frac{r_L}{L} & 0 \\ 0 & -\frac{1}{C(R_{load}+r_C)} \end{bmatrix}, \boldsymbol{B_1} = \begin{bmatrix} \frac{1}{L} \\ 0 \end{bmatrix}, \boldsymbol{C_1} = \begin{bmatrix} 0 & \frac{R_{load}}{R_{load}+r_C} \end{bmatrix}.$$

KVL for the transistor OFF state results in

$$\begin{cases} v_{in} = L\frac{di_L}{dt} + r_L i_L + v_C + r_C C\frac{dv_c}{dt} \\ v_C + r_C C\frac{dv_C}{dt} - R_{load}\left(i_L - C\frac{dv_C}{dt}\right) = 0 \end{cases} \tag{3.5}$$

with $v_{out} = R_{load}\left(i_L - C\frac{dv_C}{dt}\right)$. It leads to the state-space equations of the transistor OFF state circuit:

$$\frac{d}{dt}\begin{bmatrix} i_L \\ v_C \end{bmatrix} = \begin{bmatrix} -\frac{r_L+\frac{R_{load}r_C}{R_{load}+r_C}}{L} & -\frac{R_{load}}{L(R_{load}+r_C)} \\ \frac{R_{load}}{C(R_{load}+r_C)} & -\frac{1}{C(R_{load}+r_C)} \end{bmatrix}\begin{bmatrix} i_L(t) \\ v_C(t) \end{bmatrix} + \begin{bmatrix} \frac{1}{L} \\ 0 \end{bmatrix} v_{in} \tag{3.6}$$

$$v_{out} = \begin{bmatrix} \frac{R_{load}r_C}{R_{load}+r_C} & \frac{R_{load}}{R_{load}+r_C} \end{bmatrix}\begin{bmatrix} i_L(t) \\ v_C(t) \end{bmatrix}, \tag{3.7}$$

which becomes the state-space matrices for this circuit topology as:

$$\boldsymbol{A_2} = \begin{bmatrix} -\frac{r_L+\frac{R_{load}r_C}{R_{load}+r_C}}{L} & -\frac{R_{load}}{L(R_{load}+r_C)} \\ \frac{R_{load}}{C(R_{load}+r_C)} & -\frac{1}{C(R_{load}+r_C)} \end{bmatrix}, \boldsymbol{B_2} = \begin{bmatrix} \frac{1}{L} \\ 0 \end{bmatrix}, \boldsymbol{C_2} = \begin{bmatrix} \frac{R_{load}r_C}{R_{load}+r_C} & \frac{R_{load}}{R_{load}+r_C} \end{bmatrix}.$$

The averaged state-space equations can be calculated as followings.

$$\begin{aligned} A_{ave} &= \begin{bmatrix} -\frac{r_L D + \left(r_L + \frac{R_{load} r_C}{R_{load}+r_C}\right)(1-D)}{L} & -\frac{R_{load}(1-D)}{L(R_{load}+r_C)} \\ \frac{R_{load}(1-D)}{C(R_{load}+r_C)} & -\frac{D}{C(R_{load}+r_C)} - \frac{(1-D)}{C(R_{load}+r_C)} \end{bmatrix} \\ &= \begin{bmatrix} -\frac{r_L + \frac{R_{load} r_C}{R_{load}+r_C}(1-D)}{L} & -\frac{R_{load}(1-D)}{L(R_{load}+r_C)} \\ \frac{R_{load}(1-D)}{C(R_{load}+r_C)} & -\frac{1}{C(R_{load}+r_C)} \end{bmatrix} \end{aligned} \tag{3.8}$$

$$B_{ave} = \begin{bmatrix} \frac{1}{L} \\ 0 \end{bmatrix} D + \begin{bmatrix} \frac{1}{L} \\ 0 \end{bmatrix} (1-D) = \begin{bmatrix} \frac{1}{L} \\ 0 \end{bmatrix} \tag{3.9}$$

$$C_{ave} = \begin{bmatrix} \frac{R_{load} r_C}{R_{load}+r_C}(1-D) & \frac{R_{load}}{R_{load}+r_C} D + \frac{R_{load}}{R_{load}+r_C}(1-D) \end{bmatrix} = \begin{bmatrix} \frac{R_{load} r_C}{R_{load}+r_C}(1-D) & \frac{R_{load}}{R_{load}+r_C} \end{bmatrix} \tag{3.10}$$

The averaged solution is given as $X = -A_{ave}^{-1} B_{ave} V_{in}$.

$$\begin{aligned} X &= -\begin{bmatrix} -\frac{r_L + \frac{R_{load} r_C}{R_{load}+r_C}(1-D)}{L} & -\frac{R_{load}(1-D)}{L(R_{load}+r_C)} \\ \frac{R_{load}(1-D)}{C(R_{load}+r_C)} & -\frac{1}{C(R_{load}+r_C)} \end{bmatrix}^{-1} \begin{bmatrix} \frac{1}{L} \\ 0 \end{bmatrix} V_{in} \\ &= -\frac{1}{\frac{r_L + \frac{R_{load} r_C}{R_{load}+r_C}(1-D)}{LC(R_{load}+r_C)} + \frac{R_{load}^2 (1-D)^2}{LC(R_{load}+r_C)^2}} \begin{bmatrix} -\frac{1}{C(R_{load}+r_C)} & \frac{R_{load}(1-D)}{L(R_{load}+r_C)} \\ -\frac{R_{load}(1-D)}{C(R_{load}+r_C)} & -\frac{r_L + \frac{R_{load} r_C}{R_{load}+r_C}(1-D)}{L} \end{bmatrix} \begin{bmatrix} \frac{1}{L} \\ 0 \end{bmatrix} V_{in} \\ &= \frac{1}{r_L + \frac{R_{load} r_C}{R_{load}+r_C}(1-D) + \frac{R_{load}^2 (1-D)^2}{R_{load}+r_C}} \begin{bmatrix} 1 \\ R(1-D) \end{bmatrix} V_{in} \end{aligned} \tag{3.11}$$

$$I_{L_{ave}} = \frac{V_{in}}{r_L + \frac{R_{load} r_C}{R_{load}+r_C}(1-D) + \frac{R_{load}^2 (1-D)^2}{R_{load}+r_C}} \tag{3.12}$$

$$V_{C_{ave}} = \frac{R_{load}(1-D) V_{in}}{r_L + \frac{R_{load} r_C}{R_{load}+r_C}(1-D) + \frac{R_{load}^2 (1-D)^2}{R_{load}+r_C}} \tag{3.13}$$

The output voltage is then calculated with $V_{out} = C_{ave} X$.

$$\begin{aligned} V_{out} &= \begin{bmatrix} \frac{R_{load} r_C}{R_{load}+r_C}(1-D) & \frac{R_{load}}{R_{load}+r_C} \end{bmatrix} \frac{V_{in}}{r_L + \frac{R_{load} r_C}{R_{load}+r_C}(1-D) + \frac{R_{load}^2 (1-D)^2}{R_{load}+r_C}} \begin{bmatrix} 1 \\ R_{load}(1-D) \end{bmatrix} \\ &= \frac{R_{load}(1-D) V_{in}}{r_L + \frac{R_{load} r_C}{R_{load}+r_C}(1-D) + \frac{R_{load}^2 (1-D)^2}{R_{load}+r_C}} \end{aligned} \tag{3.14}$$

$$M = \frac{V_{out}}{V_{in}} = \frac{1}{1-D} \frac{R_{load}(1-D)^2}{r_L + \frac{R_{load} r_C}{R_{load}+r_C}(1-D) + \frac{R_{load}^2 (1-D)^2}{R_{load}+r_C}} \tag{3.15}$$

The DC voltage gain and the average inductor current can be expressed as follows by neglecting the parasitic DC resistance r_C, r_L.

$$M = \frac{V_{out}}{V_{in}} = \frac{1}{1-D} \tag{3.16}$$

$$I_{L_{ave}} = I_{in_{ave}} = \frac{V_{in}}{R_{load}(1-D)^2} \tag{3.17}$$

3.3.2 Diode type and temperature dependency of switching characteristics

Fig.3.13 depicts the circuit diagram of the experimental CCM boost converter. The MOSFET (Infineon, IPP60R099CP) was operated with 100 kHz switching frequency by 50% duty cycle for 100 V DC input voltage and 75 Ω load resistance. A battery was used as the power supply of the gate driver to isolate the noise path of the power supply to the gate driver. This section experimentally evaluates the reverse recovery behavior of the Si-PiND and SiC-SBD in the CCM DC−DC boost converter, and studies the effect of diode dynamic characteristics on the conducted emission.

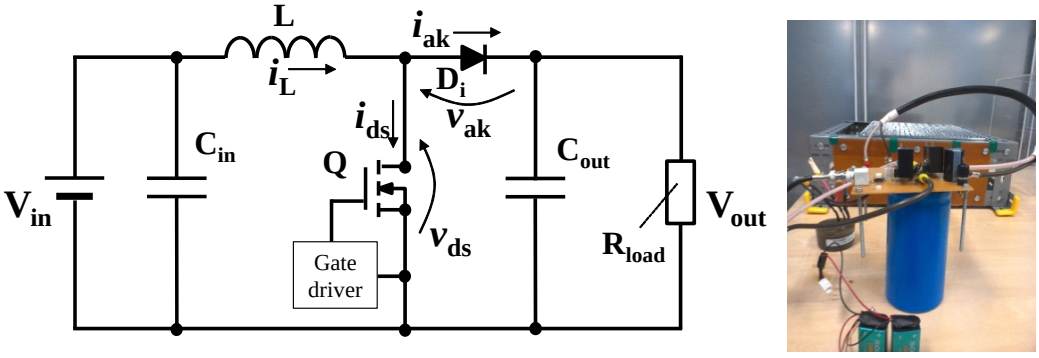

Figure 3.13: Experimental circuit configuration

Measured current and voltage in the experimental converter are depicted in Fig.3.14. The diode turns off when the MOSFET Q is turned on, and inductor current commutates from the diode to the MOSFET.

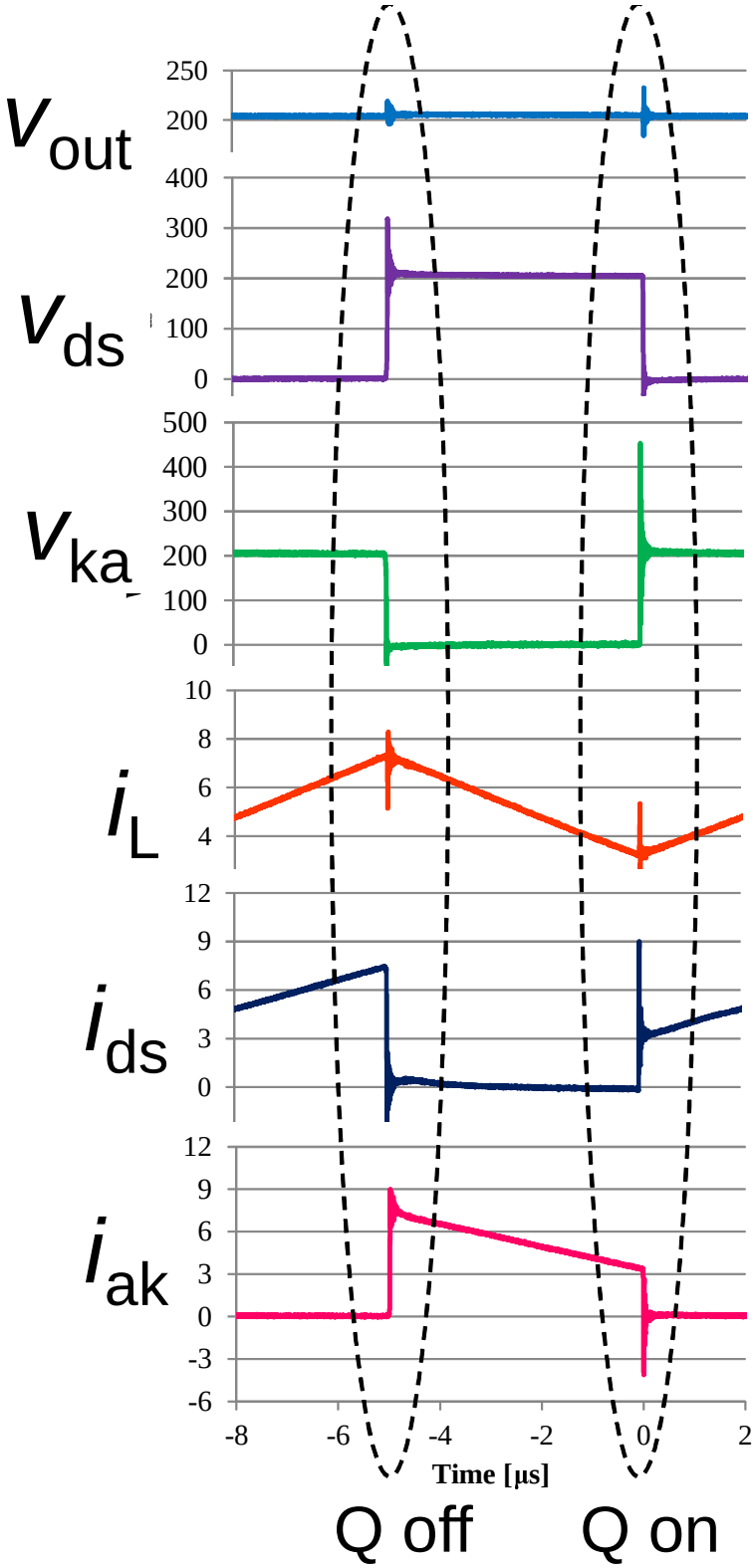

Figure 3.14: Measured voltage and current waveform in DC–DC boost converter (for SiC-SBD)

Diode type dependence

Fig.3.15 and Fig.3.16 show the measured diode and MOSFET current and voltage for turn-off of MOSFET in a CCM DC-DC boost converter at room temperature. The turn-on behavior of the diode and turn-off behavior of the MOSFET are almost unaffected by the type of diode. Fig.3.17 and Fig.3.18 show the measured reverse recovery behavior of the diodes and turn-on behavior of the MOSFET. The measured current of the Si-PiND for turn-off operation in Fig.3.17(a) shows the characteristic of bipolar devices with large peak reverse current. SBD shows a lower peak reverse current and a shorter recovery time than PiNDs. The peak drain current in turn-on operation of MOSFET is considerably larger for Si-PiND than SBD as can be seen in Fig.3.18(a). This large peak of i_{ds} also leads to a significant switching loss of MOSFET.

Temperature dependence

Fig.3.19 and Fig.3.20 show the measured diode anode to cathode current i_{ak} and voltage v_{ak} for the Si-PiND and SiC-SBD under the same switching operation. The diode temperature is given as parameter 25°C (room temperature), 100°C, and 175°C. The turn-on behavior of the diode is independent of the diode type and operation temperature, as shown in Fig.3.19(b) and Fig.3.20(b). SiC-SBD shows a lower peak reverse current and a shorter recovery time than Si-PiND and remained nearly the same with the temperature, as shown in Fig.3.20(a). The SBD operates with the majority carrier and does not have stored minority carriers; therefore, it is free from reverse recovery phenomena, and only the depletion charge is observed for the turn-off operation. Conversely, the Si-PiND shows reverse recovery phenomena, and the peak value of the reverse recovery current increases with temperature, as shown in Fig.3.19(a). The recovery time increases from 20 ns to 70 ns as the temperature increases from 25°C to 175°C. The switching operation of the diode induces ringing oscillation. The settling of the ringing oscillation in turn-off operation at 175°C is less than half that of at 25°C for Si-PiND.

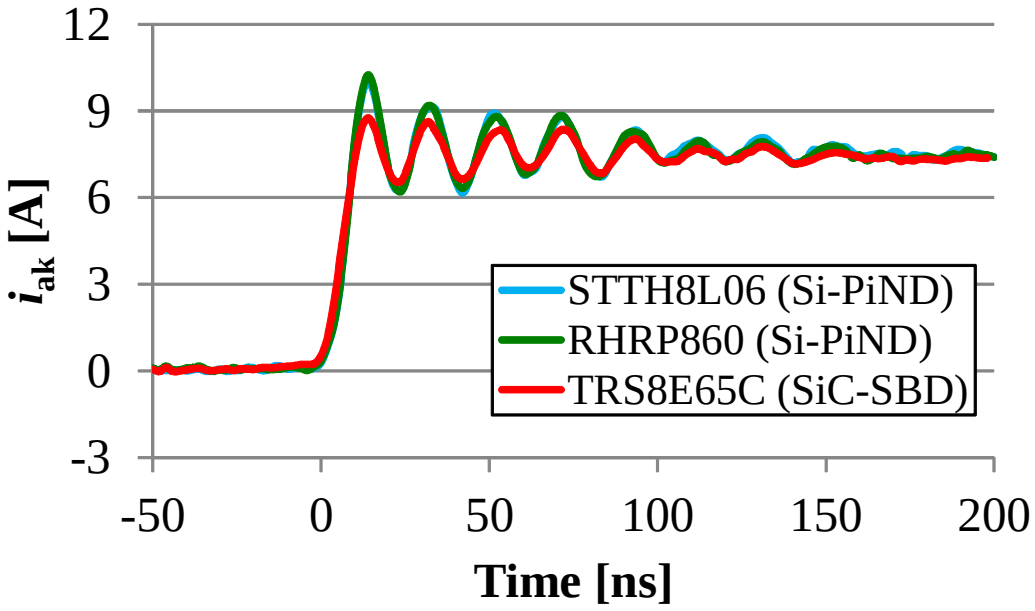

(a) Diode current

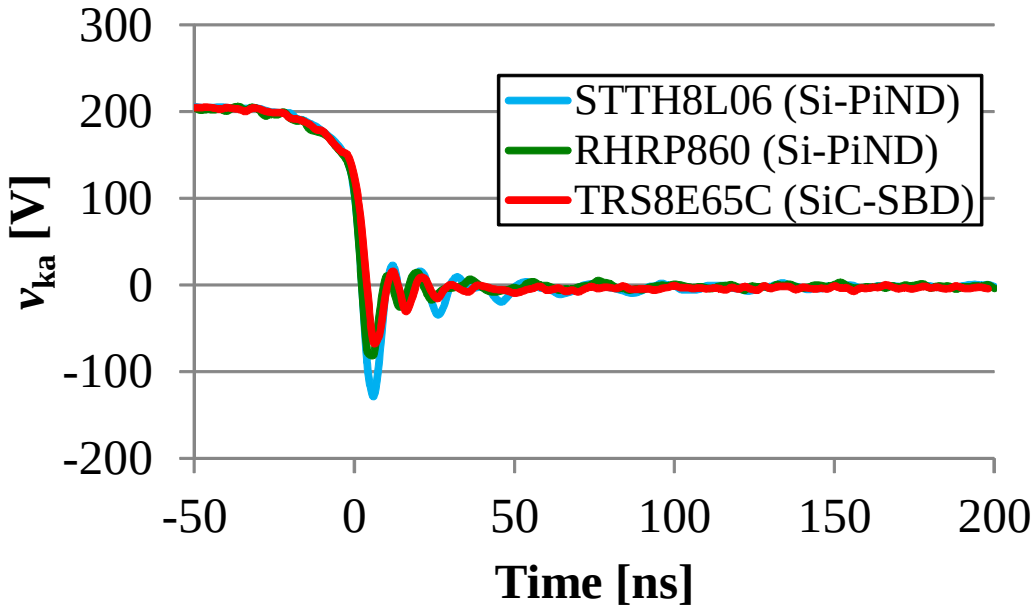

(b) Diode voltage

Figure 3.15: Measured diode current and voltage (MOSFET turn-off)

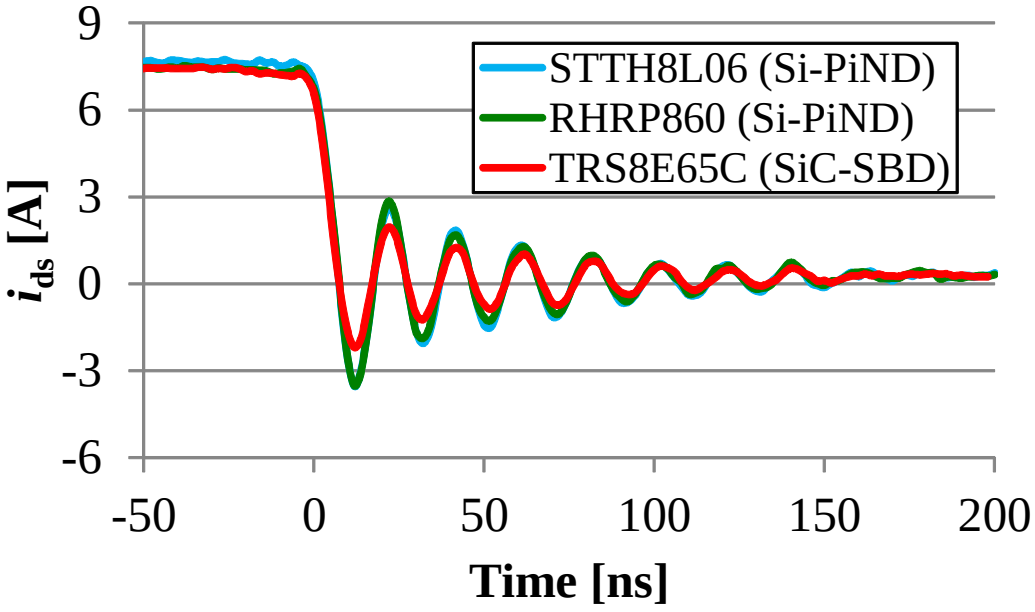

(a) Drain current

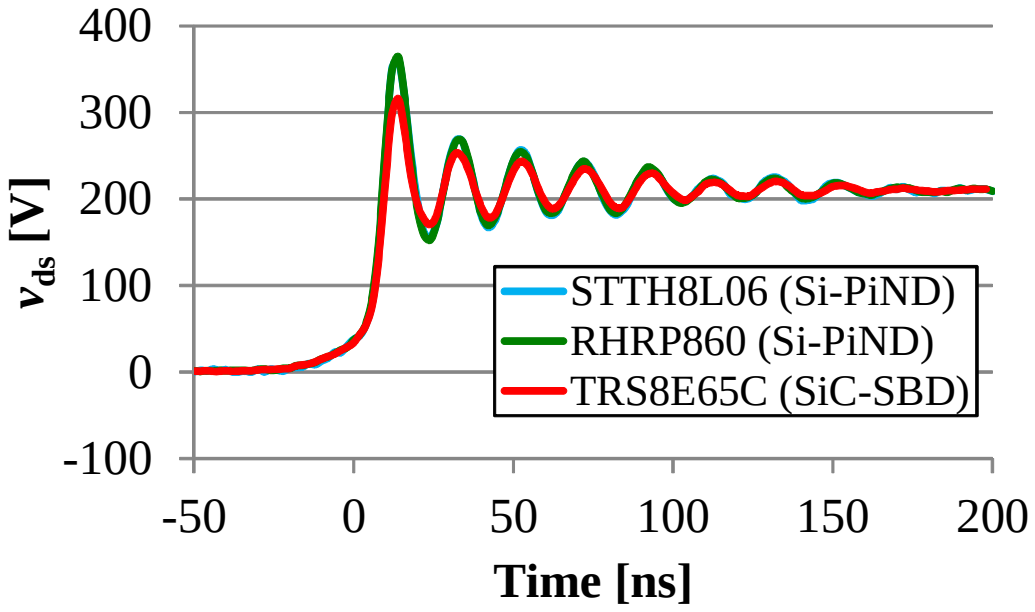

(b) Drain to source voltage

Figure 3.16: Measured MOSFET current and voltage (MOSFET turn-off)

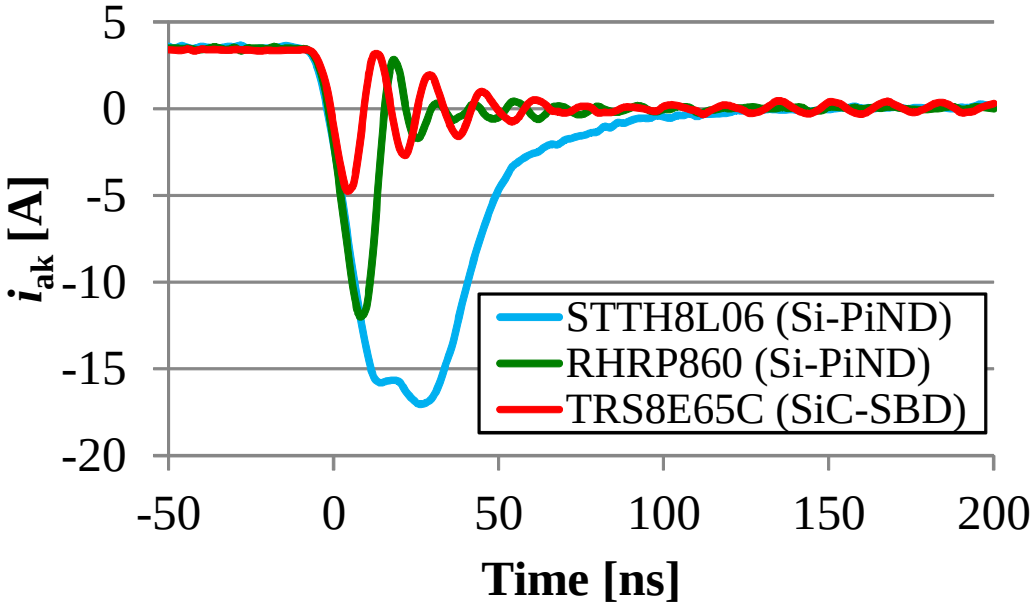

(a) Diode current

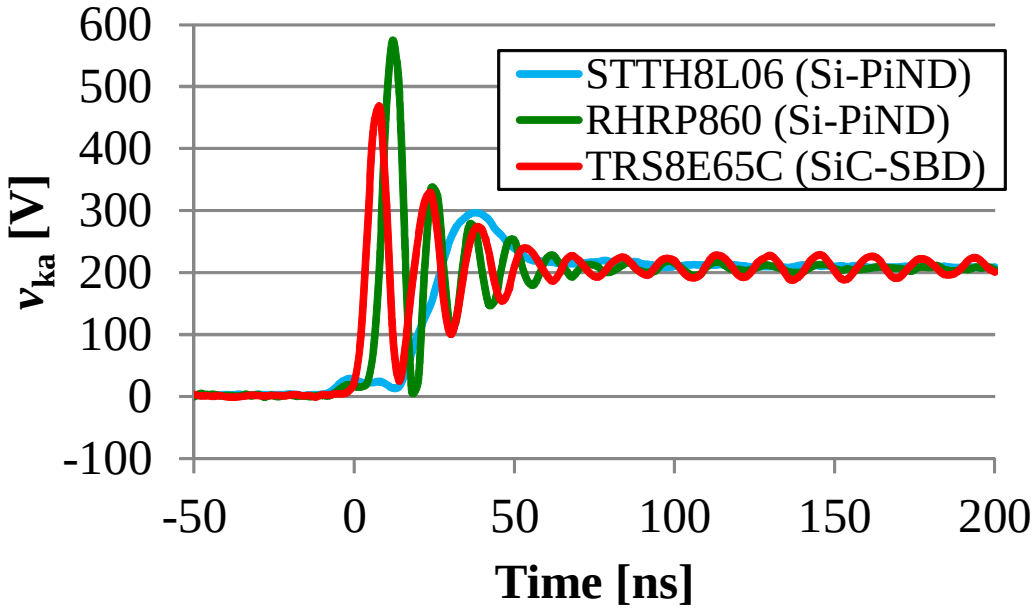

(b) Diode voltage

Figure 3.17: Measured diode current and voltage (MOSFET turn-on)

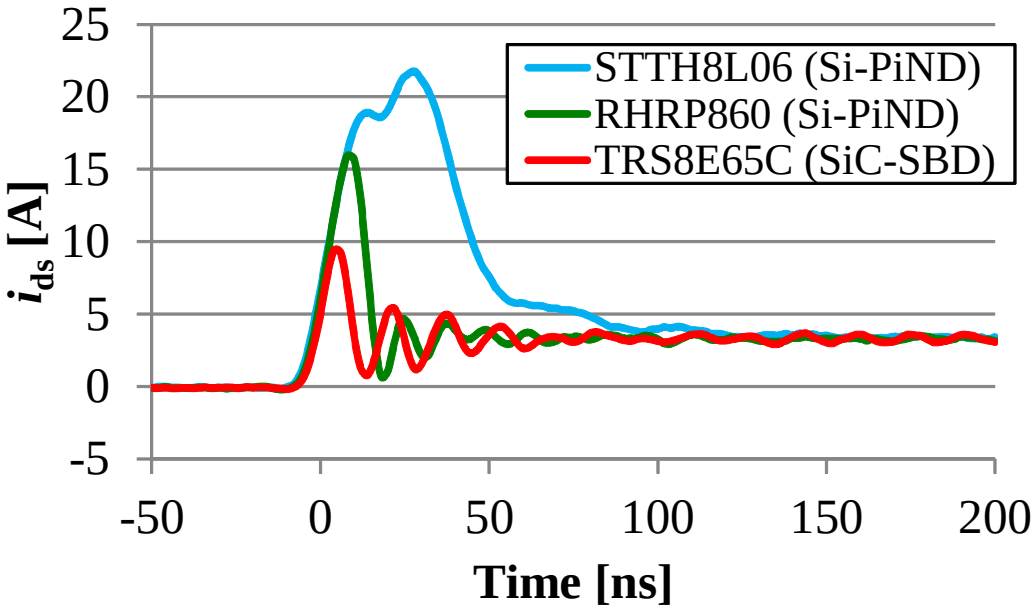

(a) Drain current

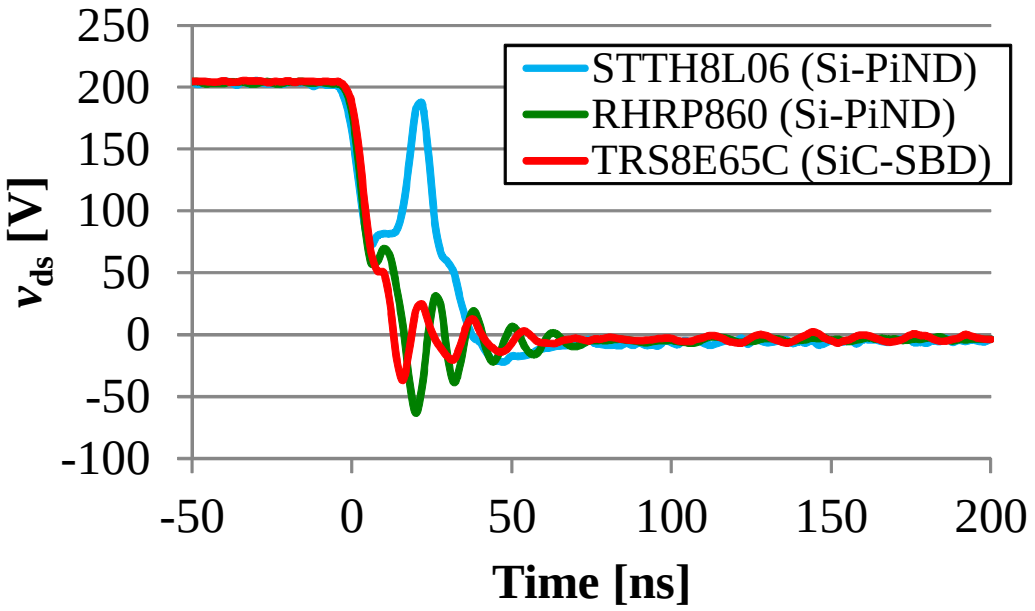

(b) Drain to source voltage

Figure 3.18: Measured MOSFET current and voltage (MOSFET turn-on)

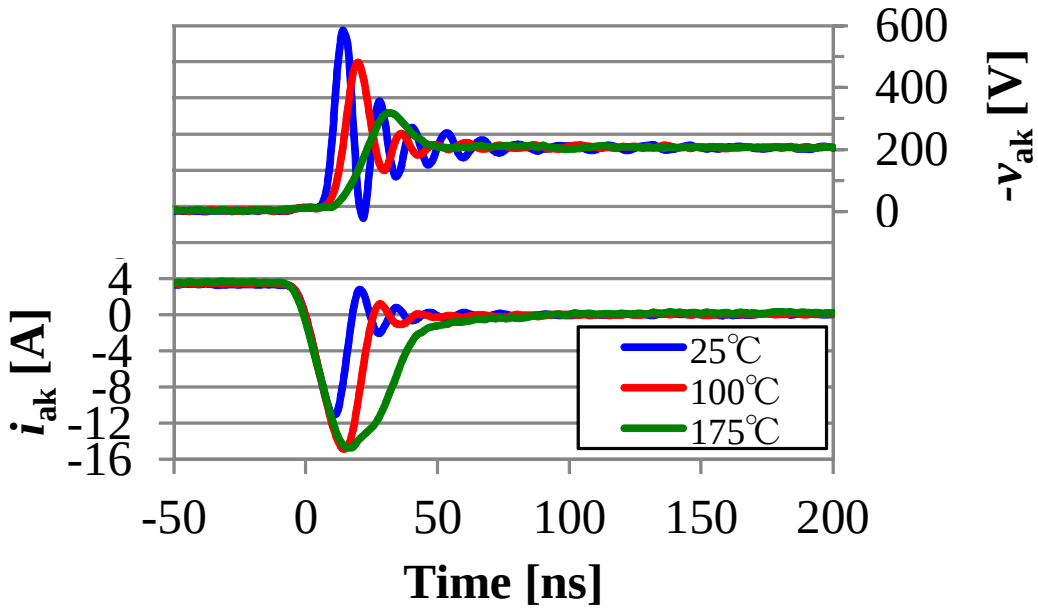

(a) turn off

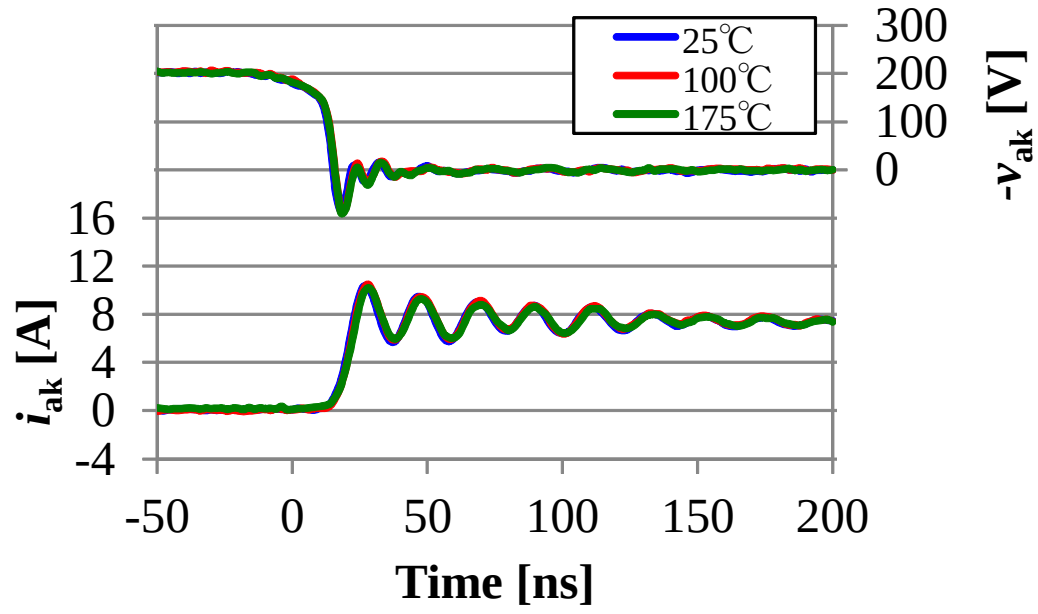

(b) turn on

Figure 3.19: Measured diode current and voltage (temperature depedency, Si-PiND)

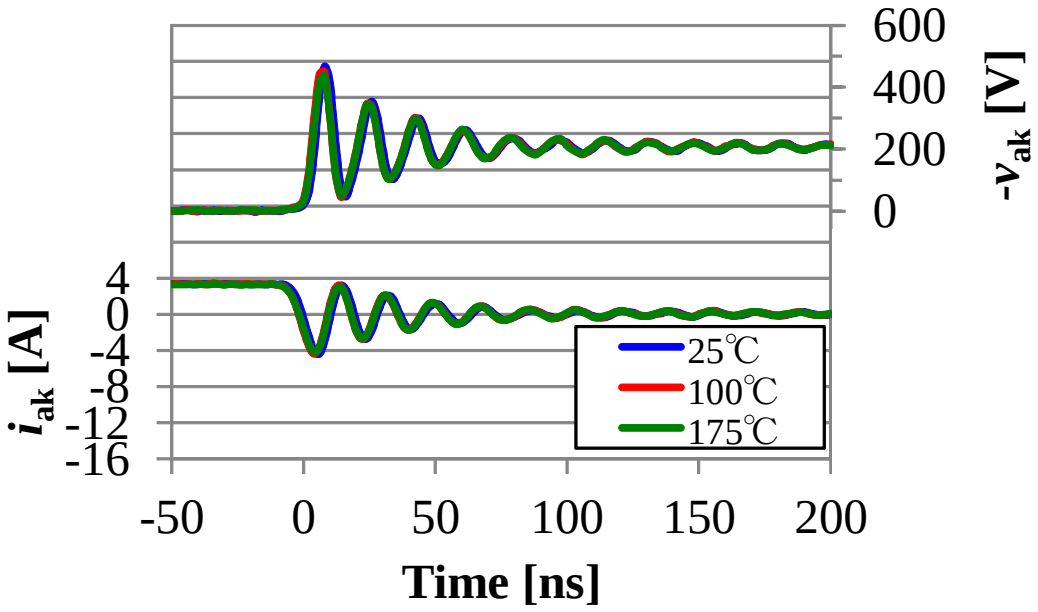

(a) turn off

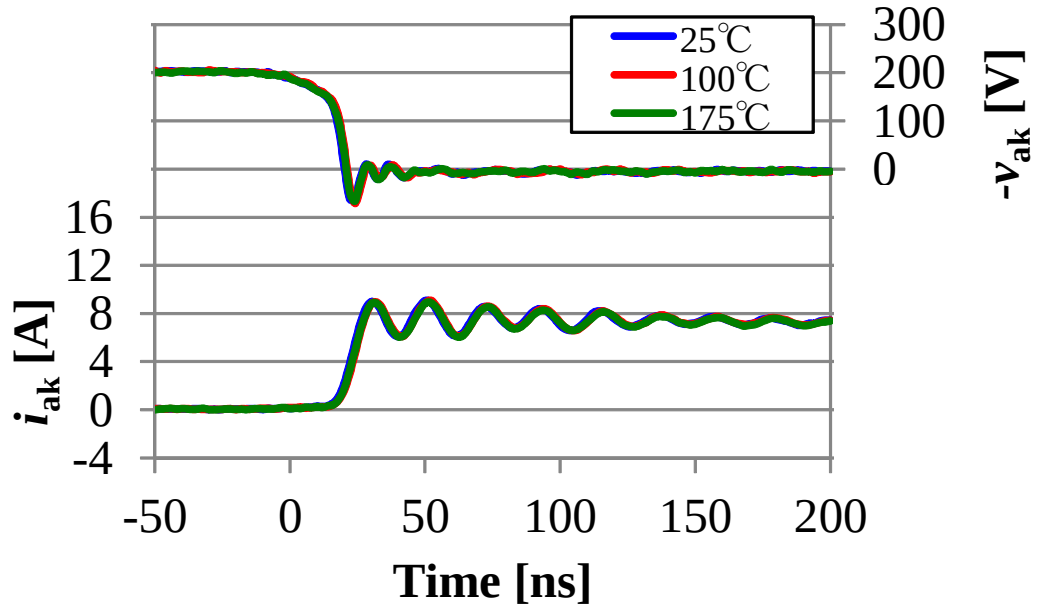

(b) turn on

Figure 3.20: Measured diode current and voltage (temperature depedency, SiC-SBD)

3.3.3 Evaluation of diode turn-off characteristics based on Prony's method

Prony analysis is applied to identify the damping, frequency, magnitude, and initial phase information of the oscillation modes from the sampled time-domain data [41]–[45]. This study models the ringing oscillation as the damped oscillation of the second order dynamical system to the step input. This section applies Prony analysis to the measured time-domain data to evaluate the oscillation frequency, damping factor, and initial value of the ringing oscillation mode.

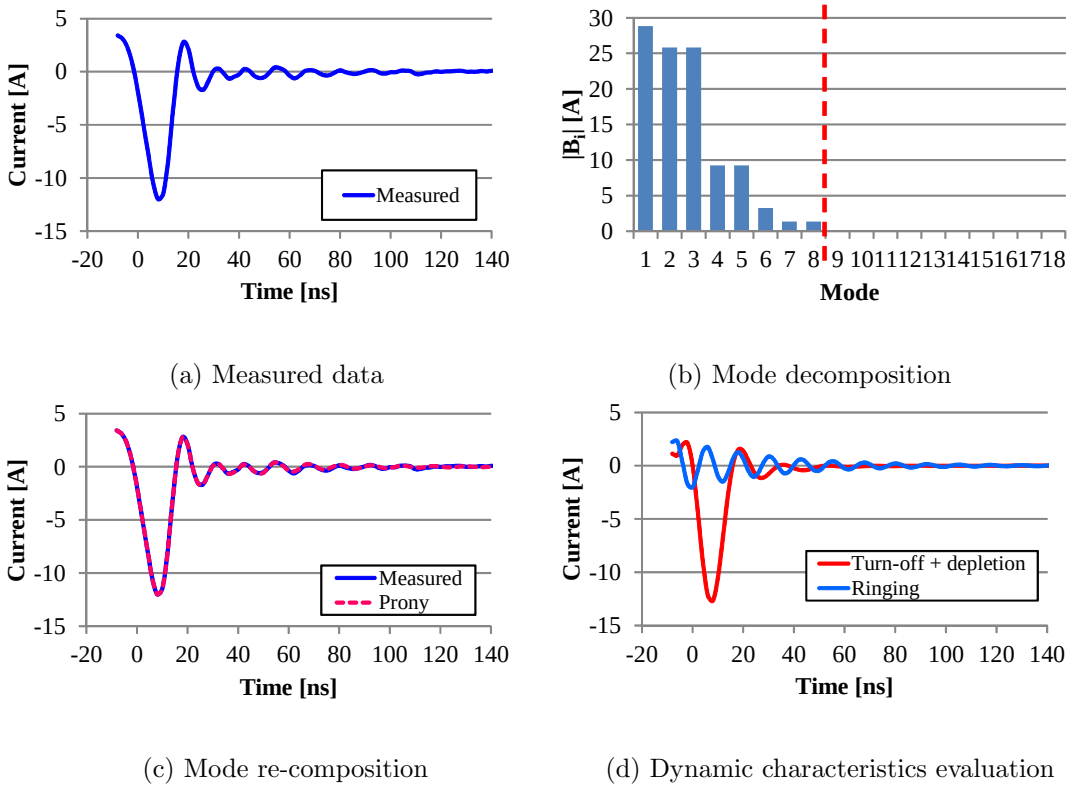

(a) Measured data

(b) Mode decomposition

(c) Mode re-composition

(d) Dynamic characteristics evaluation

Figure 3.21: Characterization of transient response by Prony's method

A measured diode turn-off current is depicted as Fig.3.21(a). Prony analysis is applied to the data for 140ns, a range that contains the whole dynamic behavior. The dominant modes are extracted with large signal residue $|B_i|$ as shown in Fig.3.21(b). The reproduced dynamic behavior of the dominant mode shown in Fig.3.21(c) as a dashed pink line corresponds to the measured data. Fig.3.21(d) shows the extracted dominant modes from the measured diode turn-off current

by Prony's method. These dominant modes represent the turn-off and depletion behavior and ringing, respectively. Therefore, the dynamic characteristics of diode turn-off current can be expressed as the reduced order with the dominant mode, which is obtained from Prony analysis.

Diode type dependence

The ringing frequency of the diode current at the turn-off shown in Fig.3.22(b) is extracted with Prony analysis as 86.2 MHz, 80.3 MHz, and 62.6 MHz for STTH8L06 (Si-PiND), RHRP860 (Si-PiND), and TRS8E65C (SiC-SBD), respectively. The damping factors of the ringing oscillation were also extracted as 1.46×10^8 /sec, 3.33×10^7 /sec, and 2.43×10^7 /sec for STTH8L06 (Si-PiND), RHRP860 (Si-PiND), and TRS8E65C (SiC-SBD), respectively. The damping factors of the ringing oscillation for Si-PiNDs are larger than for SiC-SBD. The differences correspond with product of those ESR and terminal capacitance in the diode blocking condition, as shown in Fig.3.4(b).

Prony analysis extracted the frequency of the modes that represent the ringing oscillation related with turn-off and depletion of each diode shown in Fig.3.22(a) to be 16.3 MHz, 31.5 MHz, and 57.2 MHz for STTH8L06 (Si-PiND), RHRP860 (Si-PiND), and TRS8E65C (SiC-SBD), respectively. Fig.3.22(c) shows the Fourier spectrum of the measured current for respective diode. Si-PiND has higher spectrum peak around 10 to 30 MHz than SiC-SBD stemming from longer recovery time.

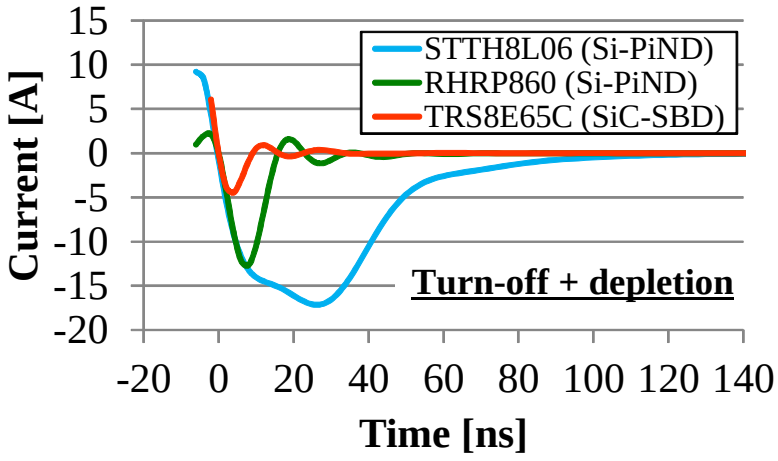

(a) Turn-off + depletion

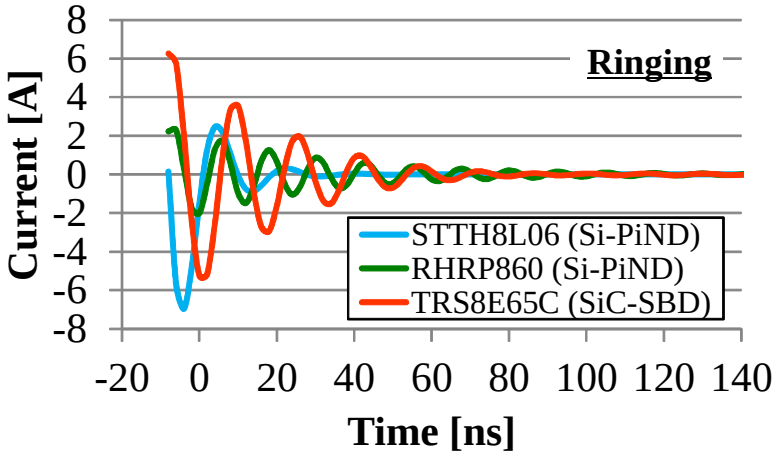

(b) Ringing

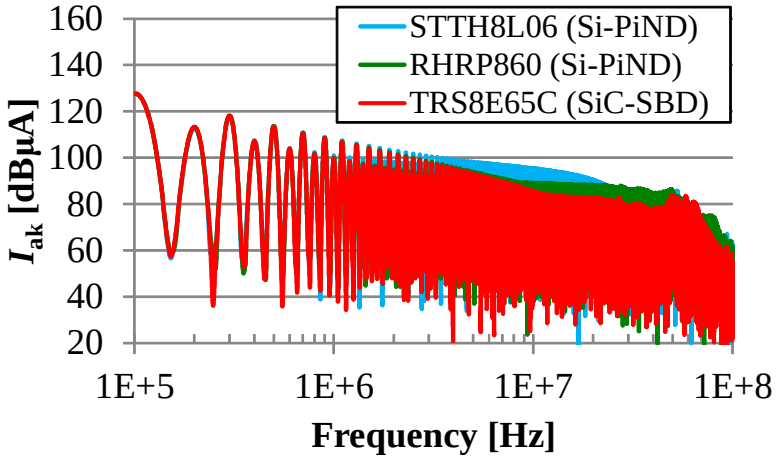

(c) Diode current Fourier spectrum

Figure 3.22: Characterization of transient response by Prony's method (diode type dependency)

Temperature dependence

The damping factor of the oscillation for the Si-PiND is calculated as 3.44×10^7 /sec, 5.00×10^7 /sec, and 9.61×10^7 /sec for 25°C, 100°C, and 175°C, respectively. The ESR of Si-PiND under 200 V reverse bias voltage at 175°C is more than twice that at 25°C. The differences in damping factor correspond with those in the ESR in the diode blocking condition, as shown in Fig.3.7(d). The difference in the settling time of the ringing oscillation can be attributed to the difference in the damping factor with the ESR of the diode in the blocking state.

Fig.3.23 and Fig.3.24 show the Fourier spectrum of the measured diode current to respective temperature. The peak value of the reverse recovery current for the Si-PiND increased with temperature, resulting in increments of an even-order harmonics level, as shown in Fig.3.23(a). Prony analysis extracted the frequencies of the modes that represent the ringing oscillation related with the turn-off and depletion of the Si-PiND to be 30.0 MHz, 26.6 MHz, and 15.9 MHz for 25°C, 100°C, and 175°C, respectively. The spectrum peak at 10 to 30 MHz shifted to lower frequency due to longer recovery time, as shown in Fig.3.24(a). The SiC-SBD showed invariant switching behavior to the operating temperature, and the even-order harmonics and the spectrum level at 10 to 30 MHz does not change, as shown in Fig.3.23(b) and Fig.3.24(b). No significant difference was observed in the spectrum peak level at 50 MHz among the diode type and temperature. This noise was caused by the ringing oscillation at the turn-on of the diode, as shown in Fig.3.20. The spectrum levels above 50 MHz decreased with increasing temperature for the Si-PiND, as shown in Fig.3.24(a). Using Prony analysis, the ringing oscillation frequency of the Si PiND current at the turn-off were extracted as 76.3 MHz, 72.7 MHz, and 75.2 MHz for 25°C, 100°C, and 175°C, respectively. The damping factor of the ringing oscillation increased with the temperature, as mentioned above; therefore, the noise spectrum levels above 50 MHz decreased with increasing temperature.

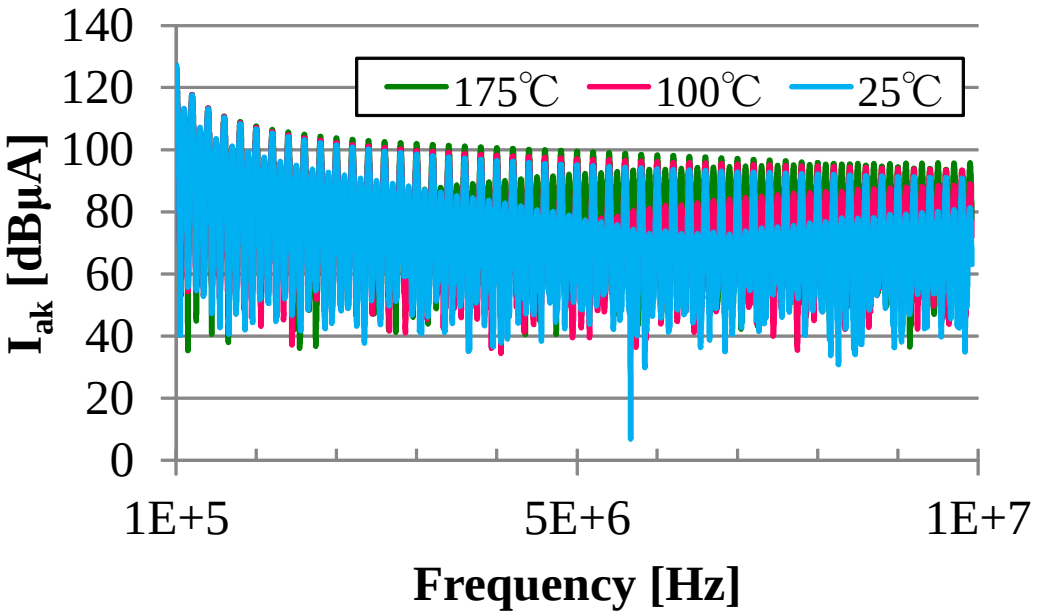

(a) Si-PiND current spectrum

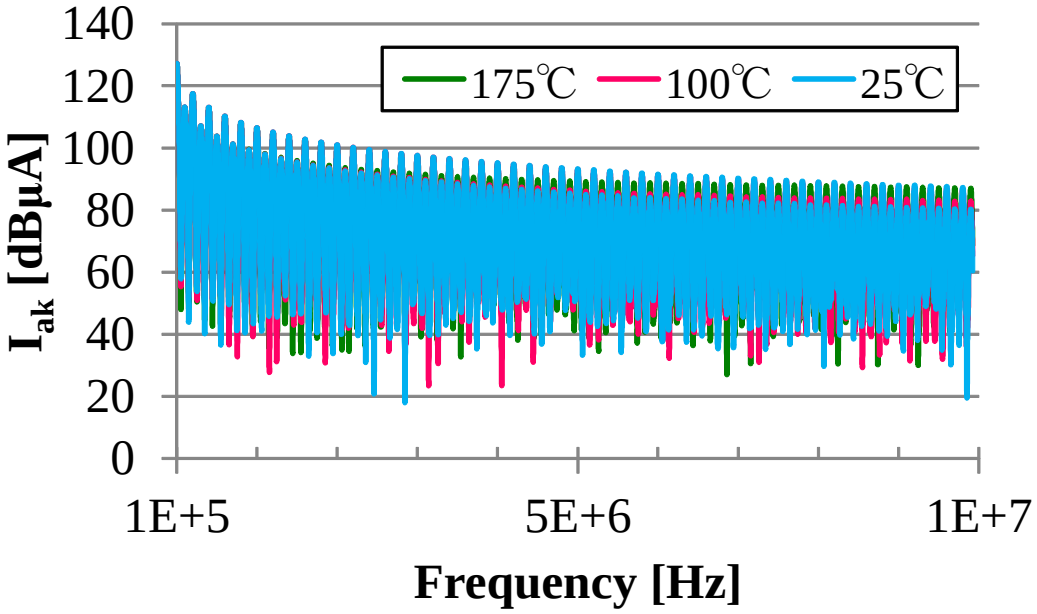

(b) SiC-SBD current spectrum

Figure 3.23: The frequency spectrum of diode current (temperature dependency, 0.1−10 MHz, frequency axis: linear)

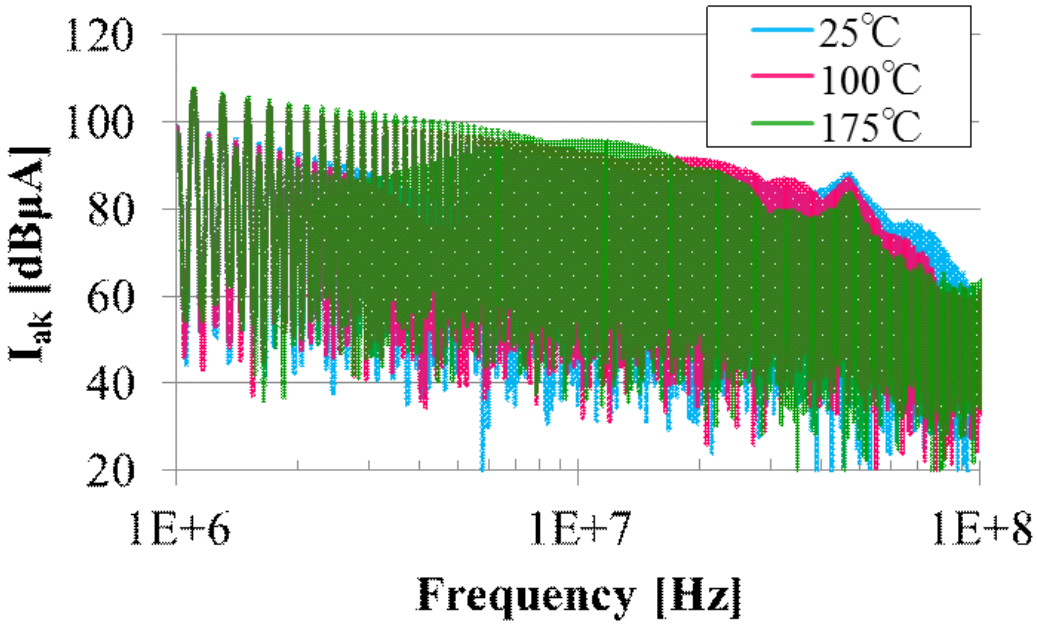

(a) Si-PiND current spectrum

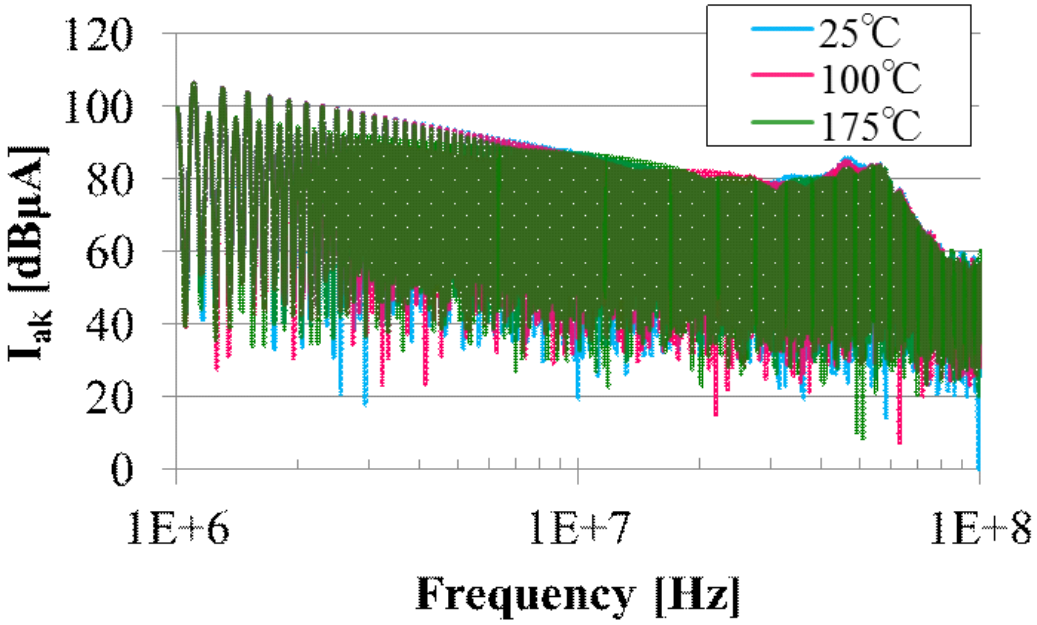

(b) SiC-SBD current spectrum

Figure 3.24: The frequency spectrum of diode current (temperature dependency, 1−100 MHz, frequency axis: log)

3.4 EMI noise emission measurement for CCM DC-DC boost converter

3.4.1 The difference in conducted emission with the operation and measurement condition

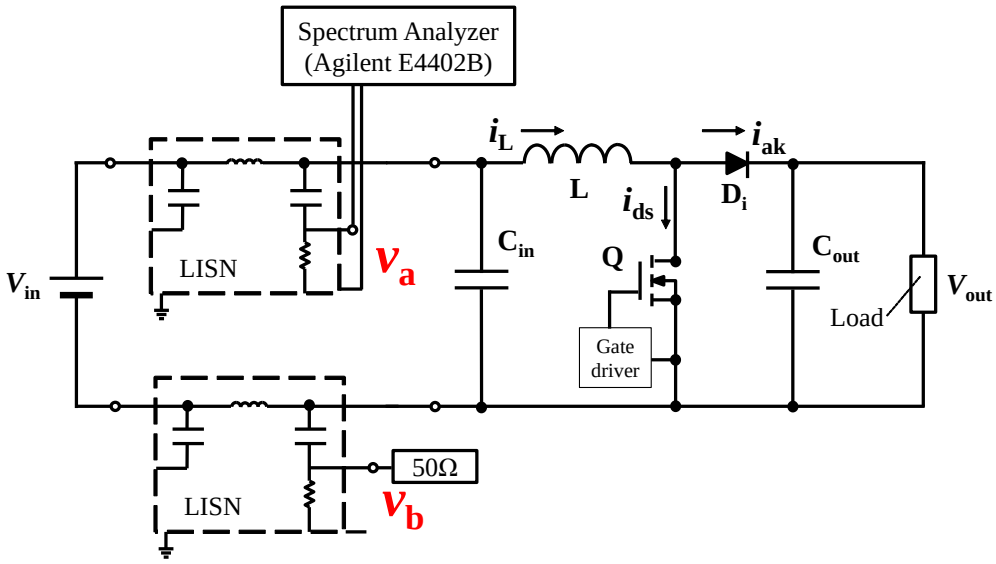

(a) using Super-heterodyne spectrum analyzer

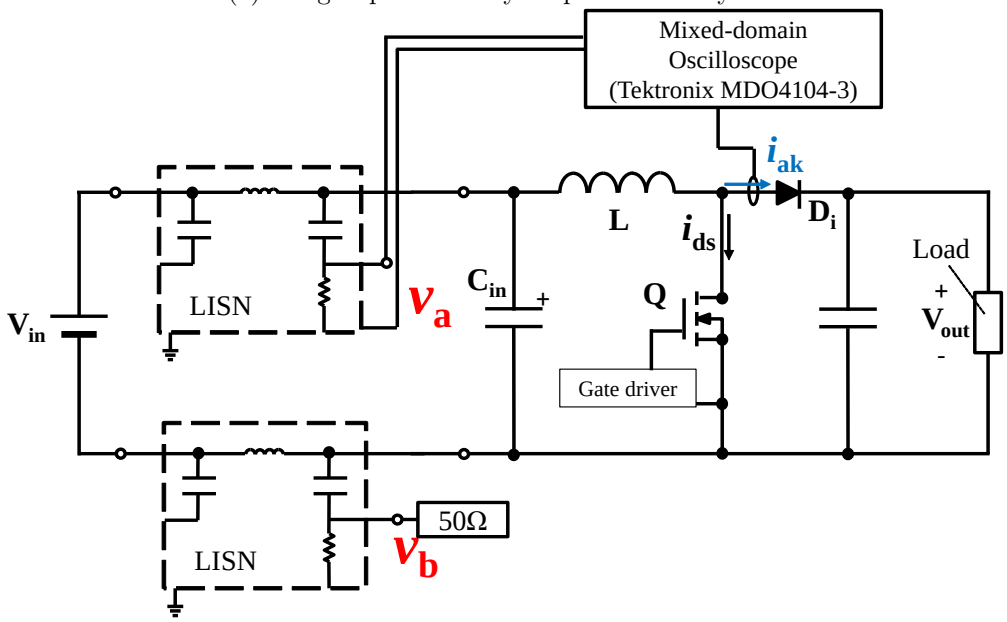

(b) using Real-time spectrum analyzer

Figure 3.25: Test circuit configuration for conducted emission measurement

This section presents the measured frequency spectrum of the conducted emission in the terminal disturbance voltage of the line to the ground v_a and v_b. A super-heterodyne spectrum analyzer (Agilent E4402B) with a peak-detection mode and line impedance stabilization network (LISN, 9117-5-PJ-50-N, Solar Electronics Co., Ltd., 0.15 MHz – 400 MHz) were used for the measurement, as shown in Fig.3.25(a). A mixed-domain oscilloscope (Tektronix MDO4104-3) and LISN are used for measurement as shown in Fig.3.25(b).

The difference in the measured spectrum with spectrum analyzer type

Figs.3.26–3.29 show the v_a and v_b in 100 kHz–30 MHz and 1 MHz–200 MHz frequency range, respectively. Two different type spectrum analyzers are used for measurement. The RBW of super-heterodyne spectrum analyzer was set to 9 kHz (measurement for 100 kHz–30 MHz) and 120 kHz (measurement for 1 MHz–200 MHz). The measured results suggest that the spectrum peak level of the conducted emission does not vary with type of spectrum analyzer, but the noise floor level is different. The IF filter in a super-heterodyne spectrum analyzer affects the noise floor level. The narrower the bandwidth of the filter realizes a lower noise floor. The RBW for a real-time spectrum analyzer is inversely proportional to the acquisition time [49]. More samples are required to achieve a smaller noise floor level. The difference of spectrum peak level between v_a and v_b results from unbalanced and asymmetrical circuit topology of a boost converter.

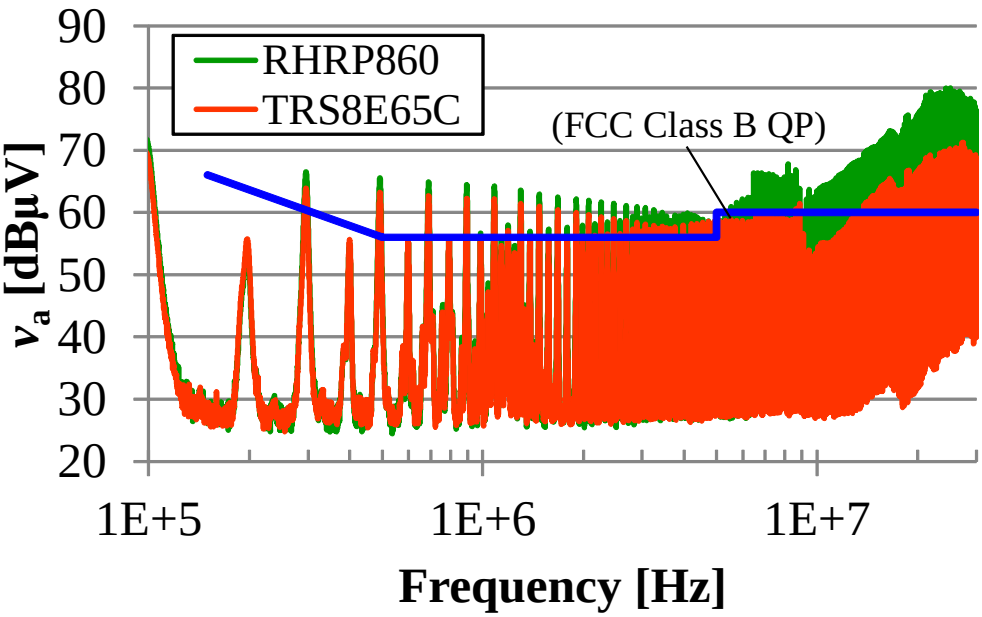

(a) v_a

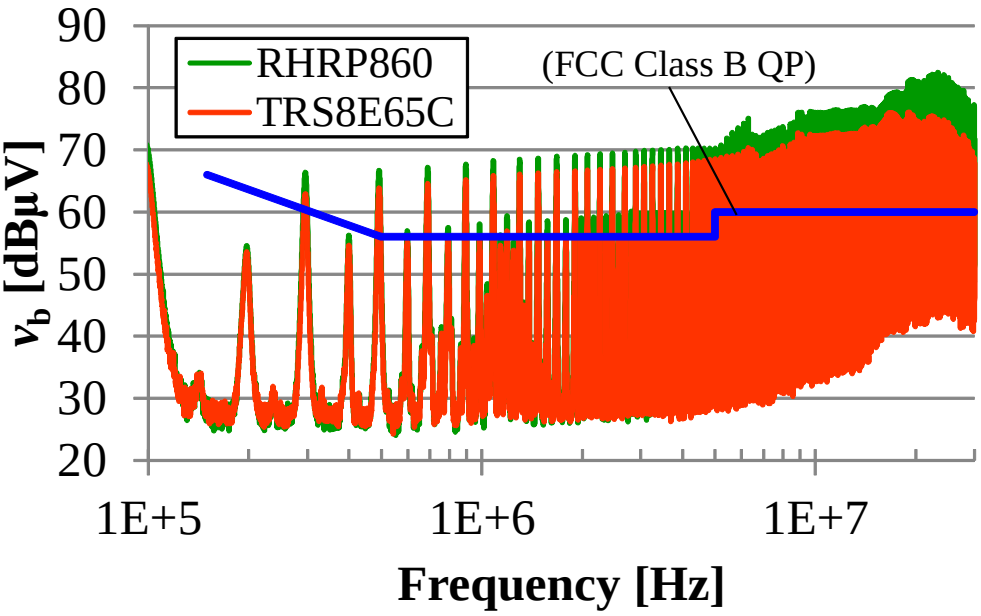

(b) v_b

Figure 3.26: The frequency spectrum of terminal disturbance voltage (100 kHz – 30 MHz, super-heterodyne spectrum analyzer)

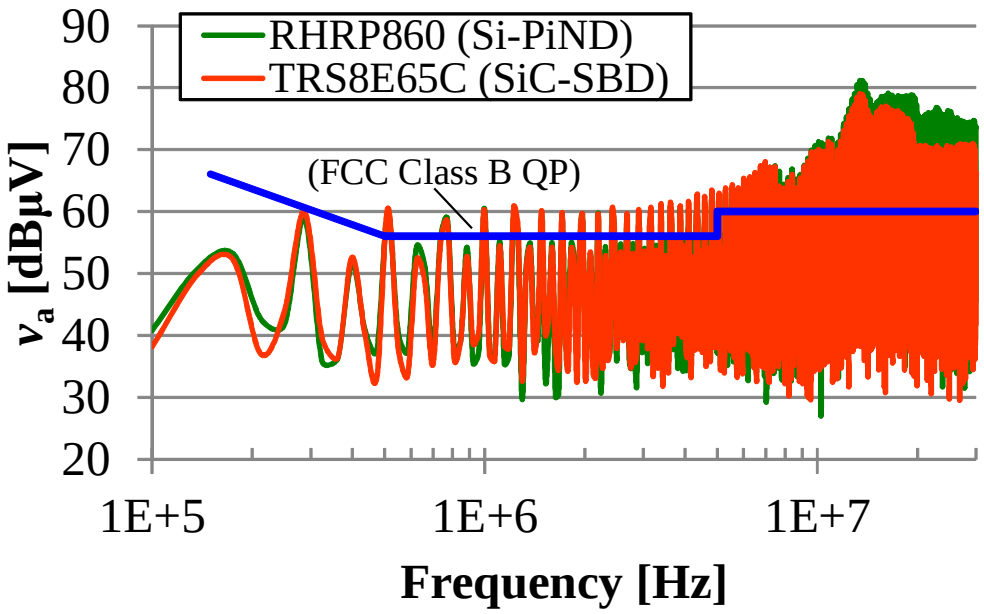

(c) v_a

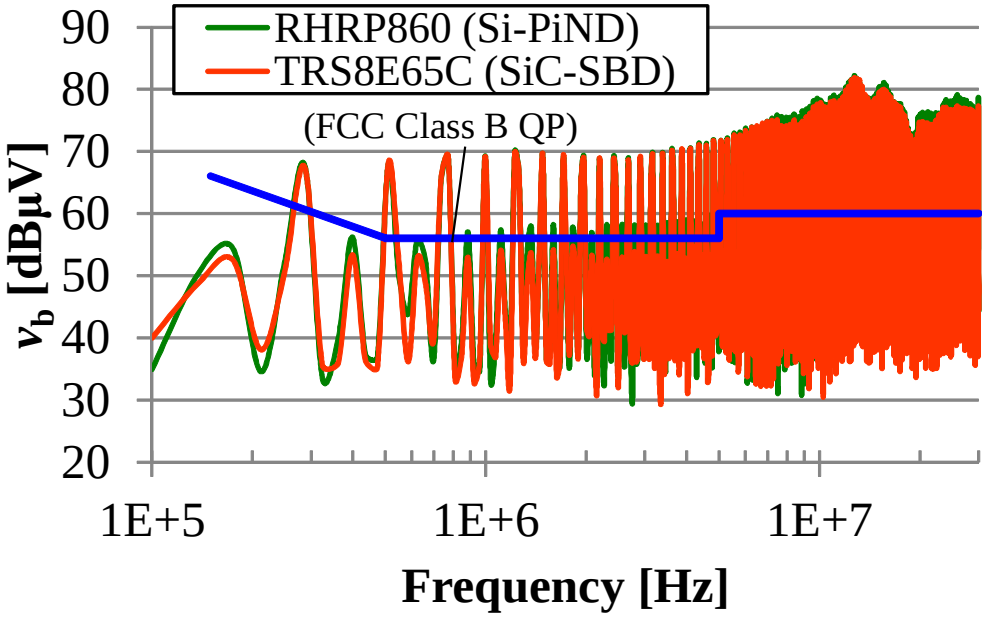

(d) v_b

Figure 3.27: The frequency spectrum of terminal disturbance voltage (100 kHz – 30 MHz, real-time spectrum analyzer)

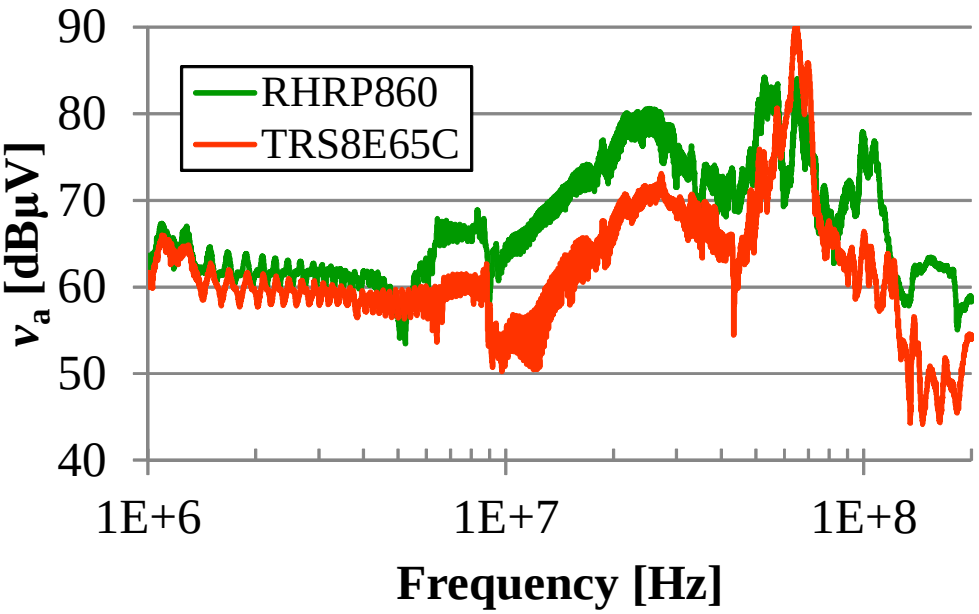

(a) v_a

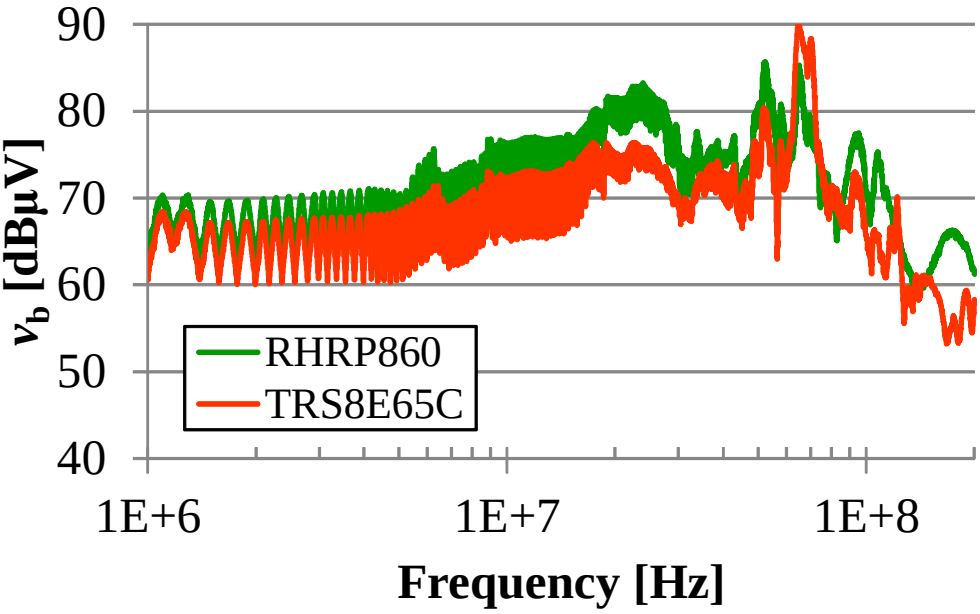

(b) v_b

Figure 3.28: The frequency spectrum of terminal disturbance voltage (1 MHz – 200 MHz, super-heterodyne spectrum analyzer)

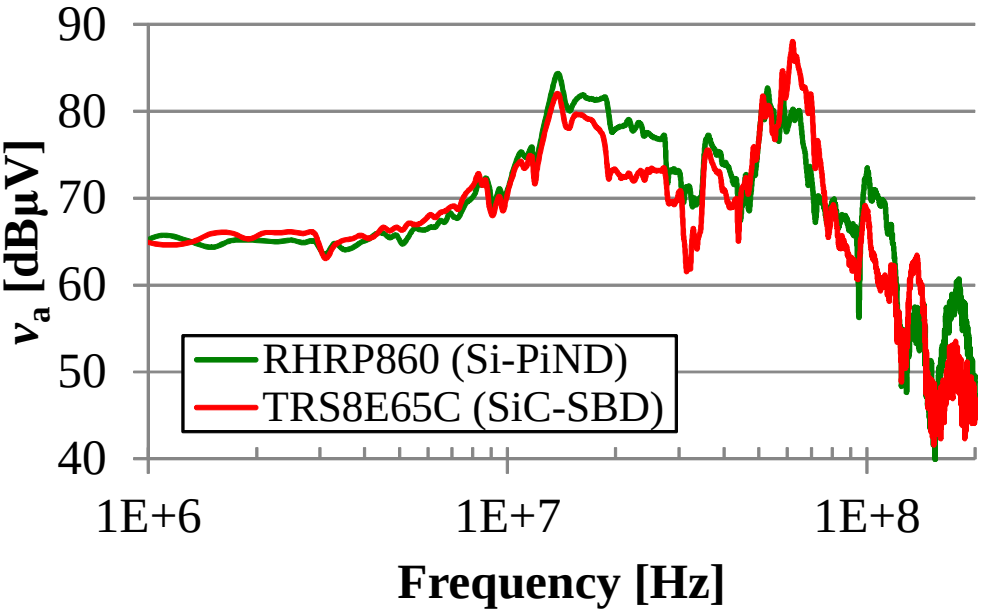

(c) v_a

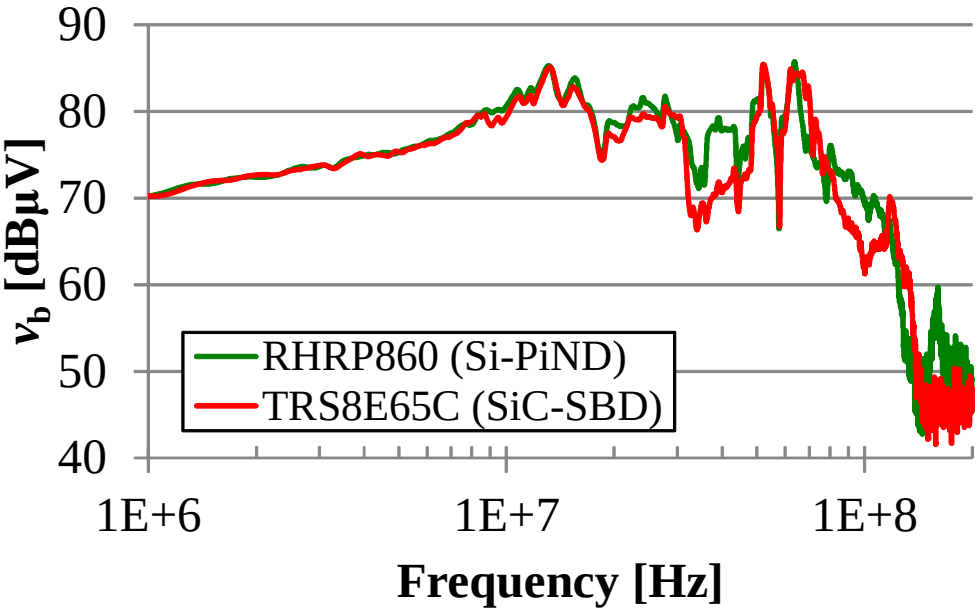

(d) v_b

Figure 3.29: The frequency spectrum of terminal disturbance voltage (1 MHz – 200 MHz, real-time spectrum analyzer)

Diode type dependency

Fig.3.30(a) shows the frequency spectrum of v_a at 100 kHz–30 MHz for the different type of diodes. The spectrum level above 10 MHz differs with the type of diode. STTH8L06 (Si-PiND) exhibits the highest spectrum levels at 10 MHz range corresponding to the longer recovery time and the frequency of the modes that represent the turn-off and depletion behavior extracted by Prony's method as shown in Fig.3.22(a). RHRP860 (Si-PiND) exhibits the highest spectrum levels for 20–30 MHz range. This result also corresponds to the frequency of contained in the turn-off and depletion behavior mode. TRS8E65C (SiC-SBD) exhibits the spectrum level approximately 5–10 dB lower than the Si-PiNDs.

Fig.3.30(b) also shows the frequency spectrum of v_a for 1–200 MHz for respective type of diodes. STTH8L06 (Si-PiND) exhibits the lowest spectrum peak level above 50 MHz which corresponds to the small $\frac{dI_R}{dt}$ and large damping factor of the ringing mode. RHRP860 (Si-PiND) gives the broad spectrum distribution from 50 MHz to 200 MHz range, which corresponds to the large $\frac{dI_R}{dt}$. TRS8E65C (SiC-SBD) exhibits notable spectrum peak at 60 MHz. This results from the small damping factor of the ringing mode. These results suggest that the ringing oscillation component in the diode switching current has significant influence on the noise level in high frequency range above conducted emission regulation.

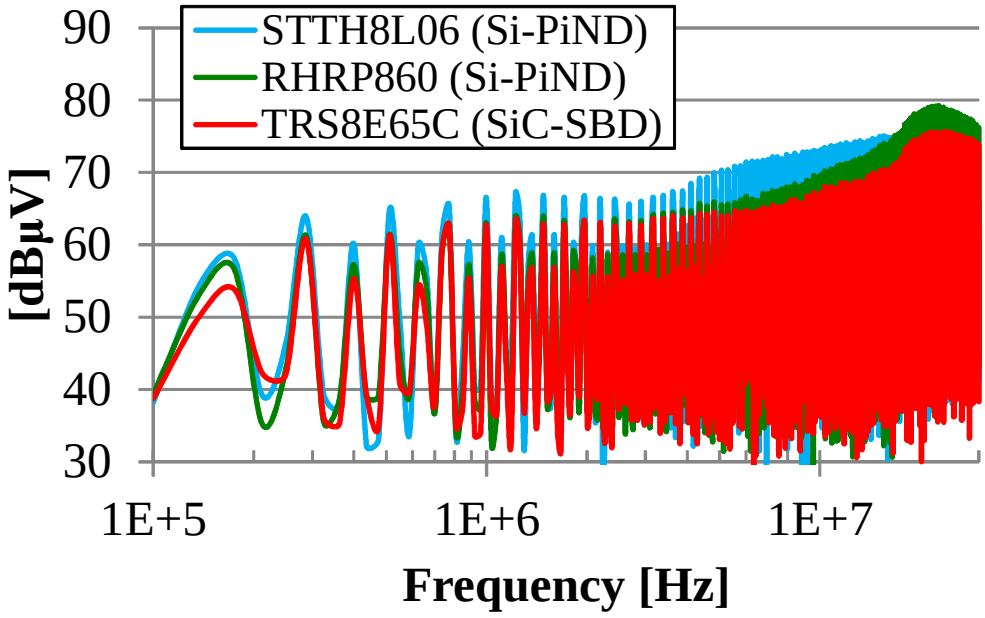

(a) 100 kHz – 30 MHz

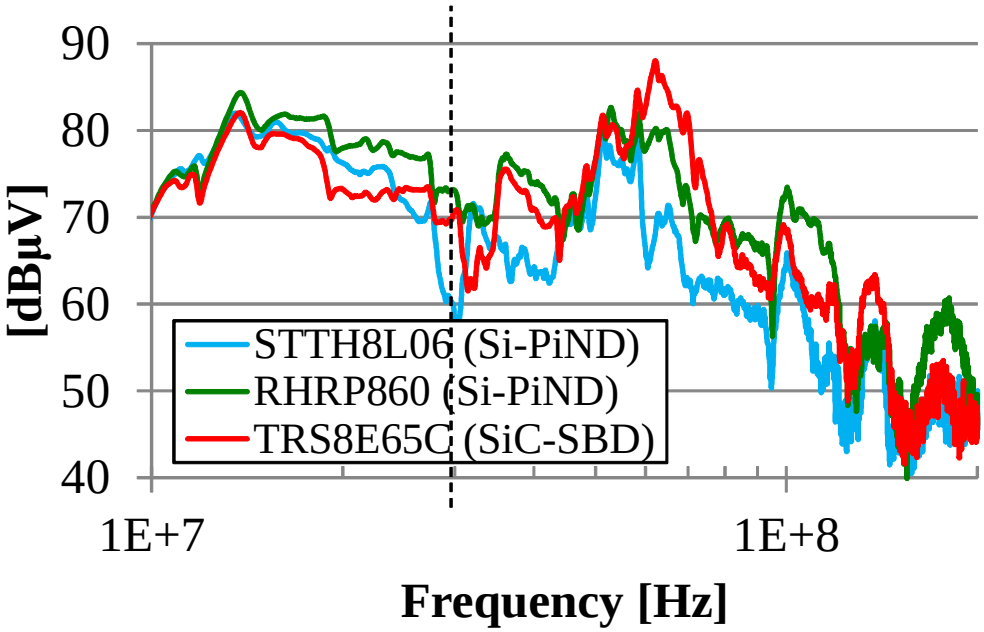

(b) 10 MHz – 200 MHz

Figure 3.30: The frequency spectrum of conducted emission (diode type dependency)

Temperature dependency

Figs.3.31 (a) and (b) show the frequency spectrum of v_a for 1−200 MHz respectively for the Si-PiND and SiC-SBD to the different diode temperature. The conducted noise spectrum level above several megahertz was affected by the temperature when the Si-PiND was used in the converter. The large reverse recovery peak and long reverse recovery time for 175°C gives larger current spectrum level for 3−20 MHz than room temperature as shown in Fig.3.23(a) and Fig.3.24(a). Thus, the conducted emission for 175°C gives the highest levels at this frequency range. The noise spectrum levels above 50 MHz decreased with increasing temperature, as shown in Fig.3.31(a). However, the influence of temperature was not significant for the SiC-SBD to the conducted emission noise level in the entire intended frequency range, as shown in Fig.3.31(b). The fast damping of the ringing oscillation in the Si-PiND turn-off operation at high temperature gave less noise in the frequency range of >50 MHz.

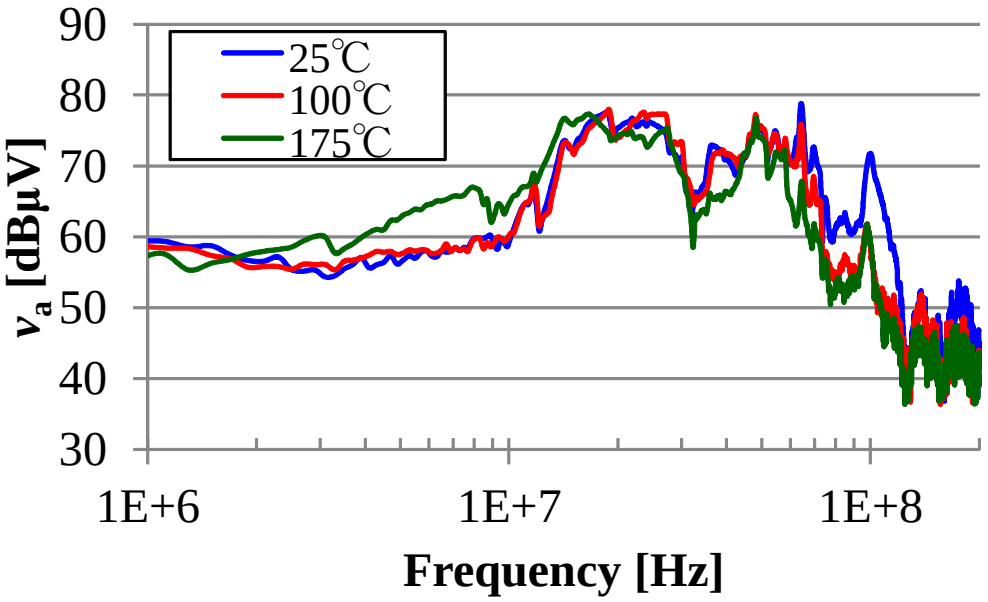

(a) Si-PiND

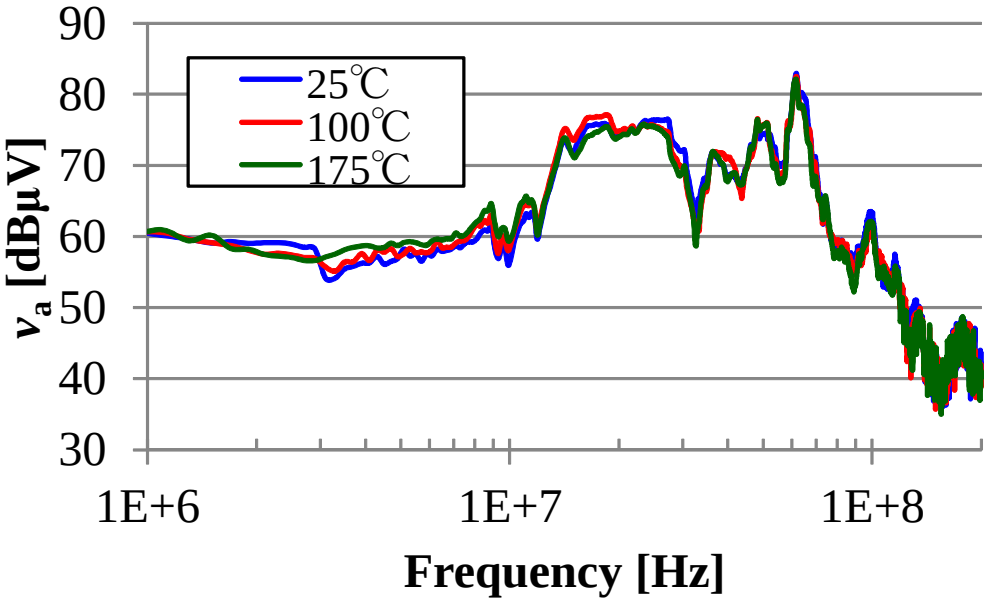

(b) SiC-SBD

Figure 3.31: The frequency spectrum of conducted emission (temperature dependency)

3.4.2 Spectrogram of conducted emission

Diode type dependency

Fig.3.32 is the spectrogram of the conducted emission in one switching period. The horizontal linear axis is frequency, and the vertical axis is time, and the noise emission levels are color-corded. The conducted noise is measured for the switching operation. The emission level and spectrum distribution for the diode turn-on operation are almost unaffected by the type of diode. STTH8L06 (Si-PiND) exhibits the highest spectrum levels around 10 MHz and the lowest spectrum levels above 50 MHz for diode turn-off operation as shown in Fig.3.32(a). RHRP860 (Si-PiND) exhibits the highest spectrum levels for 20–30 MHz. RHRP860 also shows the broad spectrum distribution from 50 MHz to 200 MHz range at the diode turn-off in Fig.3.32(b). TRS8E65C (SiC-SBD) gives larger spectrum level around 60 MHz than for Si-PiNDs as shown in Fig.3.32(c). These results correspond to the damping factor and oscillation frequency of the diode turn-off current extracted by Prony's method.

Temperature dependency

Fig.3.33 shows the measured spectrogram of the conducted emission in one switching period for different Si-PiND and SiC-SBD temperature. The influence of the temperature on the noise level and distribution was not significant for the SiC-SBD, as shown in Fig.3.33(b). Prony analysis extracted the ringing oscillation frequency related with turn-off and depletion for Si-PiND to be 30.0 MHz, 26.6 MHz, and 15.9 MHz respectively for 25°C, 100°C, and 175°C, as mentioned above. Fig.3.33(a) shows the effect of temperature to frequency shift of the conducted emission. Fig.3.33(a) also shows that the noise spectrum levels above 50 MHz decreased with temperature rise.

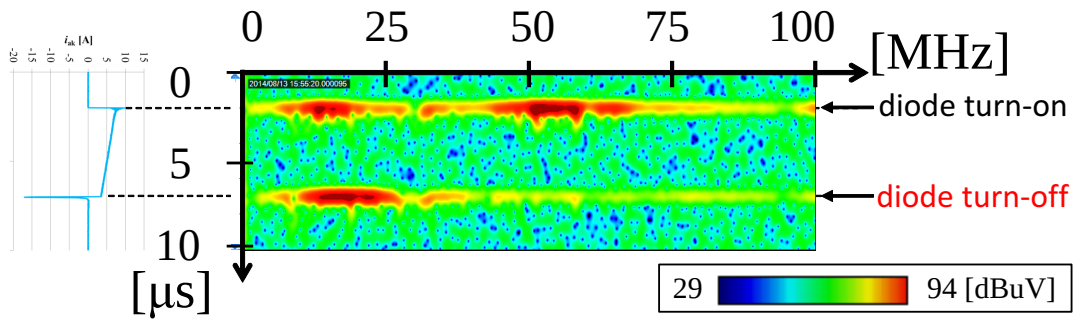

(a) STTH8L06 (Si-PiND)

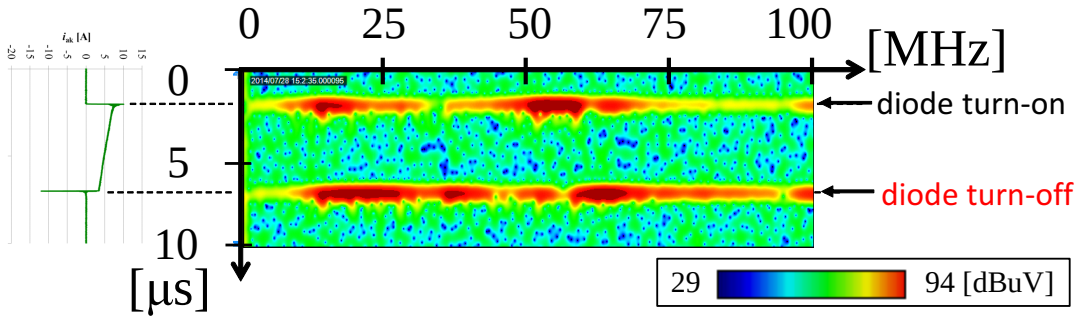

(b) RHRP860 (Si-PiND)

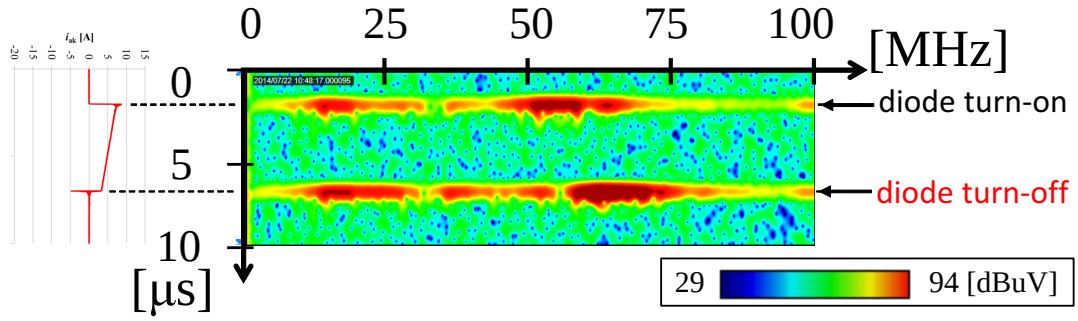

(c) TRS8E65C (SiC-SBD)

Figure 3.32: Measured spectrogram of terminal disturbance voltage v_a (One switching cycle, 25°C)

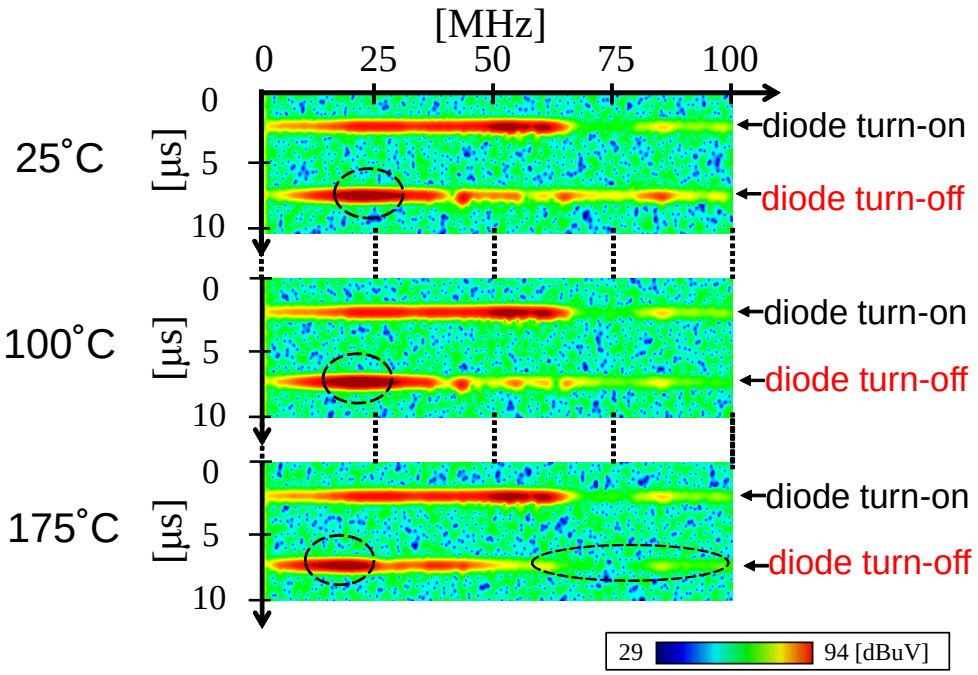

(a) RHRP860 (Si-PiND)

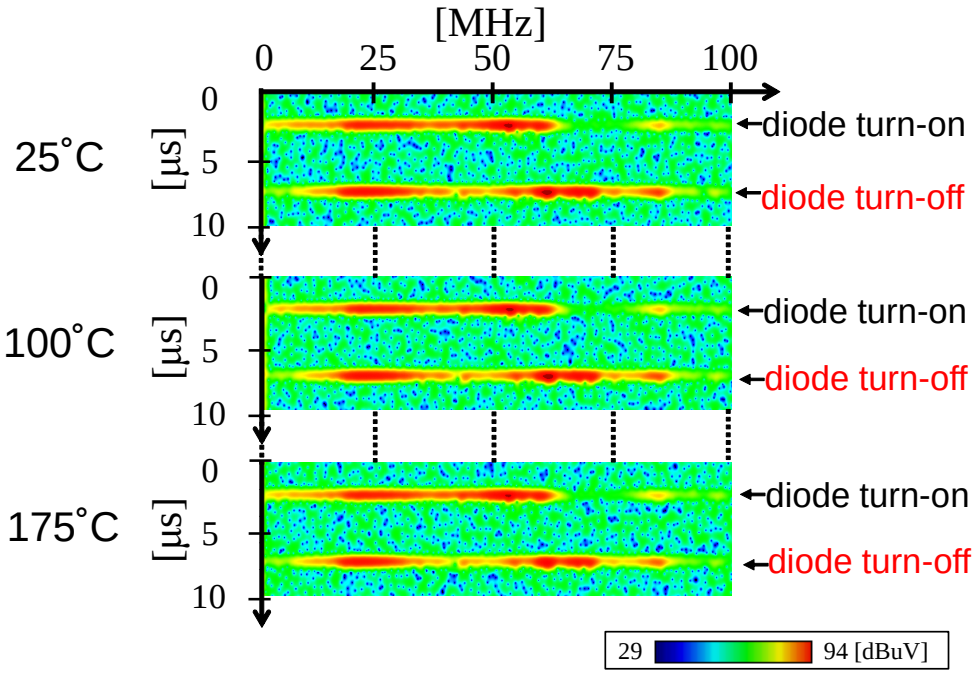

(b) TRS8E65C (SiC-SBD)

Figure 3.33: Measured spectrogram of terminal disturbance voltage v_a (temperature dependency)

3.5 Summary

This chapter evaluated the diode type and its operating temperature dependency on the reverse recovery behavior, and assessed the conducted emission in the CCM DC−DC boost converter. The Si-PiND exhibited large peak reverse current and long recovery time at high temperature, leading to an increased emission level in the conducted noise frequency range. However, the damping of the ringing oscillation in the Si-PiND switching current is increased at a high temperature, resulting in the suppressed noise level, particularly for frequencies >50 MHz. In contrast, the SiC-SBD showed invariant switching behavior and conducted emission level to the operating temperature. Therefore, the SiC-SBD enables easier design and evaluation of the noise level of the application circuit than the Si-PiND for different operating condition.

This chapter evaluated the conducted noise based on time and frequency mixed domain analysis. Prony's method could evaluate the dynamic characteristics of diode turn-off current. The extracted damping factor and ringing oscillation frequency were in good agreement with the conducted noise spectrum level and distributions. The measurement of the spectrogram by using real-time spectrum analyzer enables the detection of transient events. The spectrogram gave valuable information on characterizing the noise source and the conducted noise emission.

Chapter 4

Time variation of EMI noise emission for PFC converter

4.1 Introduction

Active power-factor correction (PFC) converters have been widely used in AC-DC power conversion circuits to achieve high power factor and low harmonic distortion [60]. The PFC controller modulates the duty ratio of MOSFETs to shape the input AC current to a sinusoid and to displace the current in phase with the supply voltage, while regulating the output DC voltage as constant. Three type of operating modes are available for a PFC converter. They are the continuous current mode (CCM), discontinuous current mode (DCM), and critical current mode (CRM) [61]. The CCM PFC converter has the advantage that its input ripple current is lower than that of CRM and DCM circuits. It contributes to lower current stress of MOSFETs and conduction losses of the circuit; therefore, the CCM PFC converter is especially suitable for high-power applications [62]. However, the reverse recovery current of a conventional Silicon (Si)-PiN diode (PiND) is induced during the turn-off operation, which is initiated by current commutation from diode to MOSFET due to the turn-on operation of the MOSFET, resulting in not only a large switching loss but also a switching noise in the CCM PFC converter [55], [56]. This section focuses on the turn-off of diode in a CCM PFC

converter. The total power conversion losses and conducted EMI noise frequency spectrum of a 300-W PFC converter were experimentally investigated and compared for Si-PiND, Si-SBD, and SiC-SBD.

4.2 PFC converter: principle and purpose

4.2.1 Rectifying harmonics limits

Fig.4.1 (a) shows a typical single-phase capacitor input diode-bridge rectifier. Diodes D_1 and D_3 operate complimentary with diodes D_2 and D_4. D_1 and D_3 conduct for a short interval in a line cycle for $v_{in} > V_{out}$. Similarly, D_2 and D_4 also conduct for a short interval in a line cycle when $-v_{in} > V_{out}$. A large smoothing capacitor is connected at the rectifier output to reduce the ripple in the DC output voltage. However, the input current drawn by this converter is peaky stemming from large smoothing capacitor as shown in Fig.4.1 (b) and rich in low-order odd harmonics component (I_3, I_5, etc.). Therefore it leads to high total harmonic distortion (THD) and poor input power factor (PF) [4].

Many countries have developed their own National Electromagnetic Compatibility standards for limiting the harmonic content in the current drawn by different equipment. The IEC 61000-3-2 international standard sets limits on the maximum level of harmonics [38]. Other standards of conducted noise are those of FCC (Federal Communications Commission , USA), CISPR (International Special Committee on Radio Interference, France), VDE (Verband Deutscher Electrotechnischer, Germany), and MIL (Military Standard). Products used in a country have to comply with the standards of that country. For example, Table 4.1 shows the IEC standards IEC 61000-3-2 Limits of harmonic current emissions for equipment with input current less than 16 A [4].

The power factor is defined as [11]

$$\begin{aligned} PF &= \frac{P}{|S|} = \frac{\text{Real power}}{\text{Apparent power}} = \frac{\text{Average power}}{(\text{RMS current})(\text{RMS voltage})} \\ &= \frac{\sum_{n=1}^{\infty} P_n}{I_{\text{rms}} V_{\text{rms}}} = \frac{\sum_{n=1}^{\infty} I_{\text{rms}(n)} V_{\text{rms}(n)} \cos\phi_n}{\sqrt{\sum_{n=1}^{\infty} I_{\text{rms}(n)}^2 \sum_{n=1}^{\infty} V_{\text{rms}(n)}^2}}, \end{aligned} \tag{4.1}$$

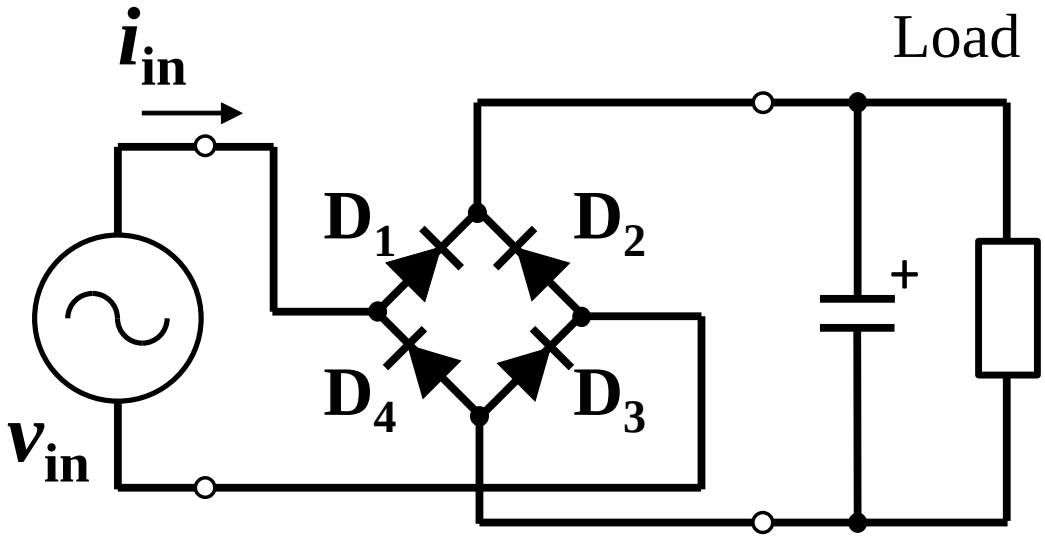

(a) Simple rectifier

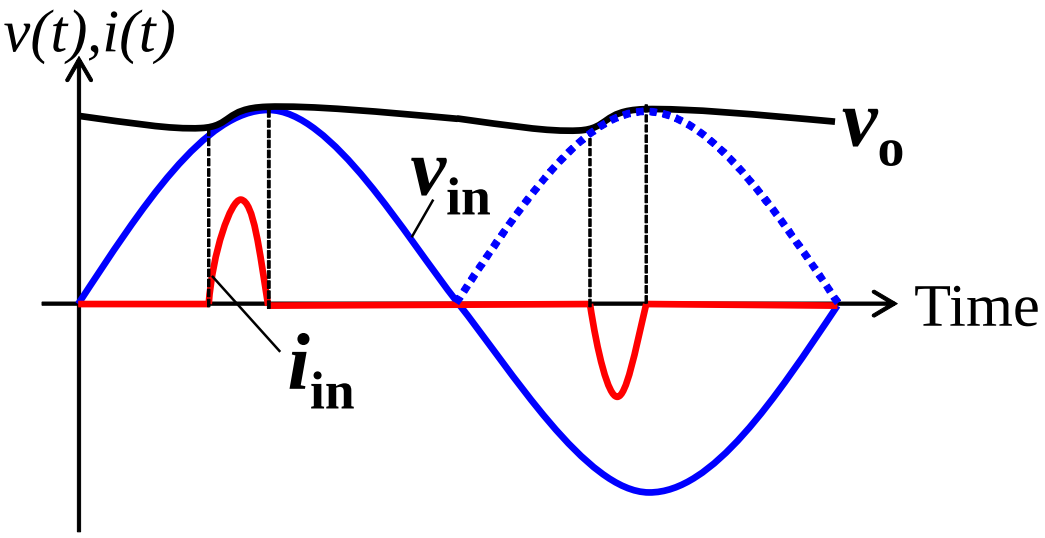

(b) voltage and current waveform

Figure 4.1: Diode bridge rectifier circuit diagram and voltage and current waveform

where the real power, called the average power or the time average power, is given by

$$P = \frac{1}{2\pi}\int_0^{2\pi} p\mathrm{d}(\omega t) = \frac{1}{2\pi}\int_0^{2\pi} vi\mathrm{d}(\omega t) \tag{4.2}$$

and the apparent power is

$$|S| = \sqrt{\frac{1}{2\pi}\int_0^{2\pi} v^2\mathrm{d}(\omega t)}\sqrt{\frac{1}{2\pi}\int_0^{2\pi} i^2\mathrm{d}(\omega t)} = V_{\mathrm{rms}}I_{\mathrm{rms}}. \tag{4.3}$$

Here, $p = vi$ is the instantaneous power, and $S = VI^*$ is the complex power.

Table 4.1: Limits for class A appliances

Harmonic order	Maximum authorized harmonic current [A]
Odd harmonics	
3	2.30
5	1.14
7	0.77
9	0.40
11	0.33
13	0.21
$15 \leq n \leq 39$	$0.15 \times 15/n$
Even harmonics	
2	1.08
4	0.43
6	0.30
$8 \leq n \leq 40$	$0.23 \times 8/n$

Let us assume that the utility line voltage is purely sinusoidal,

$$v_s = \sqrt{2} V_{\text{rms1}} \sin \omega t. \tag{4.4}$$

In general, the utility line current is not sinusoidal and can be represented by a Fourier series,

$$i_s = \sqrt{2} I_{\text{rms1}} \sin(\omega t + \phi_1) + \sqrt{2} I_{\text{rms2}} \sin(2\omega t + \phi_2) + \sqrt{2} I_{\text{rms3}} \sin(3\omega t + \phi_3) + \cdots . \tag{4.5}$$

The rms value of the line ac current is

$$I_{\text{rms}} = \sqrt{I_{\text{rms1}}^2 + I_{\text{rms2}}^2 + I_{\text{rms3}}^2 + \cdots}. \tag{4.6}$$

The total harmonic distortion is defined by

$$THD = \frac{\sqrt{I_{\text{rms2}}^2 + I_{\text{rms3}}^2 + I_{\text{rms4}}^2 + \cdots}}{I_{\text{rms1}}}. \tag{4.7}$$

The power factor for a sinusoidal voltage and a non-sinusoidal current is defined as

$$PF = \frac{P}{V_{\rm rms} I_{\rm rms}} = \frac{V_{\rm rms1} I_{\rm rms1} \cos\phi_1}{V_{\rm rms1} I_{\rm rms}} = \frac{I_{\rm rms1}}{I_{\rm rms}} \cos\phi_1$$
$$= \frac{I_{\rm rms1}}{\sqrt{I_{\rm rms2}^2 + I_{\rm rms3}^2 + I_{\rm rms4}^2 + \cdots}} \cos\phi_1 = \frac{1}{\sqrt{1 + THD^2}} \cos\phi_1 = F_{DF} F_{DA}, \tag{4.8}$$

where the distortion factor or the current distortion factor is

$$F_{DF} = \frac{I_{\rm rms1}}{I_{\rm rms1}} = \frac{1}{\sqrt{1 + THD^2}}, \tag{4.9}$$

and the displacement angle or the displacement factor is

$$F_{DA} = \cos\phi_1. \tag{4.10}$$

The distortion factor F_{DF} as a function of THD is shown in Figure 3.38. The power factor for $\phi_1 = 0$ becomes

$$PF = \frac{I_{\rm rms1}}{I_{\rm rms}} = \frac{I_{\rm rms1}}{\sqrt{I_{\rm rms2}^2 + I_{\rm rms3}^2 + I_{\rm rms4}^2 + \cdots}} = \frac{1}{\sqrt{1 + THD^2}}. \tag{4.11}$$

PF ranges from 0 to 1. When the rms values of current harmonics are zero, $THD = 0$ and $PF = 1$ (at $\cos\phi_1 = 1$). The total harmonic distortion THD in terms of the power factor PF is

$$THD = \sqrt{\frac{1}{PF^2} - 1}. \tag{4.12}$$

The rms value of input current of an AC–DC power converter with output power P_O and efficiency η is

$$I_{\rm rms} = \frac{P_O}{V_{\rm rms} \eta PF}. \tag{4.13}$$

(4.8) shows that THD is closely related to PF. Then power factor correction (PFC) is widely used to achieve unity power factor and low input current distortion for rectifier circuit.

4.2.2 Effect of PFC converter on rectifying harmonics reduction

Fig.4.2 (a) shows the circuit diagram of a boost PFC converter, where Q is the MOSFET, D_i is the diode, L is the boost inductor, and C_o is the output filter

capacitor. The PFC controller modulates the duty ratio D of MOSFET to shape the input AC current to a sinusoid in phase with supply voltage, and to regulate for constant output DC voltage. The type of PFC converter can be categorized into three with the mode of inductor current conduction; continuous current mode (CCM), discontinuous current mode (DCM), and critical current mode (CRM). This section explains the CCM PFC converter operation.

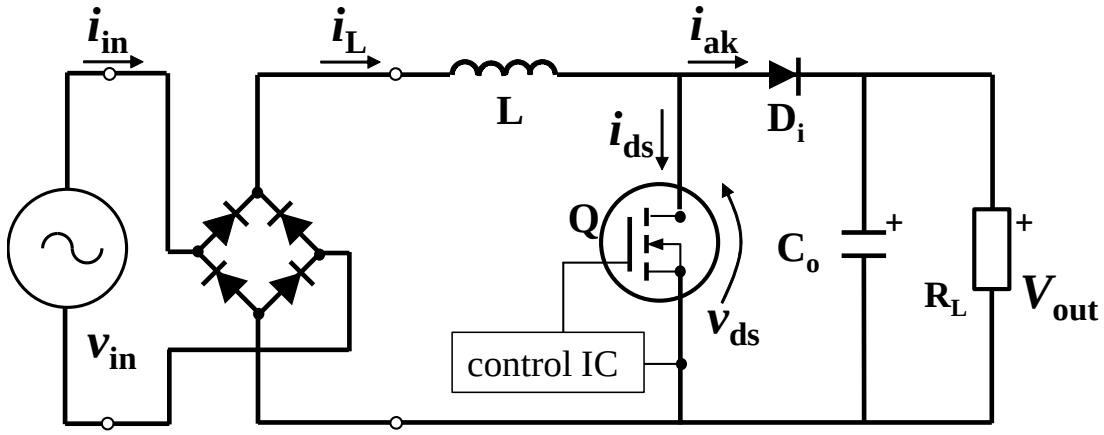

(a) Basic PFC converter

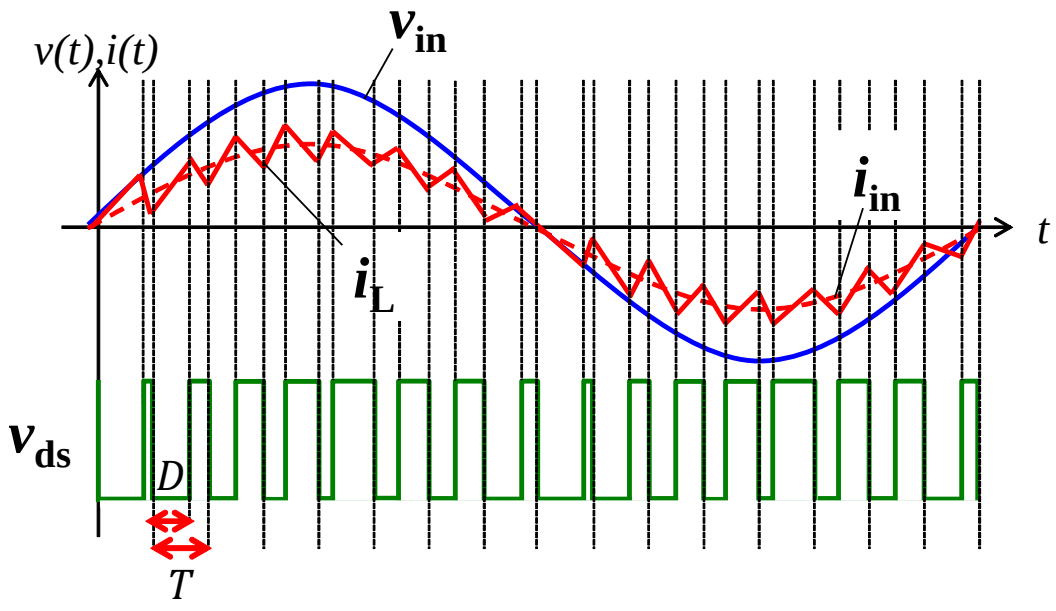

(b) voltage and current waveform (CCM)

Figure 4.2: PFC converter circuit diagram and voltage and current waveform

In order to describe the operation of the system in Fig.4.2(a), the inductor

current i_L and output voltage v_{out} are chosen as the state variables. The state equation is expressed as follows. Based on the state space averaging method with the average in one switching cycle of i_L and v_{out} as $\hat{i_L}$ and $\hat{v_{out}}$.

$$\begin{bmatrix} \frac{d\hat{i_L}}{dt} \\ \frac{d\hat{v_{out}}}{dt} \end{bmatrix} = \begin{bmatrix} 0 & -\frac{1-D}{L} \\ \frac{1-D}{C_o} & -\frac{1}{R_L C_o} \end{bmatrix} + \begin{bmatrix} \frac{1}{L} \\ 0 \end{bmatrix} v_{in} \tag{4.14}$$

The solution of (4.14) for periodic steady state is obtained as

$$\begin{bmatrix} \hat{i_L} \\ \hat{v_{out}} \end{bmatrix} = \begin{bmatrix} \frac{1}{R_L(1-D)^2} \\ \frac{1}{1-D} \end{bmatrix} v_{in} = \begin{bmatrix} -\frac{\hat{v_{out}}}{R_L(1-D)} \\ \frac{v_{in}}{1-D} \end{bmatrix}. \tag{4.15}$$

Instantaneous input voltage $v_{in}(t)$, input current $i_{in}(t)$, and input power $P_{in}(t)$ are respectively expressed with the average input power P_{in}, the RMS input voltage $v_{in-\mathrm{rms}}$, and power factor PF.

$$v_{in}(t) = \sqrt{2} v_{in-\mathrm{rms}} \sin \omega t \tag{4.16}$$

$$i_{in}(t) = \sqrt{2} \frac{\hat{P_{in}}}{v_{in-\mathrm{rms}}} \sin \omega t \tag{4.17}$$

$$P_{in}(t) = \hat{P_{in}}(PF - \cos 2\omega t), \tag{4.18}$$

where ω is the input AC angular frequency. Duty ratio $D(t)$ to compensate PF is obtained from (4.15).

$$D(t) = \frac{v_{out} - |v_{in}(t)|}{v_{out}} = 1 - \sqrt{2} \frac{v_{in-\mathrm{rms}}}{v_{out}} |\sin \omega t| \tag{4.19}$$

The ripple current of inductor $\Delta i_L(t)$, the RMS current of inductor $i_{L-\mathrm{rms}}$ and MOSFET $i_{Q-\mathrm{rms}}$ are expressed as follows, respectively.

$$\Delta i_L(t) = \frac{\hat{v_{out}} - v_{in}(t)}{L} D(t) T \tag{4.20}$$

$$i_{L-\mathrm{rms}} = \sqrt{i_{in}(t)^2 + \frac{\Delta i_L(t)^2}{12}} \tag{4.21}$$

$$i_{Q-\mathrm{rms}} = \sqrt{D\left(i_{in}(t)^2 + \frac{\Delta i_L(t)^2}{12}\right)} \tag{4.22}$$

The RMS current of inductor for AC frequency $i_{L-\mathrm{rms\text{-}AC}}$ can be denoted as

$$i_{L-\mathrm{rms\text{-}AC}} = \sqrt{\frac{1}{N} \sum_{n=1}^{N} (i_{L-\mathrm{rms}-n})^2}, \tag{4.23}$$

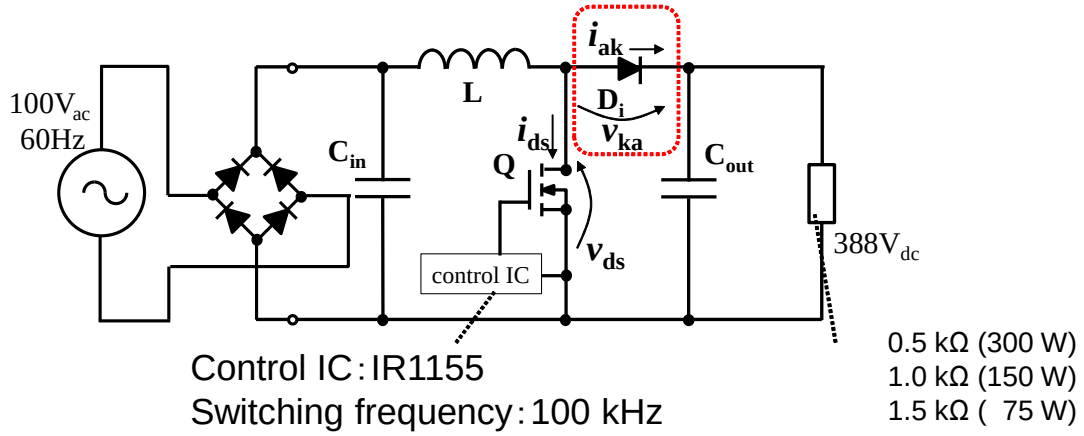

(a) Experimental circuit configuration

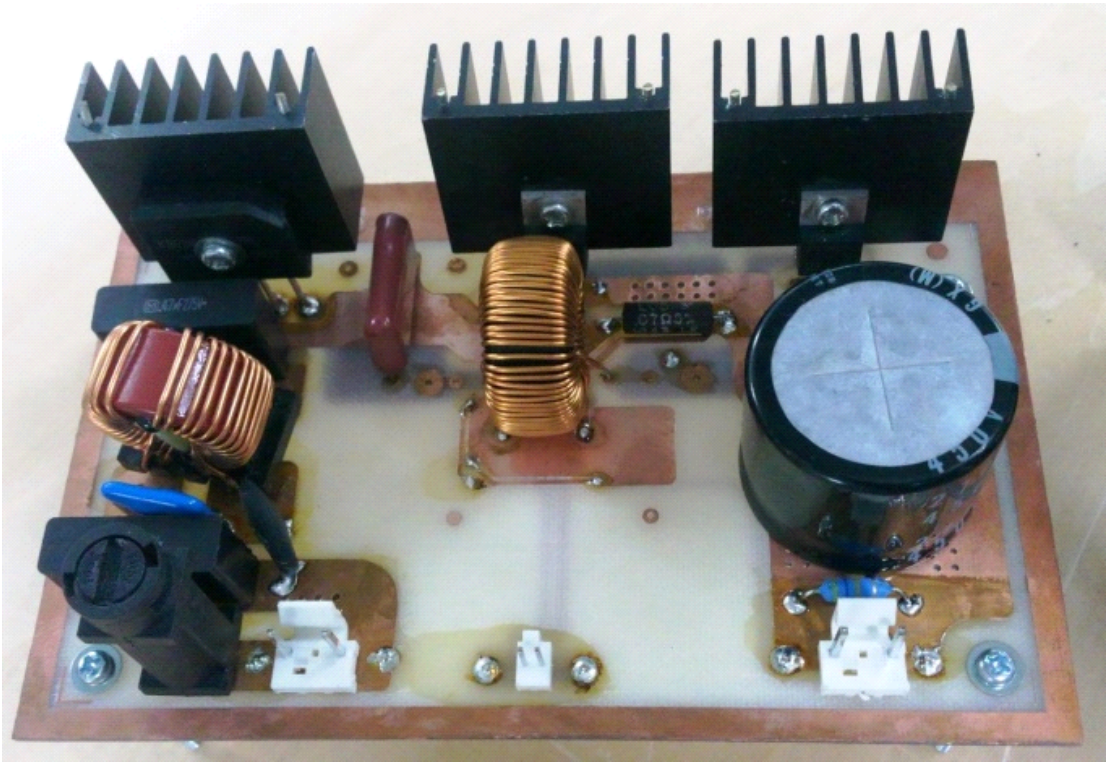

(b) Studied CCM PFC converter

Figure 4.3: Experimental PFC converter configuration

where $N = \frac{f_{sw}}{f_{AC}}$, f_{sw} is the switching frequency and $f_{AC} = \frac{\omega}{2\pi}$ is the input AC frequency.

The ripple current of inductor in CCM is lower than in DCM and CRM, and results in lower distortion of input current [61]. The duty ratio D is regulated in accordance with input voltage level as (4.19). However, the reverse recovery cur-

rent of diode D_i is induced for the diode turn-off and MOSFET turn-on transition. It causes not only switching losses but also switching noise in PFC converter.

Fig.4.3(a) shows the base configuration of the experimental circuit. The studied boost PFC converter shown in Fig.4.3(b) uses a CCM control IC (International Rectifier, IRAC1155). The switching frequency of the MOSFET (Infineon, IPP60R165CP) is 100 kHz (constant), the input AC voltage is 100 V_{RMS}, and the output DC voltage is 388 V.

Fig.4.4 shows the input voltage and current waveforms of PFC converter with 75 W, 150 W, and 300 W load power. The circuit is operated as a capacitor-input type diode-bridge rectifier and flows distorted current, when the PFC control IC is suspended (Fig.4.4(a)). The input current is shaped to be a sinusoidal as shown in Fig.4.4(b) when the PFC control IC is operated.

Fig.4.5 shows the amplitude of the odd-order harmonics of the measured input current shown in Fig.4.4, which is calculated by discrete Fourier transform (DFT). The power factor PF, crest factor I_{CF}, and total harmonic distortion I_{THD} in each case are calculated and shown in Table.4.2. The harmonics component in the input current is reduced with the PFC operation, and PF, THD are also improved.

Table 4.2: Calculated power factor, crest factor, and THD

(a) Capacitor input operation

Load	PF	I_{CF}	I_{THD}
75 W	0.581	3.044	1.379
150 W	0.608	2.913	1.259
300 W	0.667	2.492	1.067

(b) PFC operation

Load	PF	I_{CF}	I_{THD}
75 W	0.993	1.450	0.101
150 W	0.995	1.556	0.075
300 W	0.998	1.471	0.033

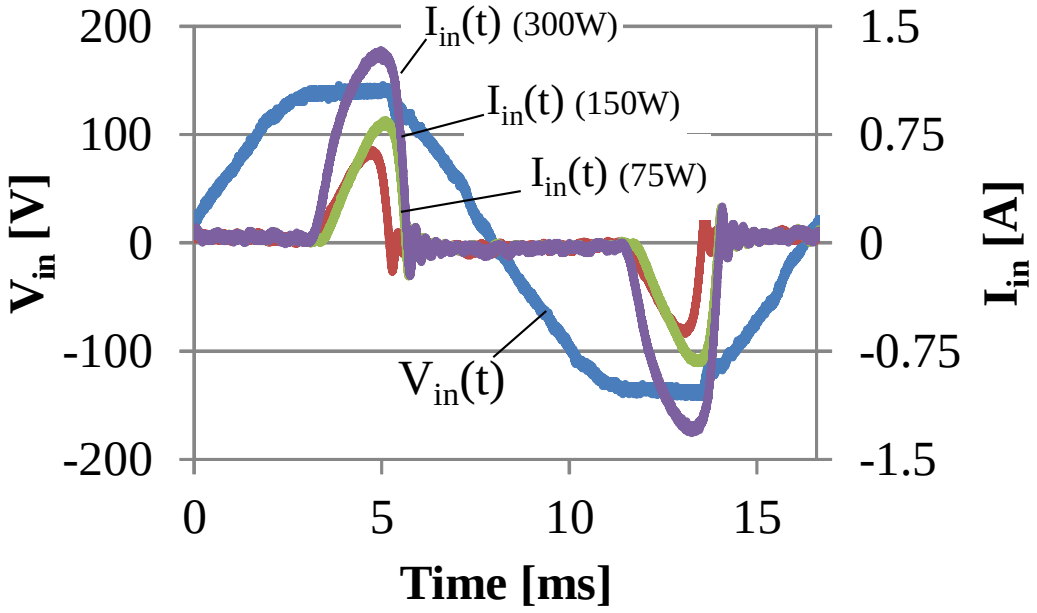

(a) Capacitor input operation

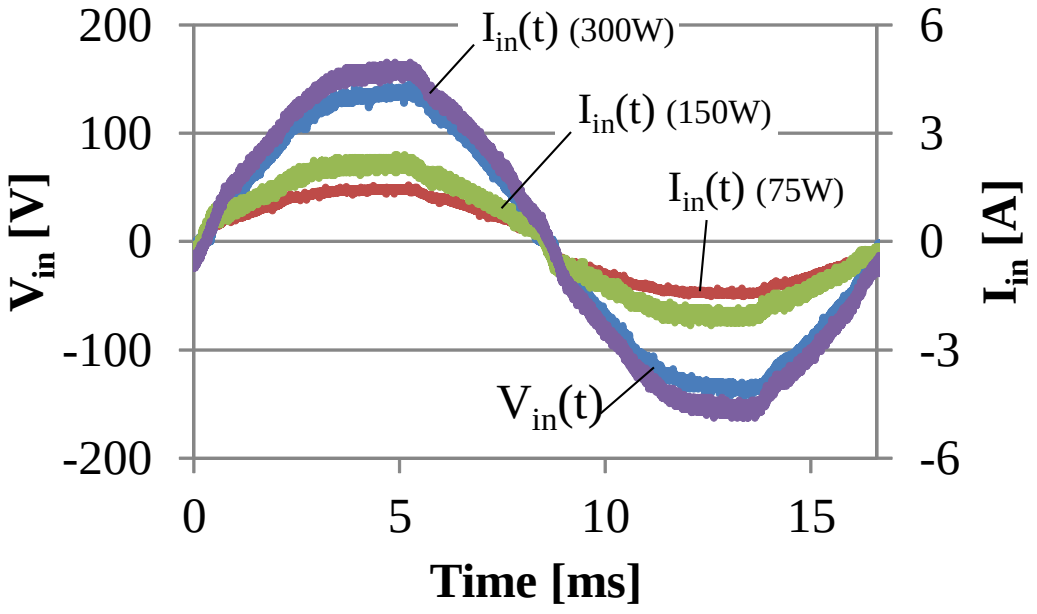

(b) PFC operation

Figure 4.4: Input voltage and current waveforms of PFC converter

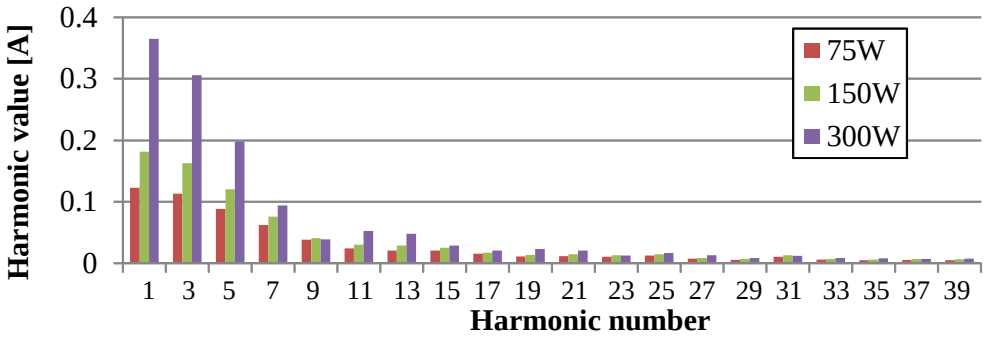

(a) Capacitor input operation

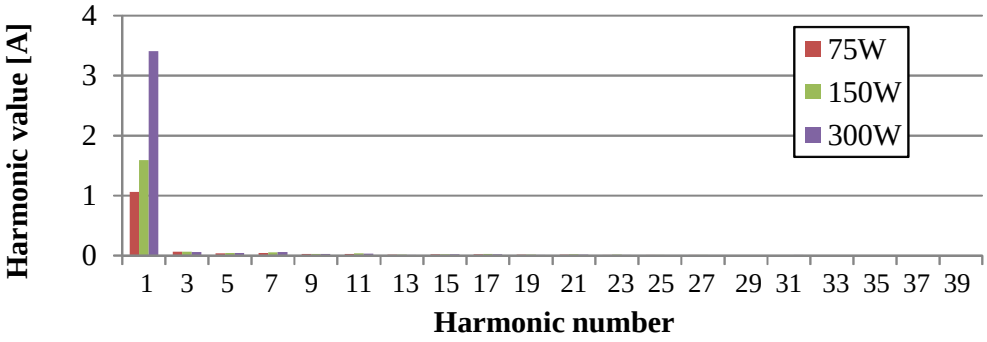

(b) PFC operation

Figure 4.5: Amplitude of input current harmonics

4.3 Loss evaluation of CCM PFC converter

4.3.1 Diode and MOSFET dynamic characteristics

This section shows the static characteristics of the studied Si-PiND (Fairchild Semiconductor, RHRP860, 600 V, 8 A), Si-SBD (Power Integrations, QH08TZ600, 600 V, 8 A), and SiC-SBD (Infineon IDH12SG60C, 600 V, 12 A). These devices were packaged in TO-220 and have almost the same current ratings. Figs.4.6(a) and (b) show the measured forward and reverse I–V characteristics of the diodes at room temperature obtained using a curve tracer (Tektronix, 371B). The DC forward voltage drop of the Si-SBD is the highest for same forward current, as shown in Fig.4.6(a). The high blocking voltage of the Si-SBD requires a thick drift layer and low-impurity concentration, which results in higher conduction resistance than other diode type. The reverse leakage currents at rated reverse voltage of the three diode type are comparable, and well below the rated values in the data sheets, which satisfy the rated blocking voltage (600 V), as shown in Fig.4.6(b). Fig.4.6(c) shows the C–V characteristics at room temperature, measured by a semiconductor characterization system (Keithley, 4200-SCS) with a 100-mV, 1-MHz AC measurement signal. The current ratings of the diodes are comparable, but the SiC-SBD yields the highest junction capacitance because of the high-impurity concentration in the drift region.

Fig.4.7 shows the configuration of the experimental PFC circuit and typical AC line current and voltage waveforms. The reverse recovery characteristics of the studied diodes in the circuit operation are discussed first in this section. Then, the total losses and conducted noise frequency spectrum of the PFC circuit are evaluated.

Fig.4.8 and Fig.4.9 show the measured reverse recovery behavior of three diodes in a CCM PFC circuit under two load conditions (75 and 300 W) at room temperature. The diode current is measured by a Rogowski coil current probe (IWATSU, SS-282) and recorded with a digital oscilloscope (Tektronix, DPO7354). The forward current of the diode in the CCM PFC circuit changes with the AC input

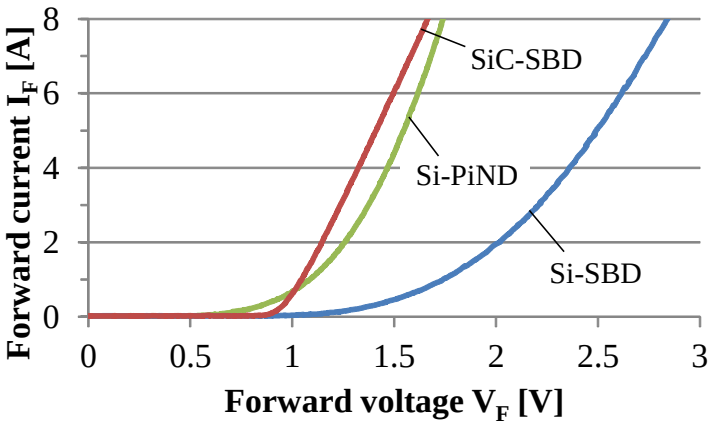

(a) Forward I–V characteristics

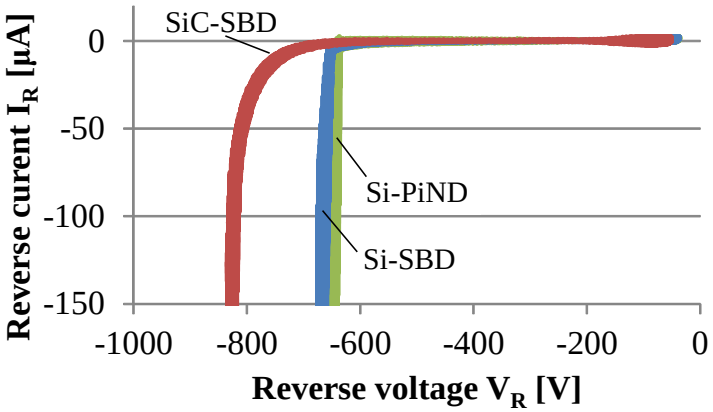

(b) Reverse I–V characteristics

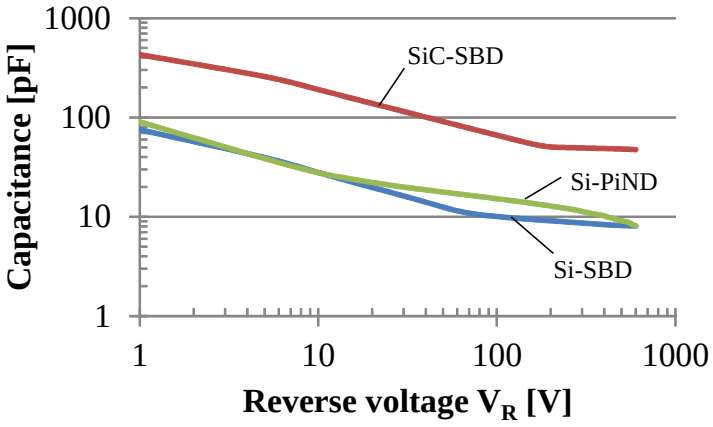

(c) C–V characteristics

Figure 4.6: Measured static characteristics of diodes

voltage and shapes the input AC current to a sinusoid in phase with the supply voltage. The symbols i), ii), and iii) correspond to the operating points shown

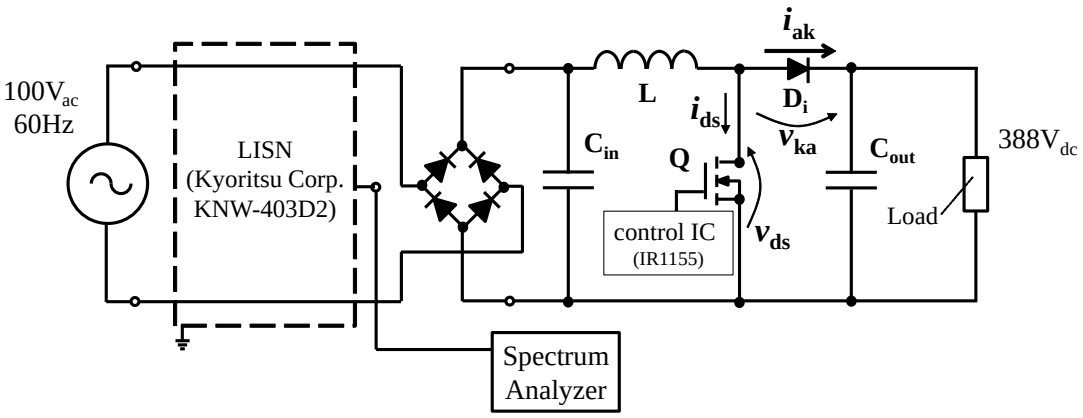

(a) Measurement circuit

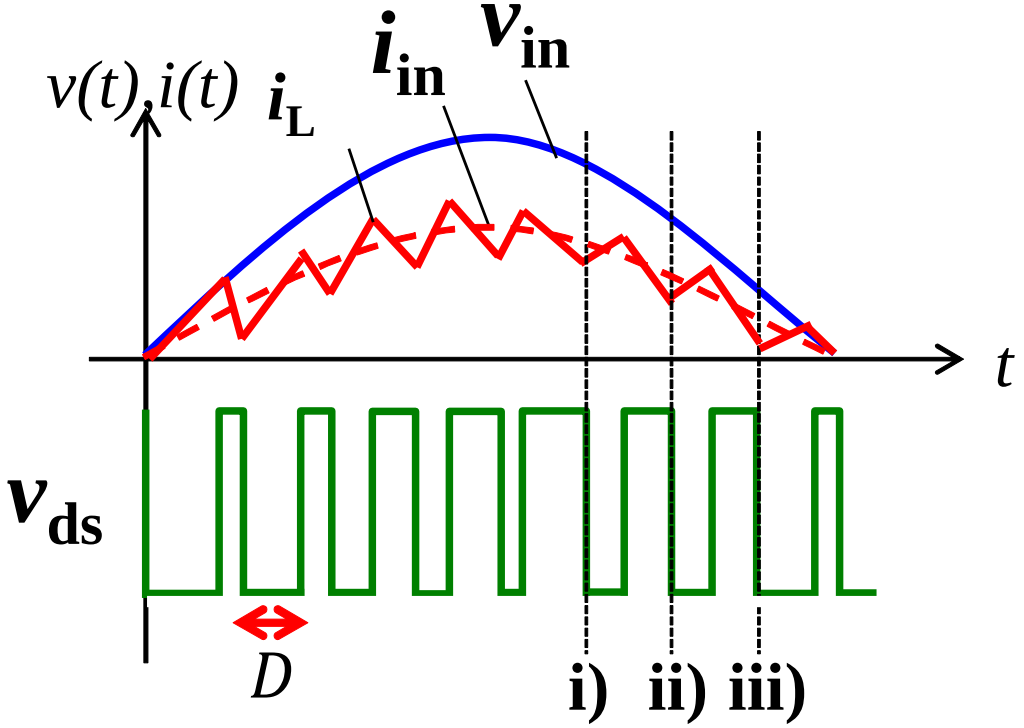

(b) AC line current and drain–source voltage of MOSFET

Figure 4.7: Measurement of the CCM PFC circuit configuration and typical waveforms of the circuit

in Fig.4.7(b). The forward conduction current of the diode is small for the 75-W load, and the reverse recovery phenomenon of the Si-PiND is not significant. The results are comparable to the operating points and type of diodes, as shown in Fig.4.8. The reverse recovery phenomenon of the diode due to large forward

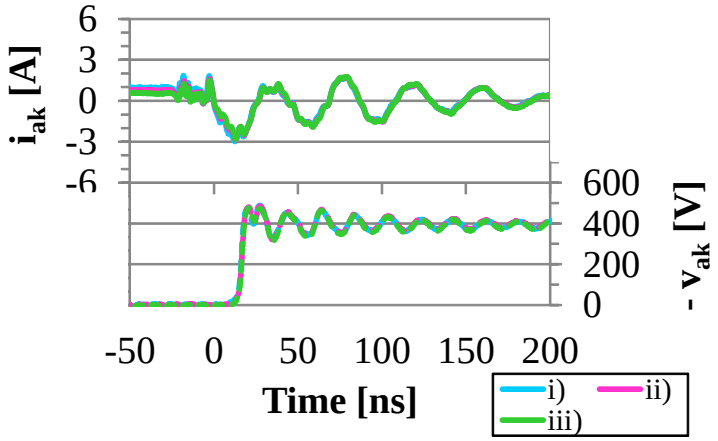

(a) Si-PiND

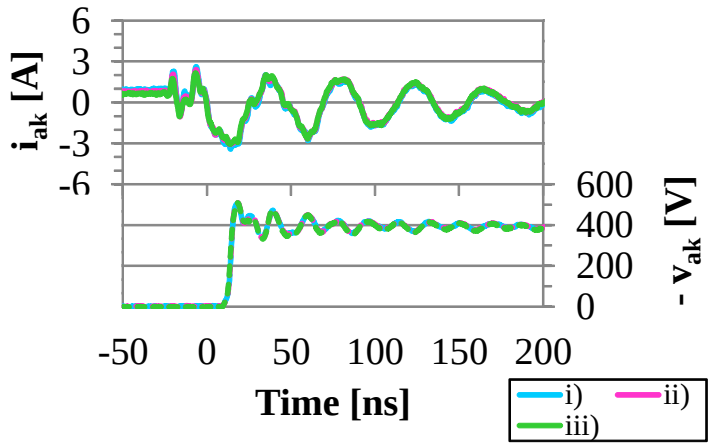

(b) Si-SBD

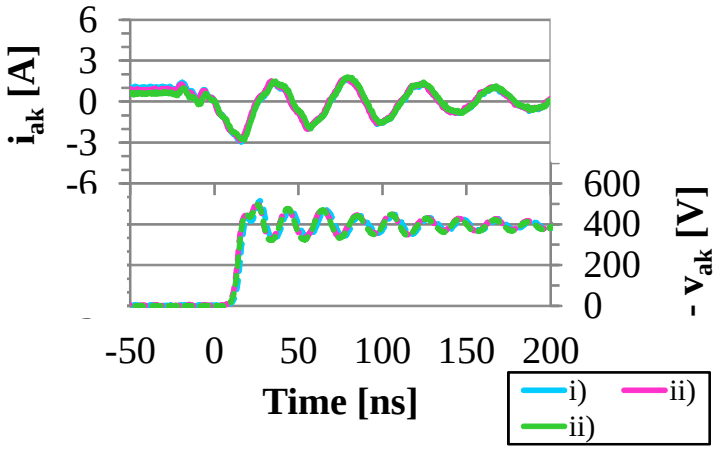

(c) SiC-SBD

Figure 4.8: Measured reverse recovery characteristics of diodes (Load: 75 W)

current is evident for 300-W load. The reverse current peak $I_{\mathrm{R_p}}$ and recovery time t_{rr} for respective diode in operating state i) are also shown in Figs.4.9. The

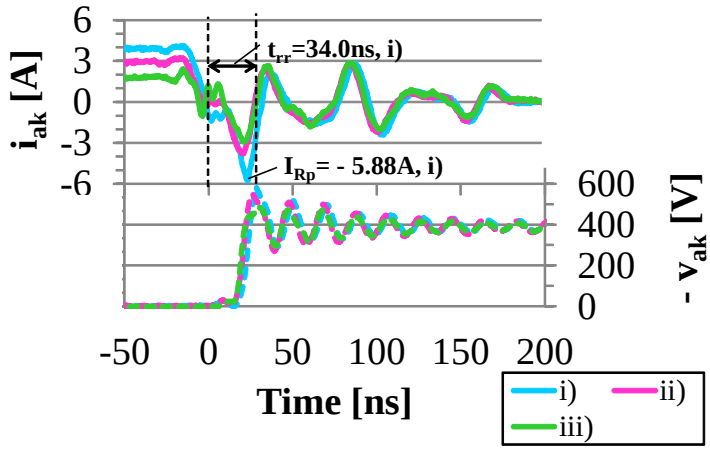

(a) Si-PiND

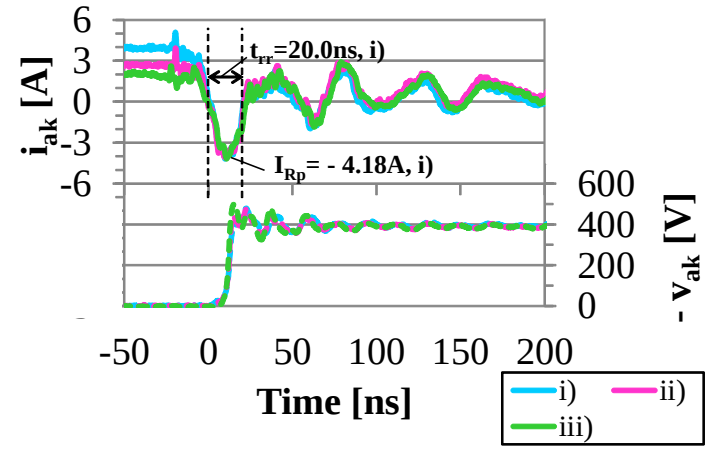

(b) Si-SBD

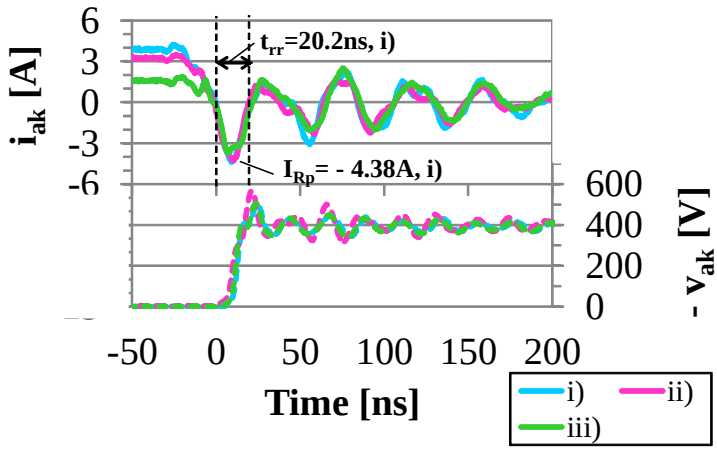

(c) SiC-SBD

Figure 4.9: Measured reverse recovery characteristics of diodes (Load: 300 W)

measured turn-off behavior of the Si-PiND in Fig.4.9(a) shows the character of bipolar devices in which a larger forward current leads to a larger peak reverse

current. The forward currents of the Si-SBD and SiC-SBD are also large under a large AC input voltage in i); however, the forward current level hardly affects the peak reverse current, as shown in Figs.4.9(b) and (c).

Fig.4.10 shows the measured turn-off characteristics of MOSFET for 300W-load. The type of diode hardly affects the turn-off behavior of MOSFET. The rate-of-rise of voltage ($\frac{dv_{ds}}{dt}$) for turn-off changes in proportion to the amplitude of i_{ds}. The ringing oscillation of v_{ds} is not observed with the low input AC voltage as in state iii).

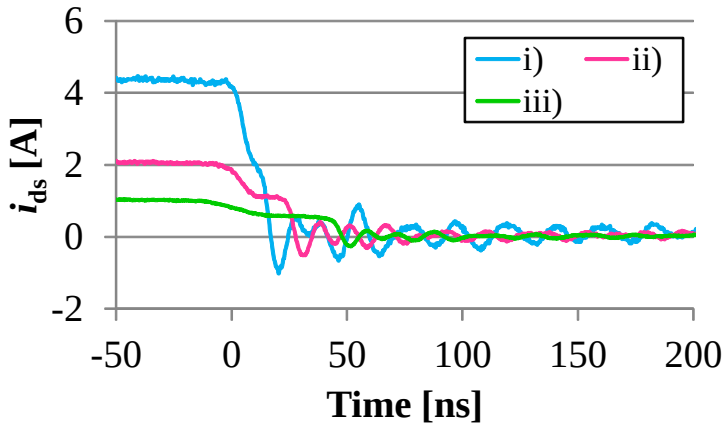

(a) Drain current

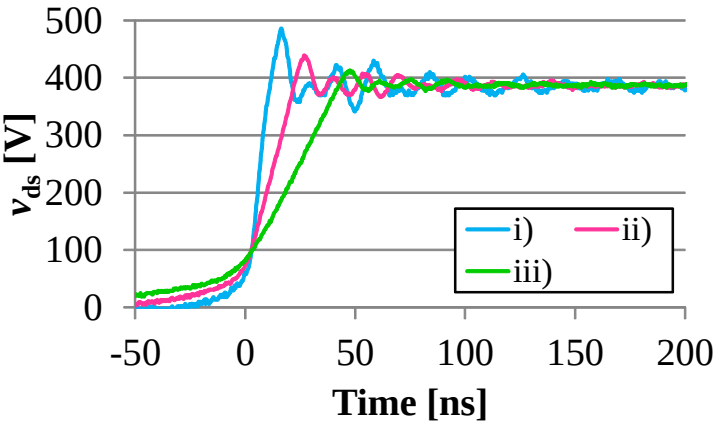

(b) Drain-Source voltage

Figure 4.10: Measured turn-off characteristics of MOSFET for 300-W load (SiC-SBD)

4.3.2 Measured total losses

Figs.4.11(a) and (b) show the calculated diode recovery losses at different operating points for the 75- and 300-W loads, respectively. The recovery losses are evaluated as the time integral of the instantaneous power from the time where the zero-crossing point of the current to the time, which gives 10 % of the peak reverse recovery current. The recovery losses of Si-PiND are higher than the other diodes for the load condition, and the losses increase with the forward current level at the operating point. On the other hand, the SBD shows a short recovery time, and the recovery loss is hardly affected by the forward current level. The Si-SBD shows the lowest recovery loss, which results from the lowest terminal capacitance, as shown in Fig.4.6(c).

The total losses of the tested CCM PFC circuit is experimentally evaluated. The experimental condition is the same except for the type of diode. The input power P_{in} and output power P_{out} of the PFC circuit are measured using a power analyzer (Tektronix PA4000). The total losses of the converter ($P_{in} - P_{out}$) under the 300-W load is 19.0, 23.7, and 21.1 W for the SiC-SBD, Si-PiND, and Si-SBD, respectively. The conduction losses of the SiC-SBD and Si-PiND are almost same, as shown in Fig.4.6(a); the difference results from the recovery losses. The recovery losses of the Si-SBD ares smaller than that of the SiC-SBD, but the total losses are larger. The difference comes from the conduction losses [Fig.4.6(a)]. These results suggest that the recovery losses and conduction losses of the diode account for a significant part of the total losses in the PFC circuit. Therefore, the SiC-SBD is more attractive than the Si diodes to reduce the switching losses in the CCM PFC circuit.

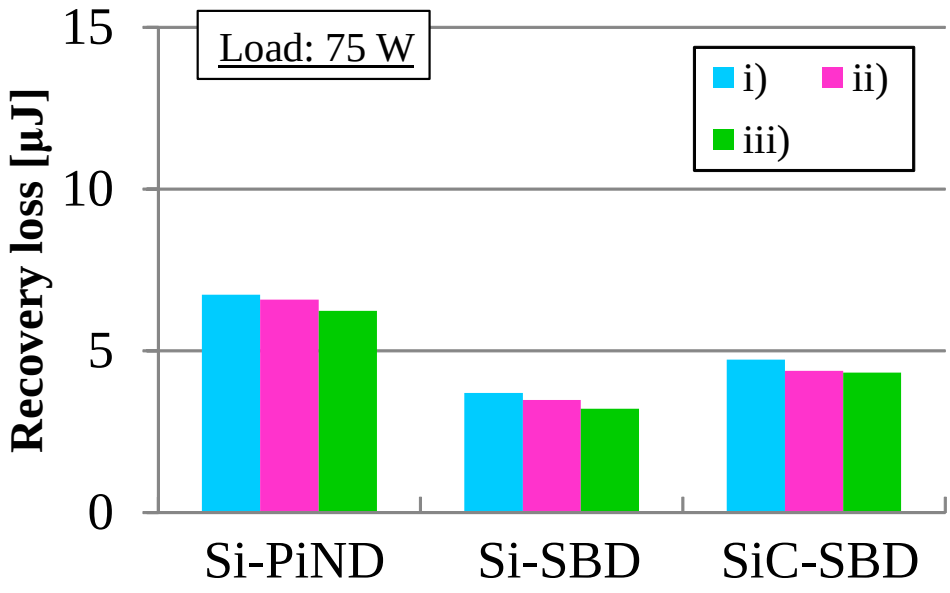

(a) Diode recovery losses (Load: 75 W)

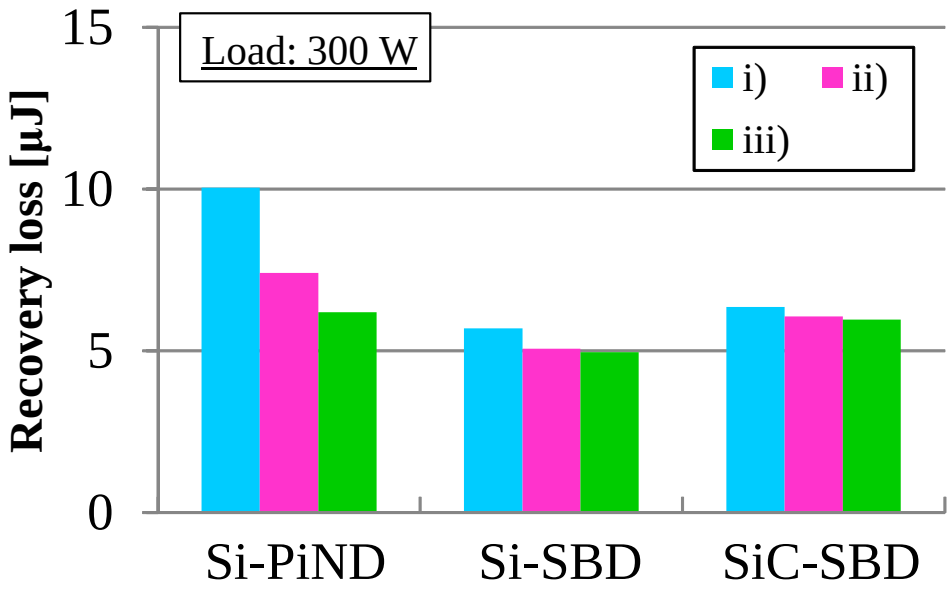

(b) Diode recovery losses (Load: 300 W)

Figure 4.11: Calculated reverse recovery losses of diodes

4.4 Conducted emission evaluation for CCM PFC converter based on time and frequency mixed domain

4.4.1 Conducted emission measurement in frequency domain

Fig.4.12 and Fig.4.13 show the measured frequency spectrum of the conducted noise in power line voltage of the PFC circuit for two load conditions (75 and 300 W). The noise terminal voltage of active power line to the ground is measured with a line impedance stabilization network (Kyoritsu Corp., KNW-403D2) and a spectrum analyzer (Agilent, E4402B) with a peak-detection mode. The type of diode is given as a parameter.

Figs.4.12(a) and (b) show the conducted noise spectrum in the lower frequency (100 kHz – 30 MHz) with a 9-kHz resolution bandwidth (RBW). The spectrum peaks correspond to the theoretical harmonic components of the integer multiple of the switching frequency up to several megahertz. The level of harmonic components is almost unaffected by the type of diode. The level of switching frequency and second-order harmonic component for the 300-W load are almost 10 dB higher than those for the 75-W load. The spectra in the 5–10 MHz frequency range for the 300-W load are also higher than those for the 75-W load. These spectra do not necessarily correspond to the integral multiple of the switching harmonics. They are estimated as noise components. The spectrum level above 10 MHz differ with the type of diode, especially for the 300-W load. The Si-PiND exhibits the highest noise levels in this frequency range. The Si-SBD and SiC-SBD exhibit a noise level approximately 5 dB lower than the Si-PiND, but the noise level becomes comparable around 30 MHz.

Figs.4.13(a) and (b) show the spectrum of the conducted noise terminal voltage at higher frequencies (10 – 200 MHz) than current EMI regulation. The RBW is 120 kHz, which is used for the radiated noise measurement. The RBW affects

the noise floor level, and therefore the noise floor shown in Figs.4.13(a) and (b) is 15 dB higher than those shown in Figs.4.12(a) and (b). The frequencies of the peak spectrum do not change with load. The spectrum peak levels from 30 to 50 MHz for the 300-W load are 10 dB higher than those for the 75-W load. There is not much difference in the spectrum peak level to the type of diodes above 30 MHz. However, the differences in noise spectrum distribution are observed for this frequency range. These differences are resulting from the difference in the terminal capacitance and recovery characteristics of the diodes.

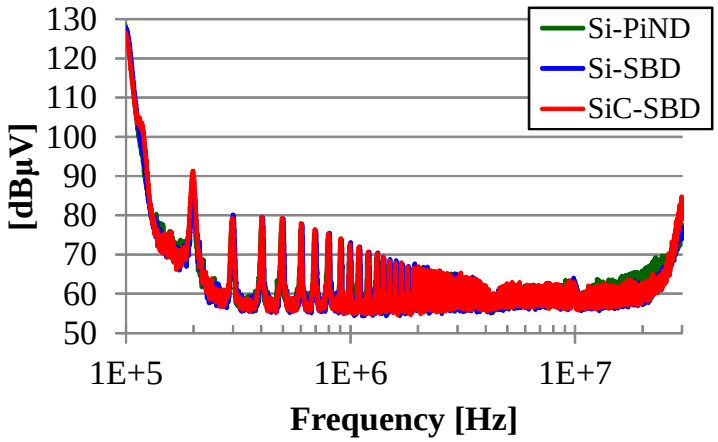

(a) Load: 75 W

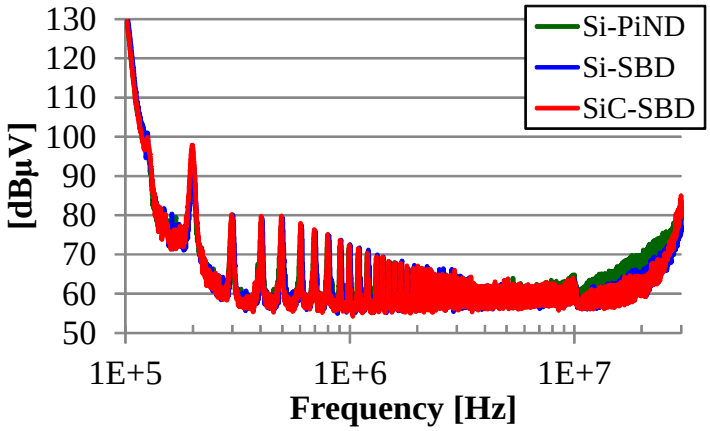

(b) Load: 300 W

Figure 4.12: Spectra of the terminal disturbance voltage for the tested CCM PFC circuit (100 kHz – 30MHz)

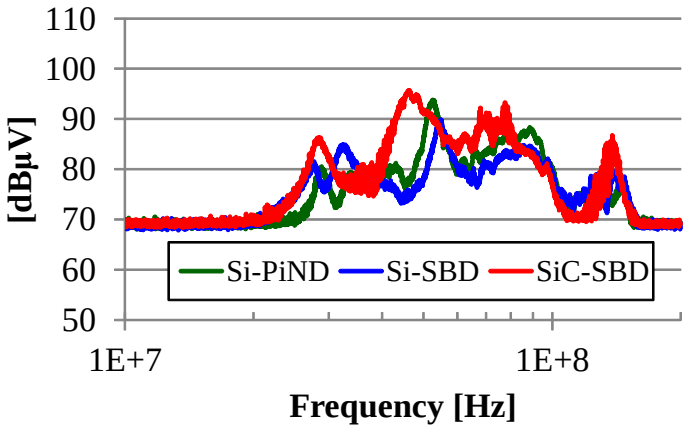

(a) Load: 75 W

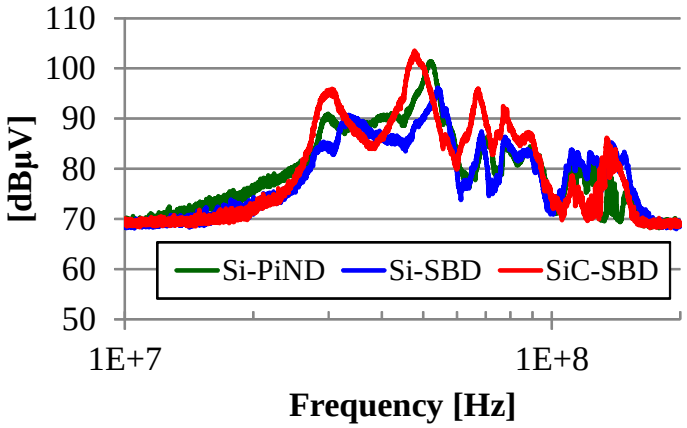

(b) Load: 300 W

Figure 4.13: Spectra of the terminal disturbance voltage for the tested CCM PFC circuit (10 MHz – 200MHz)

4.4.2 Conducted emission evaluation based on time and frequency mixed domain

The noise spectrum distribution shown in Fig.4.12 and Fig.4.13 may vary periodically stemming from periodical variation of input-voltage of PFC circuit, which changes the operating conditions of diode and MOSFET. Further study is required to clarify the relation between the noise spectrum and the device characteristics using the time domain analysis of noise spectrum.

Figs.4.14 and 4.15 are the spectrogram of the terminal disturbance voltage in one switching period at each operating point shown in Fig.4.7(b). The horizontal

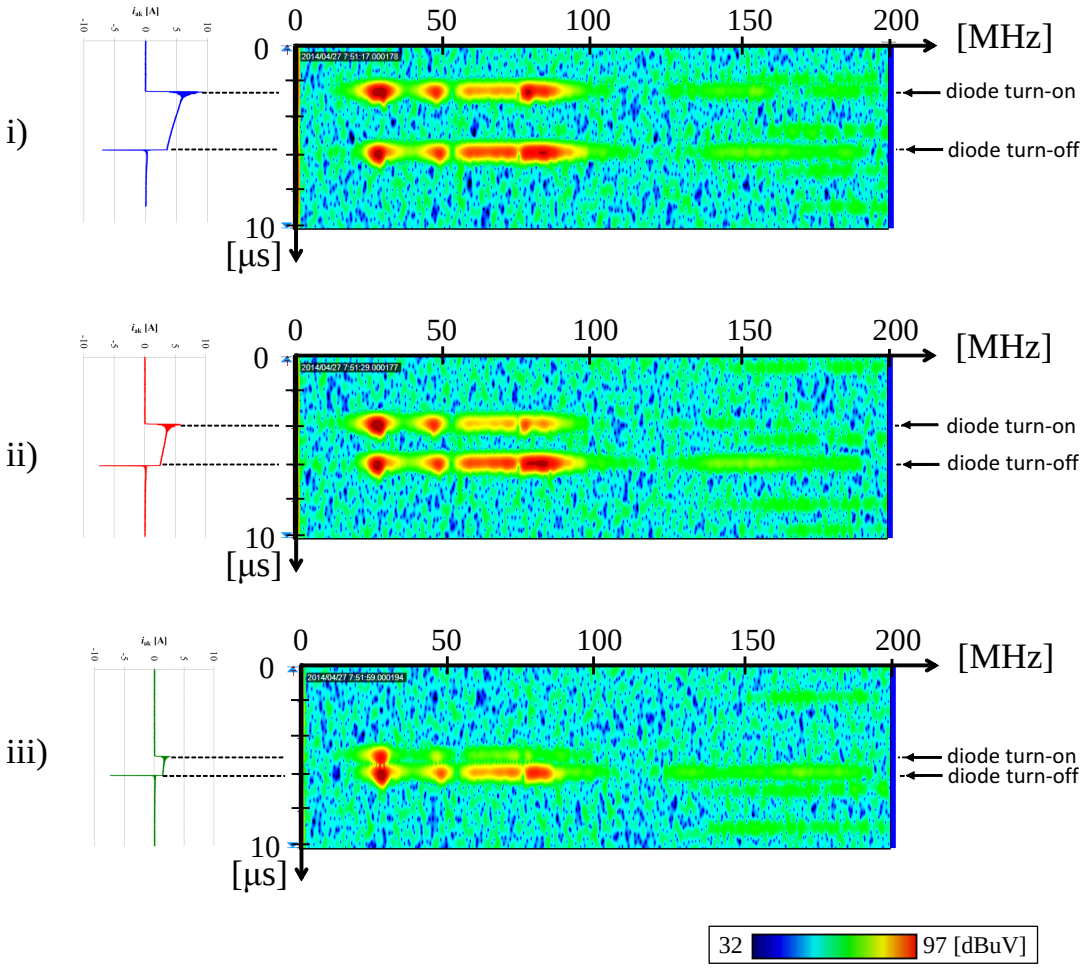

Figure 4.14: Spectrogram of the terminal disturbance voltage for the tested 300-W CCM PFC circuit (Si-PiND)

axis is frequency and the vertical axis is time, and the noise spectrum levels are color-corded. The noise spectrum level by the diode turn-on operation differs with operating states, which stems from the turn-off behavior of MOSFET shown in Fig.4.10. There is not much difference in the spectrum level and distribution for the diode turn-on operation among the different type of diodes.

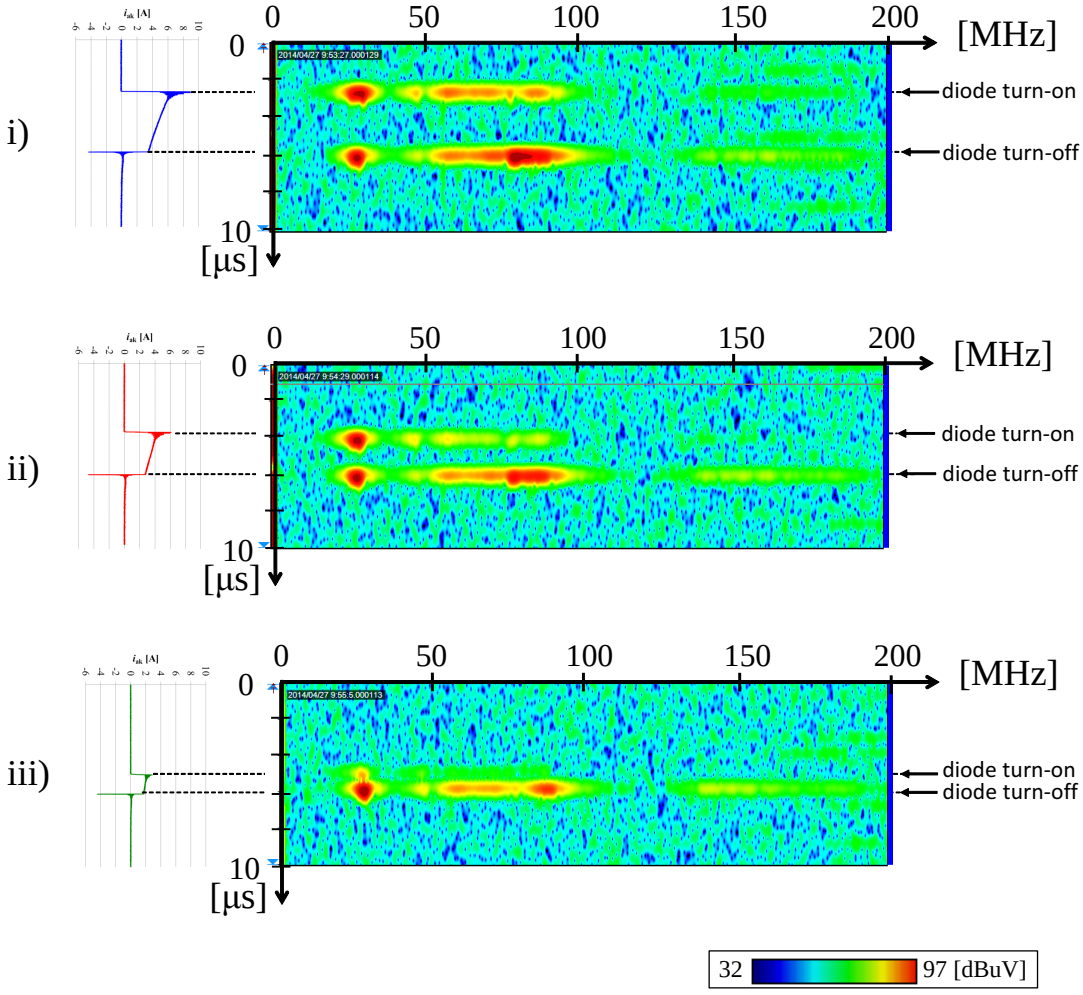

Figure 4.15: Spectrogram of the terminal disturbance voltage for the tested 300-W CCM PFC circuit (SiC-SBD)

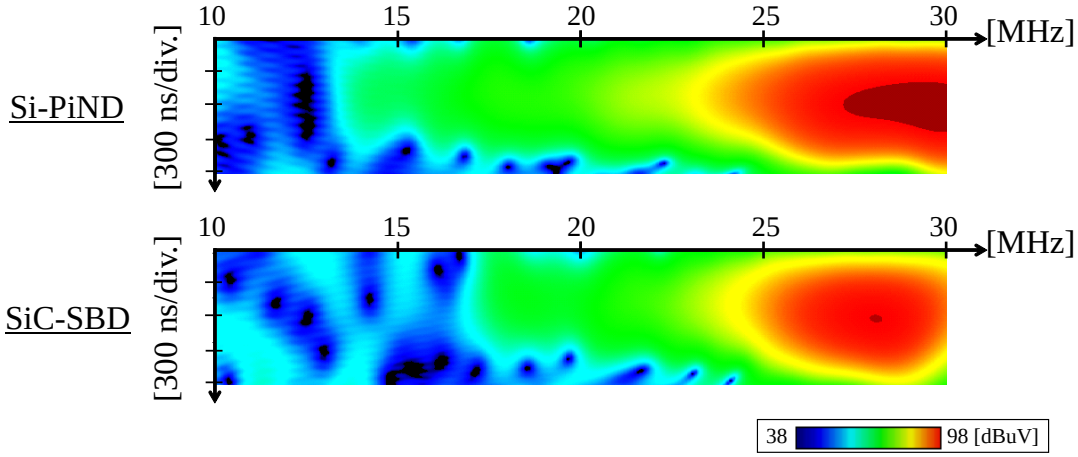

Figure 4.16: Spectrogram of the terminal disturbance voltage for the tested 300-W CCM PFC circuit in diode turn-off operation (10 – 30 MHz)

Fig.4.16 is the spectrogram of the terminal disturbance voltage from 10 MHz to 30 MHz in turn-off operation of diode at operating state i) shown in Fig.4.7(b). The noise emission level around 30 MHz for Si-PiND is higher than for SiC-SBD stemming from larger reverse current peak $I_{\mathrm{R_p}}$ and longer recovery time t_{rr} as shown in Fig.4.9.

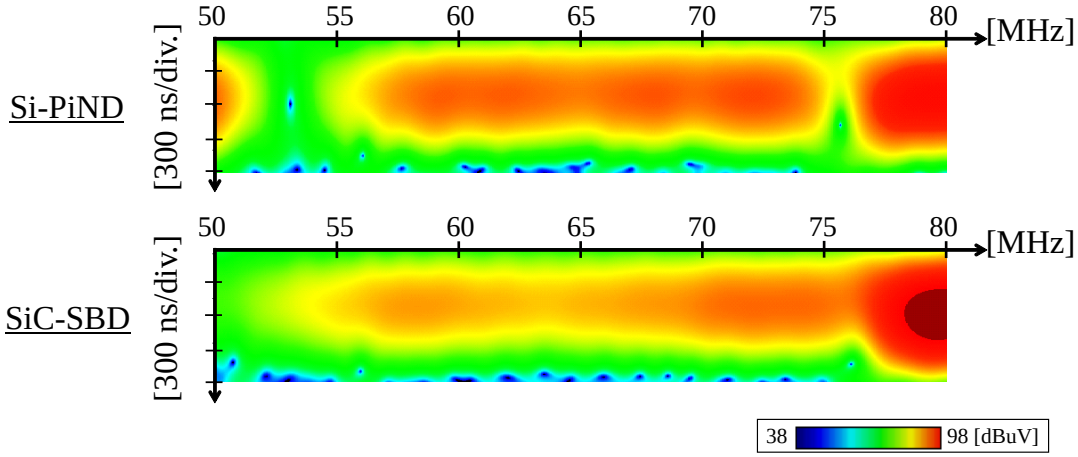

Figure 4.17: Spectrogram of the terminal disturbance voltage for the tested 300-W CCM PFC circuit in diode turn-off operation (50 – 80 MHz)

Fig.4.17 is the spectrogram of the terminal disturbance voltage from 50 MHz to 80 MHz in turn-off operation of diode at operating state i). High di/dt of recovery current for SiC-SBD generates higher level of noise emission around 80

MHz than for Si-PiND. Thus, the diode turn-off character has influence on the frequency distribution and dynamic character of conducted emission. The time and frequency mixed domain analysis for EMI noise emission gave valuable information on clarifying the EMI noise generation mechanisms.

4.5 Summary

This chapter investigated the conducted noise of the CCM PFC circuit and evaluated the difference among different type of diodes. The SiC-SBD gives less line-conducted noise levels around 20 MHz under heavy load conditions. The differences in noise spectrum distribution for higher frequency than 30 MHz are resulting from the difference in terminal capacitance and recovery characteristics of the diodes. The peak spectrum level does not differ much with the type of diodes. However, the spectrogram enables the the detection of transient events. The time and frequency mixed domain analysis for EMI noise emission gave valuable information on characterizing the noise source and EMI noise emission.

This chapter also investigated the difference in the losses. The difference in the total losses between the SiC-SBD and Si-PiND results from the difference in the reverse recovery phenomenon. SBDs do not exhibit noticeable difference in the recovery losses between the SiC-SBD and Si-SBD, but their conduction losses give a difference in the total losses. As a result, the SiC-SBD yields the lowest total losses in the PFC circuit. The measurement results presented in this chapter suggest that the SiC-SBD is more attractive than the Si diodes to reduce the losses in the CCM PFC circuit.

Chapter 5

Conclusions

5.1 Conclusions

This thesis was devoted to studies on EMI noise generation mechanism for switching converter based on time and frequency mixed domain analysis. This section summarizes each chapter and generalize the obtained results.

Chapter 2 treated EMI noise source analysis and evaluation methodology based on time and frequency mixed domain analysis. EMI noise standards and conventional EMI noise measurement methods were described earlier in this chapter as the basis for considering time and frequency mixed domain analysis. The basics of Prony's method to model dynamic characteristics and real-time spectrum analysis were addressed in this chapter.

Chapter 3 studied the diode type and its operating temperature dependency on the reverse recovery behavior and assessed the conducted emission in the CCM DC−DC boost converter. This chapter showed the conducted noise evaluation based on time and frequency mixed domain. The dynamic characteristics of diode turn-off current were evaluated by Prony's method, and extracted damping factor and ringing oscillation frequency were in good agreement with the conducted noise spectrum level and distributions. Si-PiND exhibited large peak reverse current and long recovery time, leading to an increased emission level in the conducted noise frequency range. However, the damping of the ringing oscillation current in

switching of Si-PiND increased at a high temperature, resulting in the suppressed noise level. In contrast, the SiC-SBD showed invariant switching behavior and conducted emission level to the operating temperature. The measurement of the spectrogram by using real-time spectrum analyzer enabled the detection of transient events. The spectrogram gave valuable information of the noise source and the conducted noise emission.

Chapter 4 focused on the noise in active power-factor correction (PFC) converters. It is difficult to evaluate the noise source in PFC converter over time in conventional frequency-domain analysis, whose noise spectrum depends on the operating point. This chapter assessed the influence of MOSFET's operating condition dependency on the conducted emission using real-time spectrum analyzer. The peak spectrum level does not differ much with the type of diode. However, the spectrogram revealed the relationship between the periodically changed AC input-voltage or diode dynamic characteristics and conducted emission from a PFC converter. These results showed that the time and frequency mixed domain analysis for EMI noise emission is effective to clarify the EMI noise generation mechanisms.

This research focused on the switching characteristics of power semiconductor devices, and its dynamic characteristics were evaluated for EMI noise source by the Prony's method. This research also examined the time variation of EMI noise emission based on real-time spectrum analysis. These studied methodologies could identify and characterize the EMI noise source in a switching converter, and it will lead to proper design of circuit layout that uses next-generation wide-bandgap power semiconductor devices for EMI noise mitigation.

5.2 Future works

It is important to clarify the EMI noise propagation mechanism as well as its generation mechanism for EMC design of a switching converter. The key to solve EMI noise issues is to understand how the return current get back to their source. The results of EMC compliance test depend not only on the switching behavior of the power device, but also on the characteristics of the parasitic coupling paths in the converter. EMI noise is classified in common and differential mode components according to their path. This separation is very important to conducted EMI noise modeling and appropriate EMC design. Estimating the parasitic components of the wiring, passive components, and power devices, and their influence on circuit behavior must be assessed. These studies can be combined with the work in this thesis to develop a general theory of electromagnetic compatible switching converter design in the future.

References

[1] N. Mohan, T. M. Undeland, and W. P. Robbins: *Power Electronics – Converters, Applications, and Design*, John & Wiley Sons, Inc., 2003.

[2] R. W. Erickson, D. Maksimovic: *Fundamentals of Power Electronics*, Kluwer Academic Publishers, 2004.

[3] M. Rashid: *Power Electronics Handbook*, Butterworth-Heinemann, 2010.

[4] A. Ioinovici: *Power Electronics and Energy Conversion Systems – Fundamentals and Hard-switching Converters*, John & Wiley Sons, Ltd., 2013.

[5] B. K. Bose: "Global Energy Scenario and Impact of Power Electronics in 21st Century," *IEEE Trans. Ind. Electron.*, vol. 60, no. 7, pp. 2638–2651, July 2013.

[6] B. K. Bose: "Power Electronics and Motor Drives Recent Progress and Perspective," *IEEE Trans. Ind. Electron.*, vol. 56, no. 2, pp. 581–588, Feb. 2009.

[7] B. K. Bose: "Energy, Environment, and Advances in Power Electronics," *IEEE Trans. Power Electron.*, vol. 15, no. 4, pp. 688–701, July 2000.

[8] M. Liserre, T. Sauter, J.Y. Hung: "Future Energy Systems: Integrating Renewable Energy Sources into the Smart Power Grid Through Industrial Electronics," *IEEE Ind. Electron. Mag.*, vol. 4, no. 1, pp. 18–37, Mar. 2010.

[9] J.M. Carrasco, L.G. Franquelo, J.T. Bialasiewicz, E. Galvan, R.C.P. Guisado, Ma.A.M. Prats, J.I. Leon, N. Moreno-Alfonso: "Power-Electronic Systems for

the Grid Integration of Renewable Energy Sources: A Survey," *IEEE Trans. Ind Electron.*, vol. 53, no. 4, pp. 1002–1016, June 2006.

[10] J. Lutz, A. Schlangenotto, U. Scheuermann and R. Doncker: *Semiconductor Power Devices – Physics, Characteristics, Reliability*, Springer, 2011.

[11] M. K. Kazimierczuk: *Pulse-width Modulated DC–DC Power Converters*, John & Wiley Sons, Ltd., 2008.

[12] J. Millan, P. Godignon, X. Perpina, A. Perez-Tomas, J. Rebollo: "A Survey of Wide Bandgap Power Semiconductor Devices," *IEEE Trans. Power Electron.*, vol. 29, no. 5, pp. 2155–2163, May 2014.

[13] J. Biela, M. Schweizer, S. Waffler, J.W. Kolar: "SiC versus Si – Evaluation of Potentials for Performance Improvement of Inverter and DC–DC Converter Systems by SiC Power Semiconductors," *IEEE Trans. Ind. Electron.*, vol. 58, no. 7, pp. 2872–2882, July 2011.

[14] A. R. Hefner, R. Singh, J. Lai, D. Berning, S. Bouche, C. Chapuy: "SiC Power Diodes Provide Breakthrough Performance for a Wide Range of Applications," *IEEE Trans. Power Electron.*, vol. 16, no. 2, pp. 273–280, Mar. 2001.

[15] N. Oswald, P. Anthony, N. McNeill, B.H. Stark: "An Experimental Investigation of the Tradeoff between Switching Losses and EMI Generation With Hard-Switched All-Si, Si-SiC, and All-SiC Device Combinations," *IEEE Trans. Power Electron.*, vol. 29, no. 5, pp. 2393–2407, May 2014.

[16] J.L. Hudgins, G. S. Simin, E. Santi, M. A. Khan: "An assessment of wide bandgap semiconductors for power devices," *IEEE Trans. Power Electron.*, vol. 18, no. 3, pp. 907–914, Mar. 2003.

[17] T. Funaki, J.C. Balda, J. Junghans, A.S. Kashyap, H.A. Mantooth, F. Barlow, T. Kimoto, T. Hikihara: "Power Conversion With SiC Devices at Extremely High Ambient Temperatures," *IEEE Trans. Power Electron.*, vol. 22, no. 4, pp. 1321–1329, July 2007.

[18] X. Zhong, X. Wu, W. Zhou, K. Sheng: "An All-SiC High-Frequency Boost DC–DC Converter Operating at 320°C Junction Temperature," *IEEE Trans. Power Electron.*, vol. 29, no. 10, pp. 5091–5096, Oct. 2014.

[19] R. Wang, D. Boroyevich, P. Ning, Z. Wang, F. Wang, P. Mattavelli, K.D.T. Ngo, K. Rajashekara: "A High-Temperature SiC Three-Phase AC–DC Converter Design for > 100°C Ambient Temperature," *IEEE Trans. Power Electron.*, vol. 28, no. 1, pp. 555–572, Jan. 2013.

[20] Y. Xiao, H. Shah, T.P. Chow, R.J. Gutmann: "Analytical Modeling and Experimental Evaluation of Interconnect Parasitic Inductance on MOSFET Switching Characteristics," *19th Annu. IEEE Applied Power Electronics Conference and Exposition (APEC '04)*, vol. 4, no. 1, pp. 516–521, 2004.

[21] O. Alatise, N.A. Parker-Allotey, D. Hamilton, P. Mawby: "The Impact of Parasitic Inductance on the Performance of Silicon-Carbide Schottky Barrier Diodes," *IEEE Trans. Power Electron.*, vol. 27, no. 8, pp. 3826–3833, Aug. 2012.

[22] M. I. Montrose, E. M. Nakauchi: *Testing for EMC compliance – Approaches and Techniques*, John & Wiley Sons, Inc., 2004.

[23] C. R. Paul: *Introduction to electromagnetic compatibility*, John Wiley & Sons, Inc., 2006.

[24] H. Ott: *Electromagnetic Compatibility Engineering*, John & Wiley Sons, Inc., 2009.

[25] P. Andre and K Wyatt: *EMI Troubleshooting Cookbook for Product Designers*, SciTech Publishing, 2014.

[26] K. Mainali, R. Oruganti: "Conducted EMI Mitigation Techniques for Switch-Mode Power Converters: A Survey," *IEEE Trans. Power Electron.*, vol. 25, no. 9, pp. 2344–2356, Sept. 2010.

[27] S. Maniktala: *Switching Power Supplies A to Z*, Elsevier/Newnes, 2006.

[28] F.Y. Shih, D.Y. Chen, Y.P. Wu, Y.T. Chen: "A procedure for designing EMI filters for AC line applications," *IEEE Trans. Power Electron.*, vol. 11, no. 1, pp. 170–181, Jan. 1996.

[29] V. Vlatkovic, D. Borojevic, F.C. Lee: "Input filter design for power factor correction circuits," *IEEE Trans. Power Electron.*, vol. 11, no. 1, pp. 199–205, Jan. 1996.

[30] L. Rossetto, S. Buso, G. Spiazzi: "Conducted EMI issues in a 600-W single-phase boost PFC design," *IEEE Trans. Ind. Appl.*, vol. 36, no. 2, pp. 578–585, Mar./Apr. 2000.

[31] M. Shoyama, G. Li, T. Ninomiya: "Balanced switching converter to reduce common-mode conducted noise," *IEEE Trans. Ind. Electron.*, vol. 50, no. 6, pp. 1095–1099, Dec. 2003.

[32] S. Wang, P. Kong, F.C. Lee: "Common Mode Noise Reduction for Boost Converters Using General Balance Technique," *IEEE Trans. Power Electron.*, vol. 22, no. 4, pp. 1410–1416, July 2007.

[33] M. Vilathgamuwa, J. Deng, K.J. Tseng: "EMI suppression with switching frequency modulated DC-DC converters," *IEEE Ind. Appl. Mag.*, vol. 5, no. 6, pp. 27–33, Nov./Dec. 1999.

[34] J. Balcells, A. Santolaria, A. Orlandi, D. Gonzalez, J. Gago: "EMI reduction in switched power converters using frequency modulation techniques," *IEEE Trans. Electromagn. Compat.*, vol. 47, no. 3, pp. 569–576, Aug. 2005.

[35] K.K. Tse, H.S. H Chung, S.Y. Huo, H.C. So: "Analysis and spectral characteristics of a spread-spectrum technique for conducted EMI suppression," *IEEE Trans. Power Electron.*, vol. 15, no. 2, pp. 399–410, Mar. 2000.

[36] H. Chung, S.Y.R. Hui, K.K. Tse: "Reduction of power converter EMI emission using soft-switching technique," *IEEE Trans. Electromagn. Compat*, vol. 40, no. 3, pp. 282–287, Aug. 1998.

[37] M. Joshi, V. Agarwal: "Design optimization of ZVS and ZCS quasi-resonant converters for EMI reduction," *Proc. Int. Conf. Electromagn. Interference Compat.*, pp. 407–413, 1997.

[38] T. Williams: *EMC for Product Designers*, Elsevier Ltd., 2007.

[39] J.-S. Lai, X. Huang, E. Pepa, S. Chen, T.W. Nehl: "Inverter EMI modeling and simulation methodologies," *IEEE Trans. Power Electron.*, vol. 15, no. 2, pp. 399–410, Mar. 2000.

[40] N. Oswald, B.H. Stark, D. Holliday, C. Hargis, B. Drury: "Analysis of Shaped Pulse Transitions in Power Electronic Switching Waveforms for Reduced EMI Generation," *IEEE Trans. Ind. Electron.*, vol. 53, no. 3, pp. 736–744, Jun. 2006

[41] J.F. Hauer, C.J. Demeure, L.L. Scharf: "Initial Results in Prony Analysis of Power System Response Signals," *IEEE Trans. Power Syst.*, Vol. 5, No. 1 pp.80–89, Feb. 1990.

[42] D.J. Trudnowaki, J.R. Smith, T.A. Short, D.A. Pierre:"An Application of Prony Methods in PSS Design for Multimachine Systems", *IEEE Trans. Power Syst.*, Vol. 6, No. 1 pp.118–126, Feb. 1991.

[43] D.J. Trudnowaki:"Order Reduction of Large-scale Linear oscillatory System Models," *IEEE Trans. Power Syst.*, vol. 9, no. 1 pp.451-458, Feb. 1994.

[44] R. Kumaresan, D.W. Tufts, L.L. Scharf:"A Prony Method for Noisy Data: Choosing the Signal Components and Selecting the Order in Exponential Signal Models," *IEEE Proceedings*, vol. 72, no. 2, pp. 230-233, Feb. 1984.

[45] T. Lobos, J. Rezmer, P. Schegner:"Parameter Estimation of Distorted Signals Using Prony Method," *2003 IEEE Power Tech Conference Proceedings*, vol. 4, pp.23-26, June 2003.

[46] A.A. Istratov, O.F. Vyvenko:"Exponential analysis in physical phenomena," *Review of Scientific Instruments*, vol. 70, no. 2, pp. 1233-1257, Feb. 1999.

[47] S. Braun, T. Donauer, P. Russer:"A Real-Time Time-Domain EMI Measurement System for Full-Compliance Measurements According to CISPR 16-1-1", *IEEE Trans. Electromagn. Compat.*, Vol. 50, No. 2 pp.259–267, May 2008.

[48] S. Braun:"An Overview of Emission Measurements in Time-domain," *IEEE Trans. Power Syst.*, vol. 9, no. 1 pp.451-458, Feb. 1994.

[49] Tektronix Primers: "Understanding FFT Overlap Processing Fundamentals," http://www.tektronix.com

[50] A.V. Oppenheim, R. W. Schafer: *Discrete-Time Signal Processing*, Prentice-Hall, 1999.

[51] P. Russer:"EMC measurements in the time-domain," *General Assembly and Scientific Symposium (URSI 2011)*, pp. 1-35, Aug. 2011.

[52] M. Kuisma, P. Silventoinen:"Using Spectrograms in EMI-analysis – An Overview," *20th Annual IEEE Applied Power Electronics Conference and Exposition (APEC '05)*, vol. 3, pp. 1953-1958, Mar. 2005.

[53] L. Coppola, Q. Liu, S. Buso, D. Boroyevich, A. Bell:"Wavelet Transform as an Alternative to the Short-Time Fourier Transform for the Study of Conducted Noise in Power Electronics," *IEEE Trans. Ind. Electron.*, vol. 55, no. 2, pp. 880–887, Feb. 2008.

[54] S. Qian, D. Chen:"Joint Time-Frequency Analysis," *IEEE Signal Processing Magazine*, vol. 16, Issue. 2 pp.31-33, Mar. 1999.

[55] D. Li, X. Ruan: "A High Efficient Boost Converter with Power Factor Correction," *35th Annu. IEEE Power Electronics Specialists Conference (PESC '04)*, vol. 2, pp. 1653–1657, June 2004.

[56] A. Guerra, F. Maddaleno, M. Soldano: "Effects of Diode Recovery Characteristics on Electromagnetic Noise in PFCs," *13th Annu. Applied Power Electronics Conference and Exposition (APEC '98)*, pp. 944–949, vol. 2, 1998.

[57] J. Jovalusky: "New Low Reverse Recovery Charge (Q_{RR}) High-Voltage Silicon Diodes Provide Higher Efficiency than Presently Available Ultrafast Rectifiers", *23rd Annu. IEEE Applied Power Electronics Conference (APEC '08)*, pp. 918-923, Feb. 2008.

[58] B. Ozpineci and L. M. Tolbert: "Characterization of SiC Schottky Diodes at Different Temperatures" *IEEE Power Electron. Lett.*, vol. 1, no. 2, pp.54-57, June 2003.

[59] G. Spiazzi, S. Buso, M. Citron, M. Corradin and R. Pierobon: "Performance Evaluation of a Schottky SiC Power Diode in a Boost PFC Application", *IEEE Trans. Power Electron.*, vol. 18, no. 6, pp. 1249-1253, Nov. 2003.

[60] O. Garcia, J. A. Cobos, R. Prieto, P. Alou, J. Uceda: "Single Phase Power Factor Correction: A Survey,"*IEEE Trans. Power Electron.*, vol. 18, no. 3, pp. 749–755, May 2003.

[61] ON Semiconductor reference manual: Power Factor Correction Handbook, HBD853/D (2011)
http://www.onsemi.com/pub_link/Collateral/HBD853-D.pdf

[62] M. M. Jovanovic and Y. Jang: "State-of-the-art, Single-Phase, Active Power-Factor-Correction Techniques for High-Power Applications – An Overview", *IEEE Trans. Ind. Electron.* vol. 52, no. 3, pp. 701-708, June 2005.

Publications

- Published papers

  1. Takaaki Ibuchi, Tsuyoshi Funaki: “ A study on modeling of dynamic characteristics of circuit component in TDR measurement based on Prony analysis, ”IEICE Electron. Express, Vol.8, No.18, pp.1534-1540 (2011)

  2. Takaaki Ibuchi, Tsuyoshi Funaki: “ Loss and conducted noise characteristics for CCM PFC circuit with SiC-Schottky barrier diode, ”IEICE Electron. Express, Vol.11, No.6, 20140142, pp.1-8 (2014)

  3. Takaaki Ibuchi, Tsuyoshi Funaki: “ Effect of diode operating temperature on conducted noise spectrum for CCM DC-DC boost converter, ” IEICE Communications Express, Vol.3, No.9, pp.269-274 (2014)

- International conference proceedings

  1. Takaaki Ibuchi, Tsuyoshi Funaki: “ A Study on EMI Noise Source Modeling with Current Source for Power Conversion Circuit, ”International Symposium on Electromagnetic Compatibility (EMC Europe 2012), Rome, Italy, Sep. 17-21, 2012

  2. Takaaki Ibuchi, Tsuyoshi Funaki: “ A study on copper loss minimization of air-core reactor for high frequency switching power converter, ” The 4th International Symposium on Power Electronics for Distributed Generation Systems (PEDG 2013), Rogers, Arkansas, U.S.A., July 8-11, 2013

3. Takaaki Ibuchi, Tsuyoshi Funaki: “ Validation of the air-core inductor copper loss model for high-frequency power conversion applications, ” International Symposium on Electromagnetic Compatibility (EMC Europe 2013), Brugge, Belgium, Sep. 2-6, 2013

4. Takaaki Ibuchi, Ryuma Kamikomaki, Tsuyoshi Funaki: “ Experimental evaluation on time variation of conducted noise spectrum for PFC circuit, ”EMC'14/Tokyo, Tokyo, Japan, May 13-16, 2014

5. Takaaki Ibuchi, Tsuyoshi Funaki:“ Effect of diode characteristics on conducted noise spectrum in CCM boost converter, ”International Symposium on Electromagnetic Compatibility (EMC Europe 2014), Gothenburg, Sweden, Sep. 1-4, 2014

- Domestic conference proceedings

1. Tsuyoshi Funaki, Takaaki Ibuchi: “ Measuring terminal capacitance of power devices using TDR method, ”The Papers of Technical Meeting on Electromagnetic Compatibility, IEE Japan, Suita, Osaka, EMC-10-001, pp.1-6 (2010)

2. Takaaki Ibuchi, Tsuyoshi Funaki: “ A study on circuit parameter identification based on Prony analysis in TDR measurement, ”The Papers of Technical Meeting on Electromagnetic Compatibility, IEE Japan, Hanamaki, Iwate, EMC-10-037, pp.43-48 (2010)

3. Takaaki Ibuchi, Tsuyoshi Funaki: “ A study on modeling of dynamic characteristics of DUT based on TDR measurement with Prony analysis, ”The Papers of Technical Meeting on Electromagnetic Compatibility, IEE Japan, Kaga, Ishikawa, EMC-11-004, pp.17-22 (2011)

4. Takaaki Ibuchi, Tsuyoshi Funaki: “ Experimental study on impedance characterization of half bridge circuit and circuit components, ”The Papers of Joint Technical Meeting on Electron Devices and Semiconductor Power Converter, IEE Japan, Matsue, Shimane, EDD-11-056, SPC-11-148, pp.35-40 (2011)

5. Takaaki Ibuchi, Tsuyoshi Funaki:“ An experimental study on impedance frequency characterization of power conversion circuit for EMI noise source modeling, ”The Papers of Technical Meeting on Electromagnetic Compatibility, IEE Japan, Nagoya, Aichi, EMC-11-033, pp.29-34 (2011)
6. Takaaki Ibuchi, Tsuyoshi Funaki: “ A study on EMI noise source modeling with current source of power conversion circuit, ” The Papers of Technical Meeting on Electromagnetic Compatibility, IEE Japan, Tottori, EMC-12-002, pp.7-12 (2012)
7. Takaaki Ibuchi, Tsuyoshi Funaki: “ A study on optimal copper loss and dimension design of air core reactor for power conversion circuit, ” IEICE Technical Report, Vol.112, No.372, Nagasaki, EMCJ2012-110, pp.47-52 (2013)
8. Takaaki Ibuchi, Tsuyoshi Funaki: “ The copper loss model validation for air-core inductor with proximity effect, ”The Papers of Technical Meeting on Electromagnetic Compatibility, IEE Japan, Awara, Fukui, EMC-13-016, pp.25-30 (2013)
9. Takaaki Ibuchi, Tsuyoshi Funaki: “ A study on large signal copper loss model of inductor for power converter, ”The Papers of Technical Meeting on Electromagnetic Compatibility, IEE Japan, Sakyo-Ku, Kyoto, EMC-13-023, pp.23-28 (2013)
10. Takaaki Ibuchi, Ryuma Kamikomaki, Tsuyoshi Funaki: “ An experimental study on time variation of noise spectrum for a PFC circuit, ” The Papers of Technical Meeting on Electromagnetic Compatibility, IEE Japan, Sendai, Miyagi, EMC-13-051, pp.93-98 (2013)
11. Takaaki Ibuchi, Tsuyoshi Funaki: “ A study on reverse recovery behavior of diode and time variation of noise spectrum for a PFC circuit, ” The Papers of Technical Meeting on Electromagnetic Compatibility, IEE Japan, Kariya, Aichi, EMC-13-078, pp.49-54 (2013)
12. Takaaki Ibuchi, Tsuyoshi Funaki: “ A study on diode characteristics and conducted noise spectrum for DC-DC converter, ”The Papers of

Technical Meeting on Electromagnetic Compatibility, IEE Japan, Yufu, Oita, EMC-14-003, pp.5-10 (2014)

13. Takaaki Ibuchi, Ryuma Kamikomaki, Tsuyoshi Funaki: “ A study on the effect of smoothing capacitors and wiring inductance on the output voltage distortion in a converter circuit, ”The Papers of Technical Meeting on Electromagnetic Compatibility, IEE Japan, Kobe, Hyogo, EMC-14-026, pp.49-54 (2014)
14. Takaaki Ibuchi, Tsuyoshi Funaki: “ An experimental study on the effect of diode characteristics for conducted noise emission in DC-DC converter, ”The Papers of Technical Meeting on Electromagnetic Compatibility, IEE Japan, Yuri-honjo, Akita, EMC-14-032, pp.23-28 (2014)
15. Takaaki Ibuchi, Tsuyoshi Funaki: “ An experimental study on the effect of diode temperature for conducted noise emission in boost converter, ” The Papers of Joint Technical Meeting on Electron Devices and Semiconductor Power Converter, IEE Japan, Tsukuba, Ibaraki, EDD-14-062, SPC-14-124, pp.65-70 (2014)

- Awards

1. IEE Japan Excellent Presentation Award From The Fundamentals and Materials Society (2011)
2. Osaka University Engineering Society Award (2012)
3. IEE Japan Excellent Presentation Award (2012)
4. EMC’14/Tokyo IEEE EMC Society Japan and Sendai Chapters Student Award (2014)
5. Rohde & Schwarz RTO1004 Oscilloscope Report Contest Best Award (2014)